Orientational ordering of charged colloids

Eelco Eggen

2010

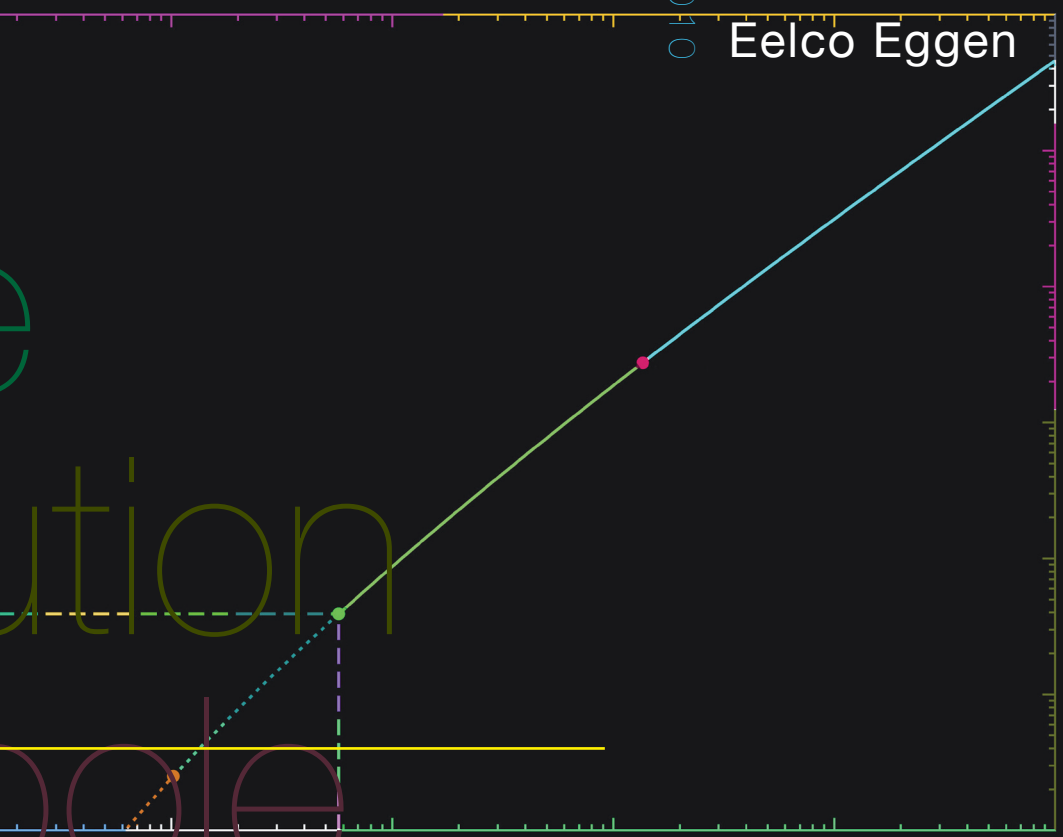

Ontwerp omslag: Otto te Wierik, idB[zsedM], Deventer
ISBN: 978-90-393-5301-1

Orientational ordering of charged colloids

Oriëntationele ordening van geladen colloïden
(met een samenvatting in het Nederlands)

Proefschrift

ter verkrijging van de graad van doctor aan de Universiteit Utrecht op gezag van de rector magnificus, prof.dr. J.C. Stoof, ingevolge het besluit van het college voor promoties in het openbaar te verdedigen op woensdag 24 februari 2010 des ochtends te 10.30 uur

door

Eelco Jurriaan Eggen

geboren op 26 april 1981 te Utrecht

Promotor: Prof.dr. H. van Beijeren
Co-promotor: Dr. R.H.H.G. van Roij

Contents

Chapter 1

Introduction

1.1 Charged colloidal suspensions

Colloidal suspensions consist of solid particles dispersed in a liquid medium. The size of these particles ranges from nanometers to micrometers. Therefore, they are large enough to be visible by means of microscopy, but they are small enough to experience Brownian motion. Suspended in a solvent of comparable density, they neither float on the surface, nor sink to the bottom. Brownian motion allows these systems to explore a large number of configurations, and it means that they are well described by statistical mechanics. It also means that colloidal suspensions can undergo phase transitions, such as gas–liquid or fluid–solid. Colloidal systems usually involve distributions of charge, because the solvent participates in a chemical reaction or adsorption—and subsequent equilibrium—with the surface of these colloidal particles. The charge present in the system is therefore distributed in a nontrivial way. Effects of these charge distributions have been thoroughly studied in the case that the particle shape is spherical and its chemical surface properties homogeneous, and to a lesser extent for nonspherical particles or heterogeneous chemical surface properties, where the charge distribution is more intricate. This thesis investigates such effects theoretically.

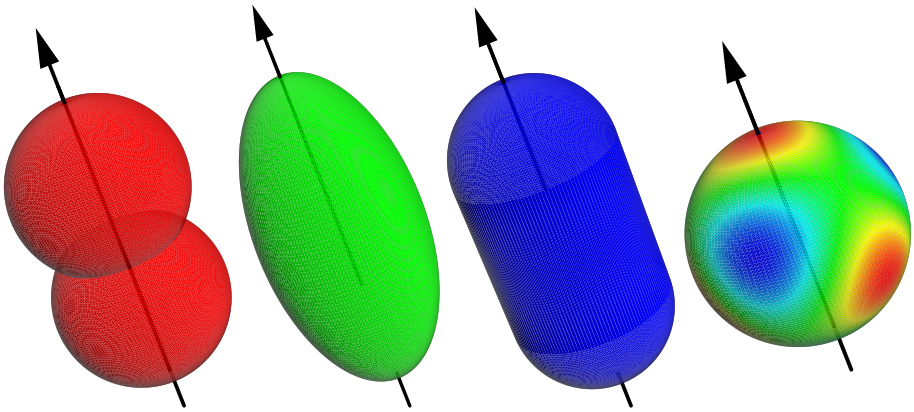

Figure 1.1: Illustration of particles of interest in this thesis—from left to right: dumbbells, ellipsoids of revolution (also known as spheroids), spherocylinders, and colloidal spheres with heterogeneous surface properties.

1.2 Self organization in soft matter

Colloidal suspensions belong to the larger class of matter, referred to as complex fluids, soft condensed matter, or simply *soft matter*. Soft matter is considered important in the fabrication of new materials. It has a time and length scale that is very convenient for observation, manipulation, and self organization on a microscopic level. Colloidal suspensions also play an important role as model systems for atomic and molecular fluids. In the research area of colloids and nanoparticles, chemists have been developing ways of synthesizing nonspherically-symmetric particles for application as building blocks for new materials. These have special properties, concerning shape, surface chemistry, or electric and magnetic behavior [1]. Until a few decades ago, there was just the choice of a handful of natural (clay, viral capsids) and synthetic particles (haematite, boehmite, gibbsite, gold, and silver nanocrystals, polymer spheres and rods). Moreover, these particles appeared in a limited variety of shapes, ranging from disks to spheroids to rods, although some had more exotic shapes such as cubes or spindles. Also, the yield of synthesis of these particles usually was quite low, and therefore their application remained limited.

In the last decades, however, novel methods of synthesis have been devised allowing for a larger yield as well as a larger choice of shapes and surface properties. Examples of these shapes are colloidal dumbbells [2], ellipsoidal colloids with aspect ratio ~ 3 [3], and nanoparticles synthesized with the shape of a rod, disk, snowman, cube,

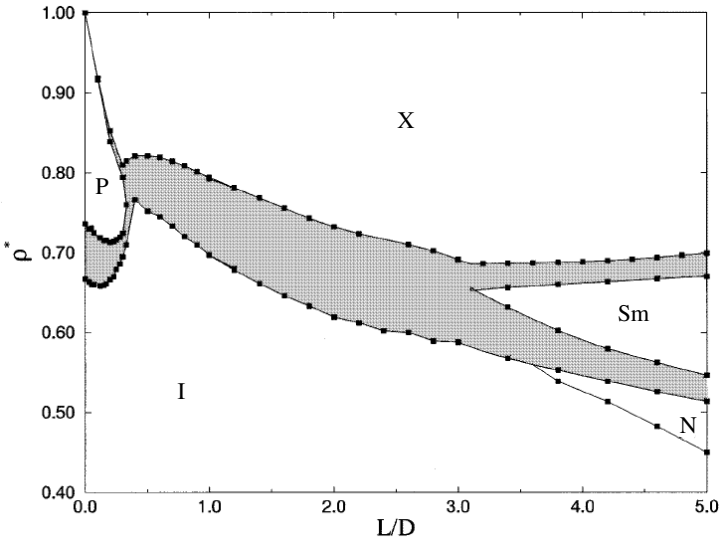

Figure 1.2: Phase diagram for hard spherocylinders as a function of aspect ratio L/D and density ρ^* (scaled with the close-packing density). The shaded regions denote phase coexistence. The following phases are depicted: isotropic fluid (*I*), orientationally ordered crystal (*X*), plastic crystal (*P*), nematic liquid crystal (*N*), and smectic-*A* liquid crystal (Sm). Taken from Bolhuis and Frenkel [19].

cap, or raspberry [4–10]. Examples of patterned surfaces are Janus colloids [11, 12], or striped particles [13]. A number of these particles are schematically illustrated in Fig. 1.1. It is clear that such a diversity of shapes and patterns need classification in the context of functional properties, since one of the goals is to create suitable particle properties for self assembly into new materials. This self assembly is driven by the Brownian motion that these particles experience in a liquid medium, and it is therefore governed by statistical mechanics. The resulting phase behavior depends on the particle interactions, which can be nonspherical by nature. These interactions can be tuned by means of tailoring Van der Waals forces, electrostatic or magnetic interaction, ligands [14, 15], linkers [16], or depletion interaction [17, 18].

A basic example of a colloidal system with nonspherical particle interactions is that of colloidal rods, which reveals a much richer phase behavior than systems of colloidal spheres. In addition to the completely isotropic fluid and completely aligned crystal phases, there can exist intermediate states [19–23]. A phase diagram for hard spherocylinders is shown in Fig. 1.2, where ρ^* denotes the rod density scaled with the

close packing density of spherocylinders. Rod shapes consist of a cylindrical segment of length L capped with two hemispheres of diameter D, and the rod aspect ratio is given by L/D. The phase diagram shows that for large elongations (i.e., $L/D \gtrsim 3.7$) the transition from the isotropic fluid phase (I) to the fully ordered crystal phase (X) is intermitted by two liquid-crystal phases (N and Sm), whereas for small elongations (i.e., nearly spherical particles; $L/D \lesssim 0.35$) a plastic crystal phase (P) is found. In a nematic phase (N), there is no positional ordering, but orientational symmetry is broken. In this simple case, the rod shapes are cylindrically symmetric, and the rods align in one direction. This direction is called the *director*, which acts as a symmetry axis about which all rods are orientationally distributed. In the smectic-A phase (Sm), the rods form stacks of liquid layers in which there is orientational alignment. The plastic-crystal (or rotator) phase (P) is characterized by an isotropic orientational distribution, but the positional ordering is crystal-like. In general, liquid crystals have a high degree of orientational ordering in contrast to a low degree of positional ordering, whereas the case is reversed in plastic crystals.

We propose that self assembly in soft matter should come about in the same way as in atomic and molecular systems: through bulk phase transitions from isotropic liquids to well-ordered solids. Also, we stress the importance of *intermediate* states between a low density isotropic fluid state and the high density ordered state. Although we do not address the kinetic properties of thermodynamic pathways along these lines, we will investigate the role of orientational ordering in intermediate states between fully isotropic and fully ordered. A large challenge that presently stands in the way of self assembly is to design and fabricate large quantities of particles that self organize into well-ordered structures with a large degree of control. Therefore, we need to make statements of the collective behavior of systems of nonspherically-symmetric charged colloidal particles, based on the single particle properties. However, we are limited in our approaches due to the immense complexity of these systems. Generally, the introduction of charge in the description of basic colloidal systems makes these rather difficult. This is evident from the fact that the study of the bulk phase behavior of homogeneously charged colloidal spheres still contains a number of open questions [24]. Moreover, the incorporation of orientational degrees of freedom and orientational dependence in the particle interactions further complicates the description. Even for hard rods and ellipsoids, the investigations are ongoing [25].

This thesis focusses on systems of charged colloidal particles that lack spherical symmetry, in contrast with the most basic treatment of colloids as homogeneously charged spherical particles. Experimental results reveal, for instance, that the chemical properties of the surfaces of some of these particles are *not* homogeneous [26, 27]. At a microscopic scale, these surface properties can display heterogeneities, resulting in heterogeneous charge distributions. Also, such heterogeneities can be purposely

devised to investigate their effect. One example is Janus colloids, where the two hemispheres of a spherical colloidal particle have a distinct surface composition [11, 12]. In certain cases, this will cause one hemisphere to be charged, but the other to be charge neutral, or even hydrophobic. The effect of the resulting particle interactions is observed to be cluster formation [28]. An illustration of charge heterogeneity is given schematically by the surface-color patterning of the sphere in Fig. 1.1. We wish to describe the self-organization of these particles in terms of bulk phase behavior due to particle interactions. The key features that we incorporate in this description are anisotropy of these interactions due to particle shape or surface charge distributions, and the orientational distributions of these particles due to their interactions.

1.3 Poisson-Boltzmann theory

The systems of interest in this thesis are suspensions of colloidal particles in an electrolytic solvent. We describe this electrolyte as a liquid medium (such as water or oil) containing positive and negative ions. The solvent is modelled as a dielectric medium, described by a (static) bulk dielectric constant. The common way to simplify the description of the electrolyte is a statistical-mechanical description referred to as Poisson-Boltzmann theory. It combines the Maxwell equation for static charge distributions known as Poisson's equation with an approximation for the ion-density distribution known as the Boltzmann distribution. The resulting model was introduced by Gouy [29] and Chapman [30], and it is thoroughly discussed in various textbooks [31, 32]. In this section, a short version of the derivation and principles of this theory—for monovalent salts—will be given.

The principal assumption of Poisson-Boltzmann theory is that all ions are charged point particles. A number of these ions belong to species that enter the solvent through an association–dissociation equilibrium at the colloidal surface, such that the colloidal particles make up a charge distribution $Q_{\text{coll}}(\mathbf{r})$ and the system is globally charge neutral. Additional ions can be added that belong to the same species, or other species, by adding salt. The easiest and most frequently used case involves added salt in the form of two ion species—of the same species as the dissociated ions—chosen to be monovalent positive and negative ions. Their charge is modelled as point charges of magnitude $\pm e$, and the potential energy $V_\pm$ of such an ion at position $\mathbf{r}$ is given by the corresponding electrostatic energy in an electrostatic potential Ψ,

$$V_\pm(\mathbf{r}) = \pm e\Psi(\mathbf{r}). \tag{1.1}$$

In turn, a particle gives rise to the Coulomb potential. Together, the ions and colloids

form a charge distribution $Q(\mathbf{r})$, and the corresponding potential reads

$$\Psi(\mathbf{r}) = \int \mathrm{d}\mathbf{r}' \frac{Q(\mathbf{r}')}{4\pi\varepsilon|\mathbf{r}-\mathbf{r}'|}. \tag{1.2}$$

where ε is the permittivity of the solvent. We assume that the suspension is index matched, such that ε is also the permittivity of the colloidal particles. The addition of salt ions is modelled as bringing the colloidal suspension in contact with a salt reservoir through a semi-permeable membrane and describing the exchange of ions grand-canonically. The salt ions and solvent molecules can traverse this membrane, but the colloidal particles cannot. The supply of ions is considered unlimited, such that both positive and negative ions have fixed chemical potentials $\mu_\pm$. Since we describe these particles as an ideal gas—or rather an ideal *plasma*—of charged point particles, we will set the reservoir density equal to the fugacity

$$\rho_\mathrm{s} = \frac{1}{\Lambda_\pm^3} \exp\left[\frac{\mu_\pm}{k_\mathrm{B}T}\right], \tag{1.3}$$

where $\Lambda_\pm$ are arbitrary interaction lengths. The reservoir salt density ρ_s is the usual parameter in Poisson-Boltzmann theory instead of the chemical potentials $\mu_\pm$, and it is equal to the density of both species, such that the *total* ion density in the reservoir is equal to $2\rho_\mathrm{s}$.

Now we consider the charge distribution in the electrolyte that is realized by the density distributions of the positive and negative ions

$$\rho_\pm(\mathbf{r}) = \rho_\mathrm{s} \exp\left[\mp\frac{e\Psi(\mathbf{r})}{k_\mathrm{B}T}\right], \tag{1.4}$$

that is,

$$Q_\mathrm{ion}(\mathbf{r}) = e\big[\rho_+(\mathbf{r}) - \rho_-(\mathbf{r})\big] = -2e\rho_\mathrm{s} \sinh\left[\frac{e\Psi(\mathbf{r})}{k_\mathrm{B}T}\right]. \tag{1.5}$$

The expression in Eq. (1.4) is the Boltzmann distribution of positive and negative ions corresponding to the description given above. We now insert this charge distribution into the Poisson equation, together with the colloid surface charge. The total charge distribution is given by $Q(\mathbf{r}) = Q_\mathrm{ion}(\mathbf{r}) + Q_\mathrm{coll}(\mathbf{r})$, for which we obtain

$$\nabla^2\Psi(\mathbf{r}) = -\frac{Q(\mathbf{r})}{\varepsilon} = \frac{2e\rho_\mathrm{s}}{\varepsilon} \sinh\left[\frac{e\Psi(\mathbf{r})}{k_\mathrm{B}T}\right] - \frac{Q_\mathrm{coll}(\mathbf{r})}{\varepsilon}. \tag{1.6}$$

This equation is called the Poisson-Boltzmann equation. It can be recast in a very convenient form by defining the dimensionless potential $\Phi = e\Psi/k_\mathrm{B}T$, such that

$$\nabla^2\Phi(\mathbf{r}) = \kappa^2 \sinh\Phi(\mathbf{r}) - \frac{4\pi l_\mathrm{B}}{e} Q_\mathrm{coll}(\mathbf{r}), \tag{1.7}$$

where $\kappa^{-1} = \sqrt{\varepsilon k_B T / 2e^2 \rho_s}$ is the Debye screening length, and $l_B = e^2/4\pi\varepsilon k_B T$ is the Bjerrum length. Our description of a charged colloidal system is not complete without appropriate boundary conditions on the colloidal particle surface. Since the ions cannot penetrate the interior of the colloidal particles, we may only apply the Poisson-Boltzmann equation in the electrolyte. Inside the particles—and in the absence of internal charge distributions—the Laplace equation holds,

$$\nabla^2 \Phi_{\text{in}}(\mathbf{r}) = 0. \tag{1.8}$$

The boundary conditions impose a continuous electrostatic potential, and a discontinuity of its derivative at the surface of each colloidal particle. This discontinuity is a result of the surface charge distribution. In the case that the suspension is *not* index matched, it is also influenced by the difference in dielectric constants of the medium and the particle.

From the description of an electrolyte as a mixture of charged ideal point particles, we can also derive the Poisson-Boltzmann equation using density functional theory (DFT) [33, 34]. The original—quantum-mechanical—version of DFT is based on the mathematical proof that there is a one-to-one mapping between the ground-state single-particle distribution of a system of interacting particles and the external potential applied to the system. It employs the same variational principle as the variational method used in quantum mechanics to approximate the ground state of a system for a given Hamiltonian. However, DFT does not rely on a specific set of trial wave functions. Instead, it determines the minimum of a (free-)energy functional in terms of a density profile, which is directly related to the wave function of the system. One applies a Born-Oppenheimer approximation to distinguish the interacting particles—which make up this density profile—from the particles that establish an "external" potential. In the context of quantum chemistry, in order to describe a system consisting of nuclei and electrons, the approximation is that the electrons move much faster than the nuclei. Thus, the latter effectively create an external potential for the former. Given specific positions of the nuclei, the ground state of the many-body system of electrons is found. The inhomogeneous electron system in turn gives rise to the (effective) potential of mean force between the nuclei. From this description, in principle, a prediction can be made of the structural and (thermo)dynamic properties of atoms, molecules, and solids [35].

The analogy with soft condensed matter systems is easily made. The colloidal particles play the role of the nuclei, and the ions that of the electrons. The free-energy functional is minimized with respect to the thermal average of the ion density. In our case, this yields two density distributions: one for the positive ions and one for the negative ions. We find the Poisson-Boltzmann equation by minimizing the grand-potential functional of a mixture of positive and negative monovalent point ions, in

which the electrostatic energy is treated in a mean-field description,

$$\beta\Omega[\rho_\pm] = \sum_{\alpha=\pm}\int \mathrm{d}\mathbf{r}\rho_\alpha(\mathbf{r})\left[\ln\frac{\rho_\alpha(\mathbf{r})}{\rho_\mathrm{s}}-1\right]+\frac{l_\mathrm{B}}{2e^2}\int\mathrm{d}\mathbf{r}\int\mathrm{d}\mathbf{r}'\,Q(\mathbf{r})Q(\mathbf{r}')G(\mathbf{r},\mathbf{r}'), \quad (1.9)$$

where $\beta = 1/k_\mathrm{B}T$, $Q(\mathbf{r}) = e\left[\rho_+(\mathbf{r})-\rho_-(\mathbf{r})\right]+Q_\mathrm{coll}(\mathbf{r})$, and $G(\mathbf{r},\mathbf{r}')$ is a Green's function that satisfies the appropriate boundary conditions. The equilibrium profile of each ion species is determined by the condition

$$\frac{\delta\Omega}{\delta\rho_\pm(\mathbf{r})} = 0. \quad (1.10)$$

This condition yields the Boltzmann distribution for each ion species

$$\rho_\pm(\mathbf{r}) = \rho_\mathrm{s}\exp\left[\mp\Phi(\mathbf{r})\right], \quad (1.11)$$

where

$$\Phi(\mathbf{r}) = \frac{l_\mathrm{B}}{e}\int\mathrm{d}\mathbf{r}'\,Q(\mathbf{r}')G(\mathbf{r},\mathbf{r}'). \quad (1.12)$$

We have chosen a general Green's function to represent the pair interaction of the ions, although in the particular case that the electrolyte is composed only of ions in an infinite solvent of permittivity equal to the colloid permittivity, one can use the Coulomb potential $G(\mathbf{r},\mathbf{r}') = 1/|\mathbf{r}-\mathbf{r}'|$. If the electrolyte contains particles or inhomogeneities of different permittivity, one is still allowed to use the Coulomb potential, but additional terms should be added in Eqs. (1.9) and (1.12). This is also the case if one applies an external field, although this subject is beyond the scope of this thesis. Upon inserting the obtained solutions for the ion-density distributions and the electrostatic potential into the grand-canonical free energy (1.9), we obtain the equilibrium grand potential

$$\beta\Omega_\mathrm{eq} = \rho_\mathrm{s}\int\mathrm{d}\mathbf{r}\left[\Phi(\mathbf{r})\sinh\Phi(\mathbf{r})-2\cosh\Phi(\mathbf{r})\right]+\frac{1}{2e}\int\mathrm{d}\mathbf{r}\,\Phi(\mathbf{r})Q_\mathrm{coll}(\mathbf{r}). \quad (1.13)$$

Note that the expression in Eq. (1.13) is not a functional, as $\Phi(\mathbf{r})$ here denotes the *solution* of the PB equation (1.7), which is equivalent to the equilibrium condition (1.10).

1.4 Debye-Hückel theory and the DLVO potential

Poisson-Boltzmann theory—as introduced in Sec. 1.3—is an inherently nonlinear many-body problem. However, the most basic application—the dilute monovalent-salt solution in the presence of low-to-moderately charged colloidal particles—justifies the

use of the linearized Poisson-Boltzmann (LPB) equation, also known as the Debye-Hückel approach [36, 37]. For the purpose of illustration, we solve the LPB equation for the case of colloidal point particles described by the colloidal charge distribution

$$Q_{\mathrm{coll}}(\mathbf{r}) = Ze \sum_{i=1}^{N} \delta(\mathbf{r} - \mathbf{R}_i), \tag{1.14}$$

where Z is the number of elementary charges on the colloidal particle. The LPB equation in this case is given by

$$\nabla^2 \Phi(\mathbf{r}) = \kappa^2 \Phi(\mathbf{r}) - 4\pi Z l_{\mathrm{B}} \sum_{i=1}^{N} \delta(\mathbf{r} - \mathbf{R}_i). \tag{1.15}$$

The solution to this equation is reasonably easy to obtain analytically, for the boundary condition that the potential vanishes infinitely far away from the colloidal particles. It is given by a multi-centered *screened* Coulomb potential (or Yukawa potential), which describes the potential of a charged test particle at position $\mathbf{r}$,

$$\Phi(\mathbf{r}) = Z l_{\mathrm{B}} \sum_{i=1}^{N} \frac{\exp[-\kappa|\mathbf{r} - \mathbf{R}_i|]}{|\mathbf{r} - \mathbf{R}_i|}. \tag{1.16}$$

The equilibrium free energy (1.13) is also linearized with respect to the potential Φ, and the solution (1.16) is inserted, with exception of the self energy of the colloidal particles,

$$\beta \Omega_{\mathrm{eq}} \simeq Z^2 l_{\mathrm{B}} \sum_{i=1}^{N} \sum_{j=i+1}^{N} \frac{\exp[-\kappa|\mathbf{R}_i - \mathbf{R}_j|]}{|\mathbf{R}_i - \mathbf{R}_j|}. \tag{1.17}$$

Interestingly, in this approach the total (free) energy of the system is simply given by the summation of pair interactions between all colloidal particles. An *effective* pair interaction between two colloidal particles naturally arises,

$$\beta V_{\mathrm{DH}}^{\mathrm{pair}}(\mathbf{r}, \mathbf{r}') = Z^2 l_{\mathrm{B}} \frac{\exp\left[-\kappa|\mathbf{r} - \mathbf{r}'|\right]}{|\mathbf{r} - \mathbf{r}'|}. \tag{1.18}$$

Essentially, this expression gives the potential of mean force between two charged point particles in the background of ions.

The most frequently applied approximation of the effective pair interaction between colloidal particles is due to Derjaguin, Verwey, and Overbeek [38, 39], although it is regularly attributed additionally to Derjaguin's co-worker Landau (DLVO). It is an approximation of the electrostatic energy—together with the effect of the osmotic pressure of the ions—of two homogeneously charged colloidal spheres in the vicinity of each other. The original description includes an additional contribution to the

pair potential due to short-ranged Van der Waals attractions. However, throughout this thesis, we assume that these attractions are either suppressed—e.g., by index matching or steric stabilization—or that they are irrelevant because of the large interparticle distances—e.g., due to electrostatic repulsions (charge stabilization). Therefore, we restrict ourselves to the electrostatic part. This part has the same form as Eq. (1.18), but instead of a charge Ze, it describes the pair potential of two point particles of effective charge

$$Q^{\text{eff}} = \frac{\exp[\kappa a]}{1+\kappa a} Ze, \tag{1.19}$$

where a is the colloidal radius. The LPB equation can be solved exactly for a single homogeneously charged sphere, for which the resulting single-particle potential is equal to the potential of a point particle of charge Q^{eff}. The approximations leading to the DLVO potential basically apply this amplitude to approximate the amplitude of the pair potential. However, the resulting expression can be mathematically derived by approximating the force exerted by one particle onto another—from which one derives the potential of mean force [39]—or applying a Derjaguin approximation on the pair interaction of two charged plates [38]. Alternatively, the exact electrostatic energy of the specific configuration of two homogeneously charged spheres can be expressed in terms of an infinite series [40], which can be truncated yielding the same expression. The resulting effective pair potential is

$$\beta V_{\text{DLVO}}^{\text{pair}}(\mathbf{r},\mathbf{r}') = \frac{l_{\text{B}} \left(Q^{\text{eff}}\right)^2}{e^2} \frac{\exp\left[-\kappa|\mathbf{r}-\mathbf{r}'|\right]}{|\mathbf{r}-\mathbf{r}'|}. \tag{1.20}$$

This expression can also be derived from DFT [41]. However, the calculation contains subtleties that influence the expression that one obtains for the proportionality constant between the effective point charge Q^{eff} and the colloidal surface charge Ze [42].

1.5 Overview

In chapter 2, we investigate short homogeneously charged colloidal rods. We develop a model to investigate the influence of charge on the anisotropic pair interaction. The phase behavior of these charged rods is compared to—and mapped onto—that of *uncharged* rods. Chapters 3–6 treat systems of heterogeneously charged colloidal spheres. We apply the concept of charge renormalization—which makes a connection between the nonlinear and linearized versions of Poisson-Boltzmann theory—to Janus particles in chapter 3. In addition, we make a connection to Onsager's model for the isotropic–nematic transitions in systems of rods. To this end, we extend the Poisson-Boltzmann cell model to include a description of orientational distributions of these

particles. This model is presented in chapter 4. We consider fluids of these particles in chapter 5, and address the question if such systems can undergo orientational ordering in the absence of positional ordering (isotropic–nematic). We do this with the use of bifurcation theory, which is well known from its application to Onsager's model [43]. Finally, we repeat this analysis in a different setting in chapter 6. There, in contrast to translational symmetry, we impose a crystal structure on the particles, fixing their positions on a cubic lattice. Then we perform the search for rotational-symmetry breaking (plastic-crystal–crystal).

Chapter 2

Short charged rods
Effective shape and phase behavior

Abstract

We explicitly calculate the orientation-dependent second virial coefficient of short charged rods in an electrolytic solvent, assuming the rod-rod interactions to be a pairwise sum of hard-core and segmental screened-Coulomb repulsions. From the parallel and isotropically averaged second virial coefficient, we calculate the effective length and diameter of the rods, for charges and screening lengths that vary over several orders of magnitude. Using these effective dimensions, we determine the phase diagram, where we distinguish a low-charge and strong-screening regime with a liquid crystalline nematic and smectic phase, and a high-charge and weak-screening regime with a plastic crystal phase in the phase diagram.

2.1 Introduction

The study of suspensions of nonspherical colloidal particles started with the experimental works of Zocher [44] and Bawden et al. [45], and with Onsager's theoretical work [20]. It has since developed into a very versatile field of research. A lot of attention has been focused on needle-shaped rods, either naturally occurring ones such as viruses like tobacco mosaic virus or fd virus [21, 23, 45], or laboratory synthesized ones such as Boehmite rods [22]. In recent years, however, a plethora of nonspherical particles have been synthesized that are not extremely elongated, for example,

ellipsoidal colloids with aspect ratio ~ 3 [3], colloidal dumbbells [2], or nanoparticles with the shape of a rod, disk, snowman, cube, cap, or raspberry [4–10]. These particles are often charged when dissolved in a polar solvent such as water, and hence their pair interactions involve not only the anisotropic steric short-range repulsions but also electrostatic long-range repulsions. The strength of the latter is determined by the charge on the particle and the range is determined by the Debye screening length of the solvent [38, 39]. For small charges and strong screening (i.e., high salt concentrations), one expects the steric interactions to be dominant (if we assume that dispersion forces can be neglected). Hence, one can use computer simulations or theoretical studies of *hard* anisotropic bodies [19, 46–50] to obtain an idea of the phase diagram of the system as a function of concentration. In the case of a high charge or weak screening (i.e., low salt concentration), however, the situation is less clear cut. There, the degree of anisotropy of the electrostatic interactions is not obvious from the outset: on the one hand one expects the soft screened-Coulomb interactions to wash out the hard-core anisotropy such that the interactions become effectively more spherically symmetric, while on the other hand there are the intriguing findings reported, for example, in Refs. [51, 52]. The studies in these papers apply to systems of charged anisotropic particles in a screening medium. It was found that the electrostatic anisotropy persists to infinitely large distances as the asymptotic decay of each multipole contribution to the electrostatic potential due to a nonspherical charge distribution is equal [51, 52]. This conclusion is in sharp contrast to the case of a charge distribution in vacuum, where the monopole potential decays more slowly than that of the dipole, as each order multipole contribution decays slower than the next one does. In this chapter we investigate the interplay between hard-core and electrostatic interactions for nonspherical particles, for the relatively simple particle shape of spherocylinders.

It is well established by now that nonspherical colloidal particles can form a wealth of phases in thermodynamic equilibrium. Needlelike colloidal rods, for instance, form a phase sequence *I*–*N*–Sm–*X* upon increasing the concentration from very dilute up to close packing, where *I* is the completely disordered isotropic fluid phase, *N* the liquid crystalline nematic phase with orientational ordering, Sm the smectic-*A* phase built from orientationally ordered liquidlike layers, and *X* a fully ordered crystal phase [19–21, 44, 53–57]. This phase sequence for colloidal needles is well established for hard-core interactions [19, 53, 55]. Also, for softer electrostatic screened-Coulomb repulsions in the case of charged needles, at least in the regime where the length of the rods is much larger than the diameter and the screening length of the electrolytic solvent. This ensures that the effective diameter of the rods is much smaller than the length [21, 58]. By contrast, particles with shapes that are sufficiently close to spherical are *not* expected to exhibit the liquid crystalline phases *N* and Sm due to

their small anisotropy. Instead, for such near-spherical particles one would expect a plastic crystalline phase (P) to appear in the phase diagram, residing in between the isotropic fluid and the fully ordered crystal. The P phase is characterized by positional ordering on a lattice, but without long-ranged orientational ordering of the particles. For instance, a phase sequence I–P–X upon increasing the concentration has indeed been established in simulations of short hard spherocylinders and of hard dumbbells with a length-to-diameter ratio smaller than about 0.35 [19, 59, 60]. The question we address in this chapter concerns the effect of colloidal charge and ionic screening on the effective shape of relatively short rods, and on their expected phase sequence upon increasing the concentration. On the basis of the well established increase of the effective diameter of charged needles compared to their hard-core diameter [58], it is to be expected that high colloidal charges and weak-screening conditions (i.e., low salt concentrations) lead to a decreased anisotropy of short charged rods. Hence, this will lead to a larger tendency of the system to exhibit a plastic crystal phase instead of liquid crystalline phases in the phase diagram, even if the hard-core shape would allow for liquid crystalline equilibrium phases.

Of course, suspensions of charged rods have been extensively studied theoretically before. Many of these studies are based on Onsager's second virial theory for hard rods [20], which is modified and extended to take into account the effects of charge and screening on the isotropic-to-nematic transition [58, 61–65]. Some of these studies, for example, those of Refs. [20, 58, 62], focus on the needle limit in which the rod length is very large compared to the screening length. In this limit, only the diameter is affected by the electrostatic effects, but in such a way that the effective geometry of the rod remains needlelike. In Refs. [61, 64] rod lengths of the order of (or larger than) the Debye length are considered, at the expense, however, of ignoring many of the prefactors such that the theory is essentially a scaling theory. Interestingly, this scaling theory predicts nematic–nematic coexistence in some parameter regime, which was later confirmed in Ref. [63]. This coexistence regime is characterized by a small rod charge density, such that the effective geometry of the rod is no longer needlelike. Another limit that was studied in detail is the limit of weak electrostatic interactions, which naturally leads to a perturbative description [63, 66, 67]. These schemes are very successful at describing the effective (non-needlelike) geometry that shows up in the angular dependence of the second virial coefficient. Another very interesting effect was identified in Ref. [65], where the correlation free energy of the many-body system of charged rods and counterions was calculated, resulting in an enhanced tendency to orientational ordering and also the possibility of nematic–nematic coexistence. With the notable exception of Ref. [67], however, most of these works on charged rods focus on the isotropic and nematic phases and hence, implicitly, on rods which are sufficiently elongated to give liquid crystalline phases at all.

In this chapter we take a slightly different perspective. We explicitly calculate the orientation-dependent second virial coefficient of rather short charged rods numerically, for colloidal charges and screening lengths that vary over many decades. Such calculations, in which we use expansions in spherical harmonics, do not require only the asymptotic far-field expressions of the multipoles (such as considered in Refs. [51, 52]), but in fact their full distance dependence. From the resulting second virial coefficient, we determine an effective hard-core length and diameter. Subsequently, we use these—in combination with the published hard-core phase diagram [19]—to determine the expected phase sequence upon increasing the concentration. This scheme is too crude to distinguish subtleties such as whether or not there is a nematic-nematic coexistence regime or to what extent the isotropic-nematic phase gap is affected. However, it is supposed to indicate reliably whether liquid crystalline (N and Sm) or plastic crystal (P) phases are to be expected in between the isotropic (I) and crystalline (X) phase. We focus on the case where the rod length is of the order of the screening length or smaller, in contrast to most of the previous theoretical work. This is the regime where the crossover from N and Sm to P is expected to occur. In the limit where the rod length is small and the hard-core interactions are important, we give a simplified theoretical description that turns out to be in remarkable agreement with the numerical results. As our numerical approach relies on an expansion in spherical harmonics of the effective pair interaction between two rods, it leads to explicit but involved expressions. We present some of the mathematical technicalities of the derivation of these expressions in appendix A.

2.2 Model

We consider a system of identical charged colloidal rods suspended in an electrolyte solvent of permittivity ε, Bjerrum length $l_{\mathrm{B}} = e^2/(4\pi\varepsilon k_{\mathrm{B}}T)$, and Debye screening length κ^{-1}, at temperature T. Here e is the elementary charge, and k_{B} is the Boltzmann constant. The rods are assumed to have the shape of a spherocylinder consisting of a cylinder of length L and diameter D capped by two hemispheres also of diameter D. The rods have a fixed charge, which we treat here as an (effective) line-charge density $e\lambda$ distributed homogeneously over a length L on the axis of the cylinder. In principle, the details of the actual charge distribution—for example, a homogeneous surface charge density—could be taken into account. However, the treatment of these details would greatly complicate the analysis is this chapter, even if we limit ourselves to applying an *inhomogeneous* effective line charge distribution. Possible improvements on our description are discussed in Sec. 2.7. We are interested in the effective pair potential $V(\mathbf{r};\hat{\omega},\hat{\omega}')$ between two rods with orientations $\hat{\omega}$ and $\hat{\omega}'$ at a center-

to-center vector $\mathbf{r}$, thermally averaged over the degrees of freedom of the electrolyte solvent (characterized by κ^{-1} and l_B). In the spirit of Derjaguin, Landau, Verwey and Overbeek (DLVO), we assume that the effective pair potential consists of steric hard-core repulsions and electrostatic screened-Coulomb interactions between segments of the line charge of the two rods. We ignore short-ranged van der Waals attractions (i.e., we assume the particle and the solvent to be index matched or that the dispersion forces are canceled by steric or charge stabilization). Within these approximations the effective pair potential can be written as

$$\beta V(\mathbf{r};\hat{\omega},\hat{\omega}') = \begin{cases} \infty & \text{for overlapping rods,} \\ \\ \beta V_e(\mathbf{r};\hat{\omega},\hat{\omega}') & \text{otherwise,} \end{cases} \tag{2.1}$$

where $\beta^{-1} = k_B T$, the overlap refers to the hard-core repulsions, and the electrostatic interaction potential is given by

$$\beta V_e(\mathbf{r};\hat{\omega},\hat{\omega}') = l_B \lambda^2 \int_{-\frac{L}{2}}^{+\frac{L}{2}} \mathrm{d}l \int_{-\frac{L}{2}}^{+\frac{L}{2}} \mathrm{d}l' \, \frac{\exp[-\kappa|\mathbf{r}+l'\hat{\omega}'-l\hat{\omega}|]}{|\mathbf{r}+l'\hat{\omega}'-l\hat{\omega}|}. \tag{2.2}$$

The integration variables l and l' play the role of coordinates running along the cylinder axes of each of the two rods, from one end of the cylinder to the other end. In the long-rod limit, $L/D \gg 1$ and $\kappa L \gg 1$, one can replace the integration domains in Eq. (2.2) by the full real axis, together with the constraint that the cylinder axes are in "cross configuration" (i.e., the axes intersect when projected onto the plane parallel to both axes). For other configurations, the potential becomes negligible. One then easily shows that V_e only depends on the shortest distance and the relative angle between the two rods [20, 58, 63]. Here we focus on shorter rods, for which this simplification does not apply. In appendix A we derive systematic series expansions in spherical harmonics to describe the angular and position dependence of V_e explicitly, focusing on rods with cylinder axes that are rather short compared to the Debye screening length (which sets the range of the electrostatic repulsions). More specifically, the expansion of the angular dependence is truncated and we consider each term as an expansion in κL up to fourth order (see Sec. A.4). We compare the result with the large-κL limit.

The present model can be characterized by a few dimensionless combinations. In the limit of uncharged rods ($\lambda = 0$), the aspect ratio L/D of the hard-core dimensions is of primary importance. However, for the charged rods of present interest, the ratio κL (of the hard-core length to the Debye screening length of the solvent) gives more information on the interaction anisotropy. The ratio κD is relevant as a measure of ionic strength. Dimensional inspection of the expression in Eq. (2.2) shows that the strength of the electrostatic interactions is proportional to the dimensionless (square

of the) line charge density

$$q \equiv \frac{l_B \lambda^2}{\kappa}. \tag{2.3}$$

These dimensionless combinations can span quite a range of numerical values in experimental systems. For instance, for fd virus suspended in water one finds [23] $L/D > 100$, $\kappa D \simeq 0.1$–1, and $q = 70$–700, and recently synthesized silica dumbbells in oily solvents [68] are best characterized by $L/D \simeq 1$, $\kappa D \simeq 1$, and $q \simeq 100$. Short (double stranded) DNA chains have $\kappa D \simeq 0.1$–1 and $q \simeq 0.1$–10, while their length can be varied by the number of base pairs included in the sequence. These chains can be characterized as rigid rods up to the persistence length corresponding to $L/D \simeq 50$. Moreover, present-day synthesis techniques allow for the tuning of surface charge, in principle at least, from essentially vanishing to extremely high. This is achieved, for example, by using different coatings with varying degrees of ion dissociation of the surface groups. It is therefore of interest to investigate the thermodynamics of the present model over a wide range of parameters.

2.3 Thermodynamics and Effective dimensions

With the pair potential specified by Eqs. (2.1) and (2.2), and with an explicit scheme to evaluate it as explained in appendix A, we can study the macroscopic properties of suspensions of these charged rods. In principle, we do this as a function of concentration, for various q, κD, and L/D. Here we circumvent the complexity of the full statistical-mechanical calculation of free energies and phase diagrams of the system at hand. We do this by mapping the second virial coefficient of the *charged* spherocylinders of interest onto that of *hard* spherocylinders with an effective cylinder length $L_{\rm eff}$ and an effective diameter $D_{\rm eff}$ that we will calculate below. We then *presume* that the phase diagram of the system of charged rods follows from that of the effective hard-rod system, which we take from published computer simulation data [19]. It is well known from these and follow-up simulations of hard rods, as well as density functional theory [53, 55], that this system exhibits a sequence of phase transitions upon increasing the concentration that strongly depends on the aspect ratio L/D: sufficiently elongated hard rods with $L/D > 3.7$ have an isotropic–nematic–smectic–crystal (*I*–*N*–Sm–*X*) phase sequence, sufficiently short hard rods $0 < L/D < 0.35$ show an *I*–*P*–*X* sequence with *P* a plastic crystal, and in between there are two more regimes in which the *N* and *P* phase, respectively, no longer appear in the phase sequence. Below we determine how the analogous crossovers between these regimes of the effective system, as determined by $L_{\rm eff}/D_{\rm eff}$, depend on the parameters q, κD, and L/D.

A key ingredient of our calculation is the effective excluded volume $E(\hat{\omega}, \hat{\omega}')$ of

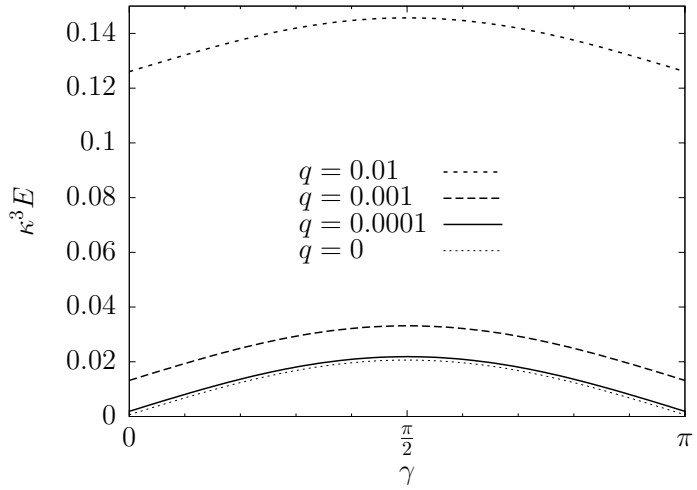

Figure 2.1: The effective excluded volume $\kappa^3 E$, as a function of the angle γ between the two rod orientations, for different values of the charge parameter q. We used the parameter values $\kappa L = 1$ and $\kappa D = 0.01$ (such that $L/D = 100$).

two charged rods with orientations $\hat{\omega}$ and $\hat{\omega}'$, defined as

$$E(\hat{\omega},\hat{\omega}') = \int \mathrm{d}\mathbf{r} \left(1 - \exp\left[-\beta V(\mathbf{r};\hat{\omega},\hat{\omega}')\right]\right), \tag{2.4}$$

where the pair potential between the rods is given in Eqs. (2.1) and (2.2). Note that $E(\hat{\omega},\hat{\omega}')$ is in fact twice the corresponding second virial coefficient, and that the nomenclature "effective excluded volume" stems from the fact that it reduces to the actual excluded volume of the pair in the case of purely hard-core interactions. On the basis of symmetry arguments one easily checks that the angular dependence of $E(\hat{\omega},\hat{\omega}')$ is in fact only through the angle $\gamma = \arccos(\hat{\omega}\cdot\hat{\omega}')$ between the cylinder axes of the two rods. In Fig. 2.1 we show this γ dependence of E for rods characterized by $\kappa L = 1$ and $\kappa D = 0.01$ (so $L/D = 100$ and weak screening), for several charge parameters q ranging from $q = 0$ (uncharged) to $q = 0.01$ (fairly charged). The results of Fig. 2.1 stem from a combination of numerical and analytic procedures explained in detail in appendix A. These involve a fivefold integration: over the contour of the rods l and l' in Eq. (2.2), and the center-to-center separation vector $\mathbf{r}$ in Eq. (2.4).

The key observations from Fig. 2.1, which is typical for many choices of system parameters, are that for increasing q the effective excluded volume becomes (i) less anisotropic, and (ii) larger in magnitude. Moreover, for all q the effective excluded

volume is larger for perpendicular orientations than for parallel ones. Qualitatively, and in fact quantitatively for many parameters, this behavior is identical to that of *hard* spherocylinders of effective length $L_{\rm eff}$ and diameter $D_{\rm eff}$, for which the excluded volume is given by [20]

$$\mathcal{V}_{\rm eff}(\hat{\omega},\hat{\omega}') = \frac{4\pi}{3}D_{\rm eff}^3 + 2\pi L_{\rm eff}D_{\rm eff}^2 + 2L_{\rm eff}^2 D_{\rm eff}\sin\gamma. \tag{2.5}$$

In principle one can fit the functional form of Eq. (2.5) to the numerical results such as those of Fig. 2.1 to determine the effective hard-core dimensions $L_{\rm eff}$ and $D_{\rm eff}$ for given charged-rod parameters. However, instead of fitting the full angular dependence numerically, it is more convenient to match the isotropically averaged effective excluded volume and the parallel one, given by

$$E_{\rm iso} = \frac{1}{(4\pi)^2}\int {\rm d}\hat{\omega}\int {\rm d}\hat{\omega}'\, E(\hat{\omega},\hat{\omega}') = \frac{1}{2}\int_0^\pi {\rm d}\gamma \sin\gamma E(\gamma), \tag{2.6}$$

$$E_\parallel = E(\hat{\omega},\hat{\omega}) = E(\gamma=0), \tag{2.7}$$

to the values for spherocylinders with effective hard-core dimensions $L_{\rm eff}$ and $D_{\rm eff}$

$$\mathcal{V}_{\rm iso} = \frac{4\pi}{3}D_{\rm eff}^3 + 2\pi L_{\rm eff}D_{\rm eff}^2 + \frac{\pi}{2}L_{\rm eff}^2 D_{\rm eff}, \tag{2.8}$$

$$\mathcal{V}_\parallel = \frac{4\pi}{3}D_{\rm eff}^3 + 2\pi L_{\rm eff}D_{\rm eff}^2, \tag{2.9}$$

respectively. This procedure yields the effective hard-core dimensions

$$D_{\rm eff} = \left[\frac{3E_\parallel}{4\pi}\left(1+3\Delta-\sqrt{3\Delta(2+3\Delta)}\right)\right]^{\frac{1}{3}}, \tag{2.10}$$

$$\frac{L_{\rm eff}}{D_{\rm eff}} = 2\Delta + \frac{2}{3}\sqrt{3\Delta(2+3\Delta)}, \tag{2.11}$$

where we used, for notational convenience, the dimensionless anisotropy parameter Δ defined as

$$\Delta \equiv \frac{E_{\rm iso}-E_\parallel}{E_\parallel}. \tag{2.12}$$

It turns out that inserting $L_{\rm eff}$ and $D_{\rm eff}$ as obtained from Eqs. (2.10), (2.11), and (2.12) into Eq. (2.5) gives an angular dependence that is in very good agreement with the numerically obtained effective excluded volume of charged rods.

It is also interesting to compare our numerical results with analytic expressions that are valid in the limit where $L/D \gg 1$ and $\kappa L \gg 1$, as obtained by Stroobants et al. [58]. In this needle limit the effective excluded volume is given by

$$E_\infty(\gamma) = 2L^2\kappa^{-1}\sin\gamma\left[\gamma_{\rm E} + \ln 2\pi q - \ln\sin\gamma + \Gamma\left(0, \frac{2\pi q\exp[-\kappa D]}{\sin\gamma}\right)\right], \tag{2.13}$$

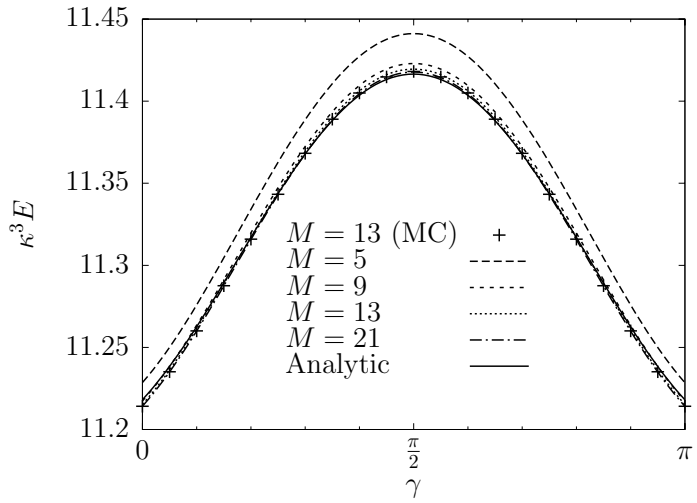

Figure 2.2: The effective excluded volume $\kappa^3 E$, as a function of the angle γ between the rod orientations, calculated using different numerical schemes (see text), involving M discrete charges, Monte Carlo (MC) integration, and the present analytic approach. We used the parameter values $\kappa L = 1$, $\kappa D = 0.25$ (such that $L/D = 4$), and $q = 1$.

where $\gamma_{\rm E} \approx 0.577$ is the Euler-Mascheroni constant and where the incomplete gamma function (or exponential integral) is defined by

$$\Gamma(\alpha, x) = \int_x^\infty \mathrm{d}y\, y^{\alpha-1} \exp[-y]. \tag{2.14}$$

From this expression—using the Onsager limit $\mathscr{V}_{\rm iso,\infty} = (\pi/2) L^2 D_{\rm eff,\infty}$ for the isotropically averaged excluded volume—the effective diameter is calculated

$$\kappa D_{\rm eff,\infty} = \gamma_{\rm E} + \ln 2\pi q + \ln 2 - \frac{1}{2} + \frac{2}{\pi} \int_0^\pi \mathrm{d}\gamma \sin^2\gamma\, \Gamma\left(0, \frac{2\pi q \exp[-\kappa D]}{\sin\gamma}\right). \tag{2.15}$$

The effective length is taken equal to the rod length $L_{\rm eff,\infty} = L$.

2.4 Numerical Results

Calculations such as those represented Fig. 2.1 are reasonably accurate for values of κL roughly up to 2. For higher values the applied approximations become poor, such that for $\kappa L \gtrsim 3$ the calculations become even qualitatively unreliable for many of our

parameters. For this reason we restrict most of our attention to the regime where $\kappa L \leq 2$.

In order to assess the accuracy of our calculations, we compare some of the results of our calculations with those obtained from more extensive numerical integration schemes. One is given by the same spatial integration scheme as before, but with the (effective) line-charge density replaced by a discrete charge distribution similar to the one applied by Graf and Löwen [67]. The rod charge is represented by an odd number of charge units ($M = 2N + 1$) distributed evenly on the cylinder axis, where one unit is always located on the center of the axis, and two units are always located on the two end points of the axis. The latter are of magnitude $e\lambda L/(4N)$, while all others are of magnitude $e\lambda L/(2N)$. This ensures that the total charge is $e\lambda L$ and the continuum limit $N \to \infty$ yields the correct homogeneous line charge. The other scheme uses the same discrete charge density as described above, but uses a Monte Carlo (MC) scheme to perform the integration. This scheme is denoted by the plusses in Fig. 2.2. The agreement between the results obtained from the different schemes, as shown in Fig. 2.2, is excellent for $M \geq 13$, particularly when considering that the shape of the effective excluded volume differs significantly from the hard-core case for these parameters. Therefore, we conclude that our calculation correctly predicts the angular dependence of the effective excluded volume of short charged rods.

In the previous section, we have shown that the angular dependence of the effective excluded volume can be used to calculate the effective rod dimensions L_{eff} and D_{eff}—from the values of $E_{\parallel}$ and $E_{\perp}$—by applying Eqs. (2.10), (2.11), and (2.12). Figure 2.3(a) shows the numerically calculated effective diameter as a function of the real diameter for $\kappa L = 1$ and a range of charge parameters q. Figure 2.3(b) shows the same function, but then for $q = 10$ and a range of rod lengths κL. Note that all (effective) rod dimensions are expressed in units of the screening length. In Fig. 2.3(b) the needle limit $\kappa L \gg 1$, given by Eq. (2.15), is plotted for comparison. Both graphs clearly reveal two regimes,

$$D_{\text{eff}} \simeq \begin{cases} D_{\text{e}} & \text{for } D \ll D_{\text{e}}, \\ \\ D & \text{for } D \gg D_{\text{e}}. \end{cases} \tag{2.16}$$

These can be identified as an electrostatic regime at small (or intermediate) κD (weak screening) and a hard-core regime at high enough κD (strong screening). In the hard-core regime, the effective diameter equals the hard-core diameter, while in the (weakly screened) electrostatic regime the effective diameter saturates to a plateau value D_{e}. This electrostatic effective diameter depends on q and κL, and increases with increasing q and κL. Also, it is (much) larger than the hard-core diameter due to the (strong) rod-rod repulsions. Values of the electrostatic effective diameter are included

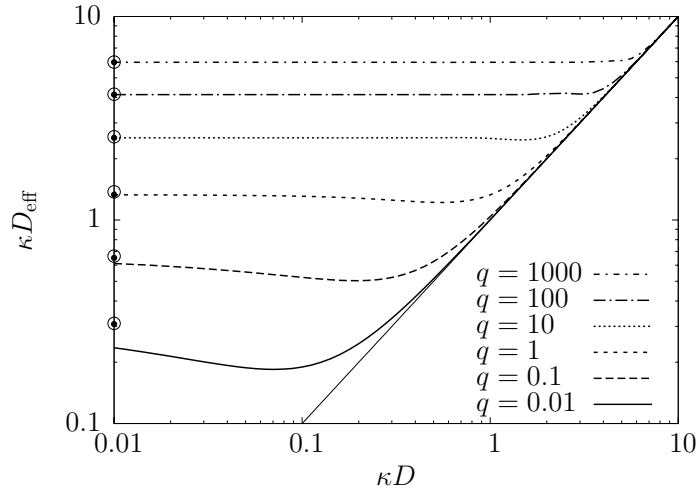

(a)

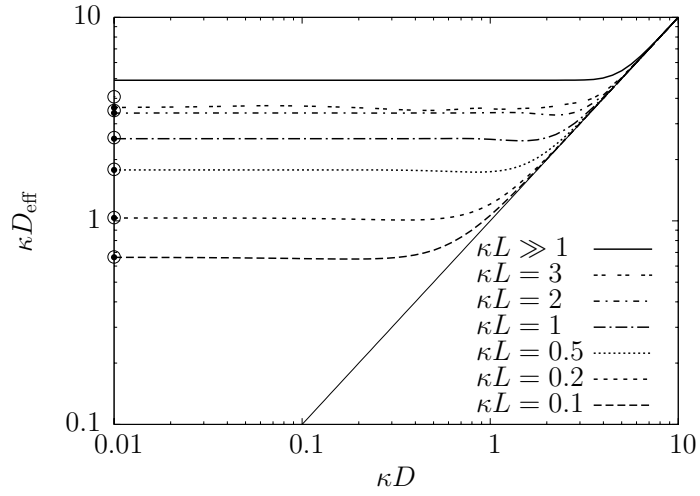

(b)

Figure 2.3: The effective diameter $\kappa D_{\rm eff}$ as a function of the rod diameter κD for (a) $\kappa L = 1$ and different values for the charge parameter q; (b) $q = 10$ and different values for the rod length κL. The rod dimensions are scaled by the screening length κ^{-1}. The thin solid line is a guide to the eye, representing the hard-core limit $D_{\rm eff} = D$. The small solid circles give the values for $\kappa D = 0$ from the numerical calculations. The larger open circles are obtained by the approximation given in Eq. (2.17).

in Fig. 2.3, where the small solid circles represent values obtained from numerical calculations for $\kappa D = 0$. The larger open circles represent the following simple approximation for D_e.

In the short-rod limit, we can treat the double layer around the rod as spherically symmetric, with an effective point charge $e\lambda L$ in the center, such that also the pair potential is spherically symmetric. We then approximate the effective excluded volume (2.4) by inserting this spherically symmetric pair interaction. This gives $\Delta = 0$, and hence from Eq. (2.10), for large enough q (or small enough κD), we obtain the electrostatic effective diameter from the simple expression

$$\kappa D_e \simeq \left[3\int_0^\infty \mathrm{d}x\, x^2 \left(1 - \exp\left[-q\kappa^2 L^2 \frac{\exp[-x]}{x}\right]\right)\right]^{\frac{1}{3}}. \tag{2.17}$$

This approximation is given in Fig. 2.3 by the larger open circles. Both graphs together show good agreement between the solid and open circles, for $\kappa L \leq 1$ and all values for q. Figure 2.3(b) also shows that the regime $\kappa L \leq 2$—which is reliably accessible with our truncated numerical scheme—evolves smoothly to the needle limit $\kappa L \gg 1$ of Stroobants et al. [58]. The slight drop in the curve for $\kappa L = 3$ between $\kappa D \simeq 0.1$ and $\kappa D \simeq 1$ indicates the numerical instabilities we encounter for larger values of κL.

In a similar fashion we can also study the effective length L_{eff} of the rods. Figure 2.4(a) shows results of numerical calculations of the effective rod length for $\kappa L = 1$ and a range of charge parameters q. Figure 2.4(b) is the result for $q = 10$ and a range of rod lengths κL. The rod dimensions are expressed in units of the Debye length, whereas L_{eff} is expressed in units of the hard-core length. We distinguish again two asymptotic regimes, the strong-screening (hard core) regime $\kappa D \gg 1$ where $L_{\mathrm{eff}} = L$, and the weak-screening (electrostatic) regime $\kappa D \ll 1$ where L_{eff} reaches a plateau value that depends on q and κL. Note also that $L_{\mathrm{eff}} < L$ which is perhaps unexpected at first sight. Naively, one could expect the effective length to increase with increasing effective excluded volume. However, as Sato and Teramoto [62] pointed out, the effective length decreases with increasing rod charge density because of end effects. Thus, the increase of the effective excluded volume—due to the increase of the rod charge density—is purely caused by the increase of the effective diameter. Moreover, this increase balances the decrease in effective length such that the total effective particle length $L_{\mathrm{eff}} + D_{\mathrm{eff}}$ does increase with increasing rod charge density. Inspection of Fig. 2.4(a) also reveals numerical (convergence) problems for $q \geq 100$ at $\kappa D \gtrsim 1$, where κL_{eff} sharply drops and rises before reaching the hard-core limit $L_{\mathrm{eff}} = L$. This is in fact a minor problem in practice, as it only occurs in the regime where $L_{\mathrm{eff}}/D_{\mathrm{eff}} \lesssim 0.1$. There, the anisotropic contribution to the effective excluded volume is much smaller than the isotropic part. Upon approach of the limit $\kappa L \gg 1$, see Fig. 2.4(b), we find that L_{eff} approaches L for all values of κD, as expected.

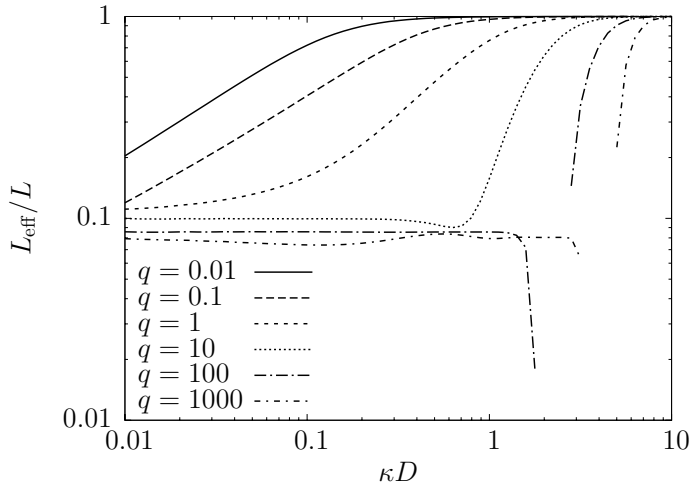

(a)

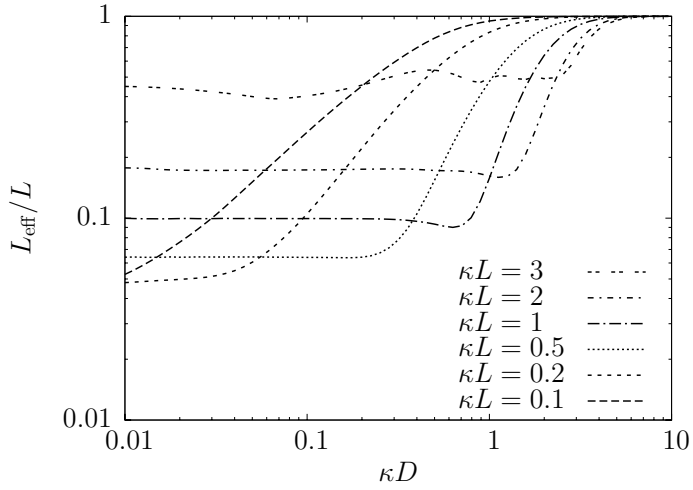

(b)

Figure 2.4: The effective length L_{eff}/L as a function of the rod diameter κD for (a) $\kappa L = 1$ and different values for the charge parameter q; (b) $q = 10$ and different values for the rod length κL. The rod diameter is scaled by the screening length κ^{-1} and the effective length is scaled by the rod length L.

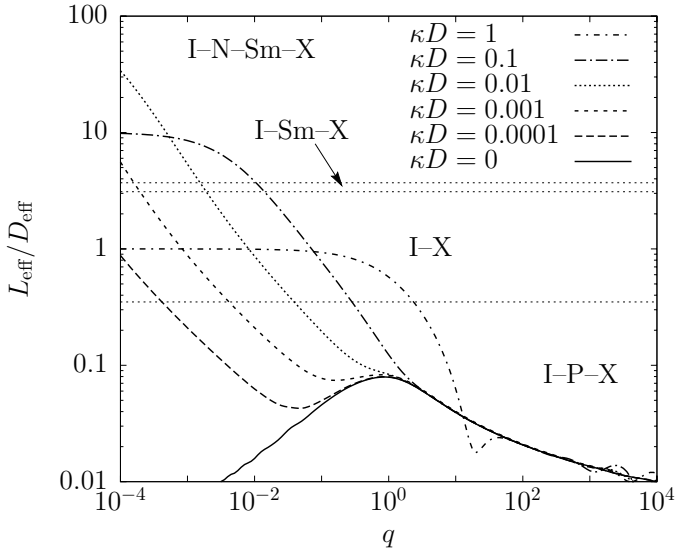

Figure 2.5: The effective aspect ratio $L_{\rm eff}/D_{\rm eff}$ as a function of the charge parameter q for $\kappa L = 1$ and different values for the rod diameter κD. Different—possibly coexisting—phases are associated with a certain range of (effective) aspect ratios. See the text for an explanation of the abbreviations and the boundary values.

2.5 Phase behavior

We have determined the effective length and diameter of charged rods, by mapping their orientation-dependent second virial coefficient onto that of hard rods of effective dimensions. Subsequently, we also study the effective length-to-diameter ratio $L_{\rm eff}/D_{\rm eff}$. In Fig. 2.5 we show this effective aspect ratio as a function of the rod charge for $\kappa L = 1$ and a range of rod diameters κD. All curves with $\kappa D > 0$ essentially decrease from their maximum value—the hard-core aspect ratio L/D—towards the curve obtained for $\kappa D = 0$. This indicates that the effective dimensions of charged rods become independent of the hard-core diameter for large charge parameters, where we enter the electrostatic regime. Also, since the effective aspect ratio for $\kappa D = 0$ is a decreasing function for large q, we see that the charged rods essentially behave as charged spheres upon increasing the charge above a certain value.

Moreover, Fig. 2.5 reveals a local maximum for the effective aspect ratio as a function of rod charge for very small κD, in the regime where $q \simeq 1$. This effect can be understood by considering the electrostatic regime for small charge parameters

q. Note that this electrostatic regime does not extend toward $q = 0$, only to a finite value of q that depends on the value of κD. This includes $\kappa D = 0$, for which q can become arbitrarily small. Equation (2.11) shows that the effective aspect ratio is governed by the dimensionless anisotropy parameter Δ, which is defined in Eq. (2.12). In the electrostatic regime, this anisotropy can be shown—up to first order—to be proportional to q, because the linear approximation of the effective excluded volume is orientation independent [63]. Therefore, the difference between the isotropically averaged and parallel values is of second order in q, whereas the parallel value itself is of first order. The effective aspect ratio is of order $\sqrt{\Delta}$, and thus increases as $\sqrt{q}$. Conversely, for $q \gtrsim 1$ the effective length is more or less constant, and the effective aspect ratio decreases again due to the increase of the effective diameter.

The horizontal dotted lines in Fig. 2.5 indicate the crossover values (0.35, 3.5, and 3.7) between regimes for which we expect different phase sequences upon increasing the density. The values for these aspect ratios are taken from simulation results of hard-spherocylinder systems by Bolhuis and Frenkel [19]. These simulations consist of explicit free-energy calculations of coexisting phases, where the most dilute phase is always given by an isotropic fluid (*I*), and the most dense phase by a fully ordered crystal (*X*). Depending on the aspect ratio, different phases were found in between these two phases. For aspect ratios exceeding ~ 3.7 the phase sequence *I*–*N*–Sm–*X* was found upon increasing the density. Here, the *N* and Sm denote the nematic and smectic-*A* liquid crystalline phases, respectively. Somewhat shorter rods, with an aspect ratio in the narrow regime between ~ 3.5 and ~ 3.7, can still form a smectic-*A* but no longer a nematic phase, and hence have a phase sequence *I*–Sm–*X*. Even shorter hard rods, with an aspect ratio in between ~ 0.35 and ~ 3.5 cannot form a thermodynamically stable smectic-*A* phase, and thus crystallize directly into a fully ordered crystal from the isotropic fluid, yielding a phase sequence *I*–*X*. Very short hard rods, with an aspect ratio smaller than ~ 0.35, exhibit a plastic (*P*) crystal phase, such that the phase sequence is *I*–*P*–*X*. The plastic crystal phase is characterized by orientational disorder, but has translational order as in a crystal phase [19, 59]. This regime arises naturally in the case that κL is small. Then, such a crystal forms because of the essentially isotropic long-range repulsive interactions, but the competition with entropic effects prevents the rods from aligning.

We use the mapping of the charged-rod system onto the effective hard-rod system to give an indication of the phase sequence of systems of charged rods as a function of the parameters κL, κD (or L/D), and q. For instance, from the curve for $\kappa D = 1$ in Fig. 2.5, we see that the effective aspect ratio never exceeds unity for any q. This excludes the possibility of a nematic or smectic-*A* liquid crystal phase. The curve starts off at its maximum (in the limit where $q \to 0$), where the effective aspect ratio equals the hard-core aspect ratio $L/D = \kappa L = 1$. It crosses the value $L_{\text{eff}}/D_{\text{eff}} = 0.35$

at $q \approx 2.35$, such that a sufficiently large rod charge density allows for a plastic crystal phase. Similarly, for $\kappa D = 0.1$ (which corresponds to $L/D = 10$), we find all four phase sequences upon increasing q.

By determining the intersections of the effective aspect ratio with the crossover values of the hard-rod system, we construct "phase diagrams" indicating the different regimes. In Fig. 2.6 we present two examples of such diagrams in the plane spanned by q and κD. In Fig. 2.6(a), we fix $\kappa L = 1$, such that the horizontal axis could read D/L as well. In Fig. 2.6(b) we fix $L/D = 20$, such that the change in κD physically corresponds to a change in salt concentration (while keeping the particle dimensions fixed). The symbols denote the crossover values for the effective aspect ratio as determined from our numerical data (such as presented in Fig. 2.5). The lines are based on an approximate theoretical model to be discussed in Sec. 2.6.

Both diagrams in Fig. 2.6 show that rods with sufficiently high charge always show the *I*–*P*–*X* sequence. This is due to the essentially spherical nature of the effective shape of highly charged rods. The limit of uncharged rods is determined by the hard-core sequence that corresponds to L/D. The *I*–*N*–Sm–*X* regime at fixed κL in Fig. 2.6(a) is completely bounded. First, by a hard-core regime when $\kappa D \gtrsim 0.27$, where the liquid crystal phases cannot exist even for $q = 0$ because $L/D \lesssim 3.7$. Second, by an electrostatic regime in the weak-screening limit of small κD, where the rods effectively behave as spheres since $D_{\text{eff}} \gg L_{\text{eff}}$. Conversely, the trends displayed for fixed L/D in Fig. 2.6(b) are monotonic, with an *I*–*N*–Sm–*X* regime that extends to higher q with increasing κD.

2.6 A Simpler Model

For small values of the rod charge, we found that the electrostatic contribution to the effective excluded volume (2.4) is essentially isotropic in nature, which implies that the anisotropic effects are primarily due to the hard-core anisotropy. This is also apparent from Fig. 2.1, where the angle dependent contribution has a constant shape upon increasing the charge, whereas the isotropic contribution increases. We therefore propose that—by approximation—the anisotropic parts of the hard-core and effective excluded volumes are equal, such that

$$L_{\text{eff}}^2 D_{\text{eff}} \simeq L^2 D. \tag{2.18}$$

On this basis, we propose here a simple model, which turns out to describe our numerical findings with remarkable accuracy. This model introduces a "spherical approximation" of the electrostatic contribution to the effective excluded volume, which involves the orientation-dependent diameter $\bar{D}(\gamma)$. The volume of a sphere of this

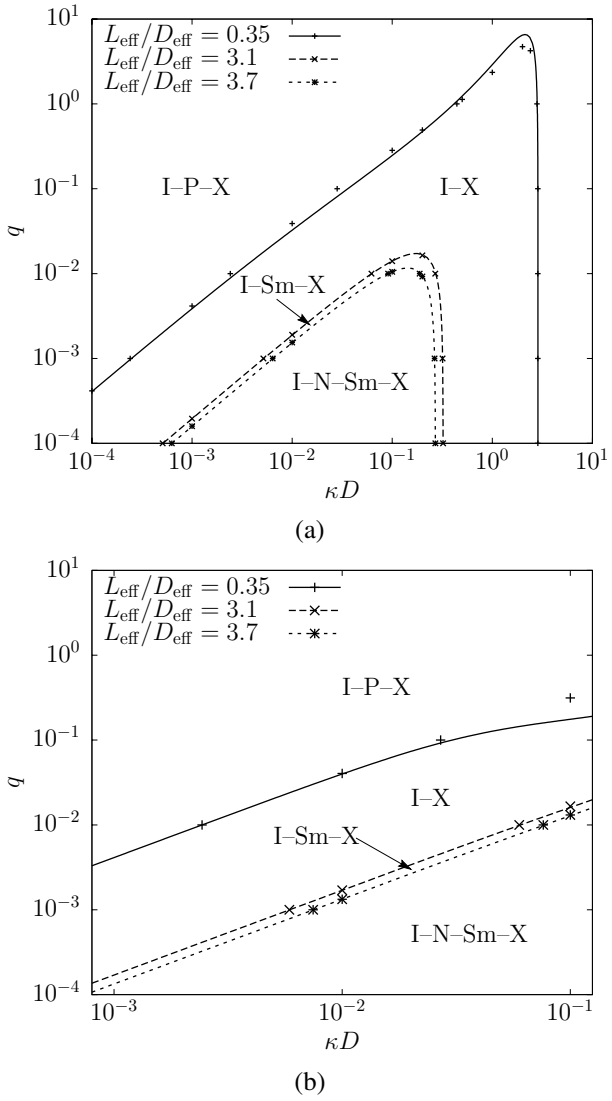

Figure 2.6: Boundary lines for given values for the effective aspect ratio $L_{\rm eff}/D_{\rm eff}$. See the text for an explanation of the abbreviations of the different regime labels. The points are results of numerical calculations, and the lines are given by a simplified theory. We fix (a) $\kappa L = 1$, and (b) $L/D = 20$, respectively.

diameter is equal to the hard-core excluded volume of a pair of rods [20]

$$\frac{4\pi}{3}\bar{D}(\gamma)^3 = \frac{4\pi}{3}D^3 + 2\pi LD^2 + 2L^2D\sin\gamma. \tag{2.19}$$

We approximate the effective excluded volume (2.4) by the value for charged spheres of diameter $\bar{D}(\gamma)$, and effective (point) charge that equals the total amount of effective charge on the rods,

$$\bar{E}(\gamma) = \frac{4\pi}{3}\bar{D}(\gamma)^3 + 4\pi\int_{\bar{D}(\gamma)}^{\infty} \mathrm{d}r\, r^2 \left(1 - \exp\left[-q\kappa^2 L^2 \frac{\exp[-\kappa r]}{\kappa r}\right]\right). \tag{2.20}$$

Note that the only orientation dependence of the electrostatic contribution to this effective excluded volume (i.e., the second term) comes from the integration boundary $\bar{D}(\gamma)$. To calculate the effective dimensions, we only need the parallel and isotropically averaged values of the effective excluded volume. In the parallel case ($\gamma = 0$) this value is readily calculated

$$\bar{E}_{\parallel} = \frac{4\pi}{3}\bar{D}_{\parallel}^3 + 4\pi\int_{\bar{D}_{\parallel}}^{\infty} \mathrm{d}r\, r^2 \left(1 - \exp\left[-q\kappa^2 L^2 \frac{\exp[-\kappa r]}{\kappa r}\right]\right), \tag{2.21}$$

where

$$\frac{4\pi}{3}\bar{D}_{\parallel}^3 = \frac{4\pi}{3}D^3 + 2\pi LD^2. \tag{2.22}$$

The isotropically averaged value can be calculated numerically by using expression (2.20). However, we approximate it by the value for a charged sphere of diameter $\bar{D}_{\mathrm{iso}}$ (using the same total effective charge), which is taken from the isotropic average of the hard-core excluded volume

$$\frac{4\pi}{3}\bar{D}_{\mathrm{iso}}^3 = \frac{4\pi}{3}D^3 + 2\pi LD^2 + \frac{\pi}{2}L^2D. \tag{2.23}$$

This approximation yields the simple expression

$$\bar{E}_{\mathrm{iso}} = \frac{4\pi}{3}\bar{D}_{\mathrm{iso}}^3 + 4\pi\int_{\bar{D}_{\mathrm{iso}}}^{\infty} \mathrm{d}r\, r^2 \left(1 - \exp\left[-q\kappa^2 L^2 \frac{\exp[-\kappa r]}{\kappa r}\right]\right). \tag{2.24}$$

With our explicit expressions (2.21) and (2.24), we evaluate the effective dimensions from Eqs. (2.10) and (2.11) as before. The resulting crossover values of the hard-rod system are shown by the curves in Fig. 2.6, and are in very good agreement with the numerical calculations presented in Sec. 2.5 (denoted by the symbols). The key to this remarkable accuracy lies in the fact that the anisotropic electrostatic contributions are relatively unimportant, because the rod length is small with respect to the screening length (i.e., $\kappa L \leq 2$). Thus, our simple model accounts for the hard-core anisotropy correctly, as well as for the isotropic electrostatic contribution.

Interestingly, for small κL the lowest-order contribution to V_e in Eq. (2.2) is quadratic in κL and independent of rod orientations. Also, it happens to correspond to the interaction potential of two point charges $e\lambda L$. If we insert this approximation of $V(\mathbf{r};\hat{\omega},\hat{\omega}')$ into the expression of the effective excluded volume [given by Eq. (2.4)], we obtain an expression where the integral boundary $\bar{D}$ is still a function of both the angle between the rod orientations and the direction of the center-to-center separation vector $\mathbf{r}$. In fact, it is given by the distance where the rods touch, given a certain orientational configuration. By setting this overlap diameter to a value that is independent of the orientation of $\mathbf{r}$, but still respects the total hard-core excluded volume, we effectively neglect its dependence on κL. This choice is justified by the fact that (for small κL) the size of the double layer around the particles is larger than the variations in the overlap diameter $\bar{D}$. That is why our simple theoretical description can be interpreted—in a sense—as a perturbation theory of a hard-rod reference system with an (almost) isotropic electrostatic contribution. Unfortunately, it completely fails to describe the anisotropic effects in the electrostatic regime. In this regime the anisotropic details of the electrostatic contributions do become important compared to the hard-core contributions.

2.7 Discussion and Conclusion

The numerical results presented in this chapter give access to a part of the parameter space where there is a large difference between the effective length and the real length. In this regime, one cannot hope that the theory of Stroobants et al. [58] gives any accurate results, as this is based on the needle limit where $L_{\text{eff}} \simeq L$. The perturbation theory of Chen and Koch [63] breaks down for most of our parameter values. This is because it is based on small charges, and thus fails to describe the effect of large rod surface-charge densities. Also, this theory is not accurate for large differences between the effective and hard-core diameter.

In Fig. 2.7(a), we show results of numerical calculations of the effective rod length as a function of the hard-core length, for $\kappa D = 0.1$. Note that again the effective length is always smaller than (or equal to) the hard-core length. Also, in accordance with the results from Fig. 2.4, there is a hard-core regime for small values of the charge parameter q, as well as for small values of the rod length κL, for which the total amount of effective rod charge is small. On the other hand, there is an electrostatic regime. In Fig. 2.4, this was shown to be the case for decreasing values of κD, where the plateau value (i.e., the electrostatic length) depends on q and κL. However, from Fig. 2.7(a), it can be seen that this electrostatic length depends mostly on the rod length κL, and not really on the charge parameter q, as long as either q or κL is large enough.

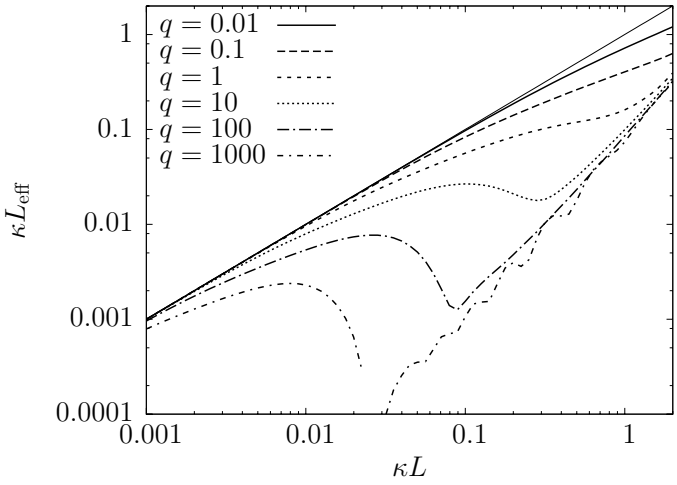

(a)

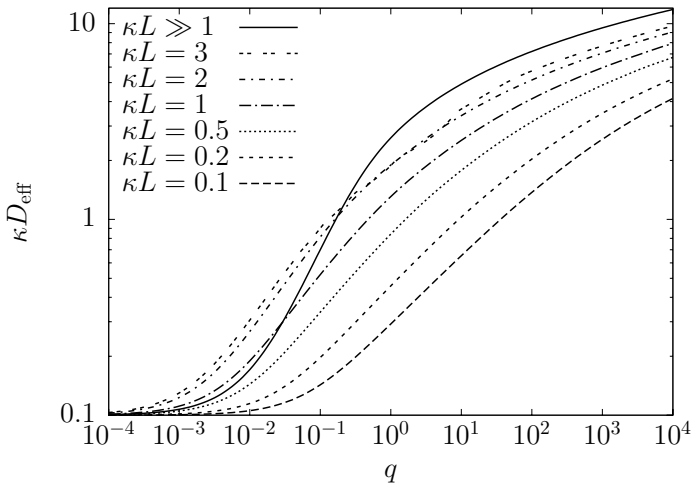

(b)

Figure 2.7: (a) The effective length $\kappa L_{\rm eff}$ as a function of the rod length κL for $\kappa D = 0.1$ and different values for the charge parameter q. The thin solid line represents the needle or hard-core limit, where $L_{\rm eff} \simeq L$. (b) The effective diameter $\kappa D_{\rm eff}$ as a function of the rod charge parameter q for $\kappa D = 0.1$ and different values for the rod length κL. The (effective) rod dimensions are scaled by the screening length κ^{-1}.

Furthermore, the effective length is "wedged" in between the electrostatic length and the hard-core length, where the electrostatic length approaches the hard-core length in the needle limit ($\kappa L \gg 1$).

Unfortunately, there is no analytic theory yet that describes our numerical results for this electrostatic length as a function of κL. Therefore, it would be worthwhile to gain new insight in the effect of electrostatics on the effective rod length for intermediate κL—neglecting hard-core interactions—in the case of large rod charges. In this regime, however, the angular dependence of the effective excluded volume is different from that of a hard spherocylinder. Visual inspection of Fig. 2.2 reveals this difference for small angles. Probably, the effective shape resembles more a hard ellipsoid of revolution, for which it is know that there is no stable smectic phase [69]. Thus, one can claim that the existence of a stable smectic phase is questionable in this regime. On the other hand, in the parameter regime that we focused on in this chapter this subtlety is not directly relevant. The part of the diagram of phase sequences that shows a smectic phase is well described by the simplified model in which the anisotropy of the effective excluded volume purely stems from the hard-core interactions. In this case, the increase of q leads to such a strong increase in the isotropic contribution to the effective excluded volume that the smectic phase disappears from the sequence. This happens before the onset of any significant change in the effective shape.

Another point of discussion is the validity of our treatment of the rod charge as a homogeneous effective line charge. In the case of homogeneously charged spheres in linearized Poisson-Boltzmann theory, the pair interaction is often approximated as that between two effective point charges. This approximation is proven to be accurate for large interparticle distances [40]. It involves the scaling of the actual charge with a factor that depends solely on the ratio between the particle diameter and the screening length. This scaling yields the exact solution for the single particle potential, where the solution is replaced with the potential generated by a single point charge of the scaled amplitude. In the case of an homogeneously charged infinite cylinder, a similar scheme can be applied by replacing the charged cylinder with an effective line charge. Although the scaling factor is different, it still only depends on the ratio κD between the rod diameter and the screening length, and it has the same order of magnitude up to $\kappa D \simeq 10$. The present case of a homogeneously charged *finite-sized* spherocylinder poses a problem, because we have no analytic solutions of the single-particle potentials for both a line charge or a surface charge. Moreover, we have no proof that the pair interaction of the surface-charge case can be reliably approximated by a pair interaction involving line charges.

Finally, Fig. 2.7(b) shows results of numerical calculations of the effective diameter as a function of the charge parameter q. For $q \gtrsim 1$, there is a smooth transition to the theoretical needle limit of Ref. [58], where $\kappa L \gg 1$. Conversely, this is not the

case for $q \lesssim 1$, probably due to the fact that the approximations leading to Eq. (2.15) do not give the correct effective excluded volume for small values of q and (nearly) parallel rods. More investigations need to be made into this regime.

In conclusion, we have numerically studied the second virial coefficient of short charged rods dispersed in an electrolyte, presuming pairwise screened-Coulomb interactions between the line-charge segments of the rods. The control parameters of interest are the hard-core length L and diameter D, the Debye screening length of the medium κ^{-1}, and the charge parameter q. The main resulting quantities are the effective diameter D_{eff} and length L_{eff} of the rods. By a mapping onto an effective hard-core system—for which the sequence of phases between the dilute isotropic phase and the dense crystalline phase is known for all aspect ratios—we predict the relations between control parameters and the expected phase sequence explicitly. We have also constructed a simplified model, based on the diameter $\bar{D}(\gamma)$ of Eq. (2.19), which reproduces the numerical results accurately at the expense of much less computational effort. This model is particularly successful in the regime of large effective aspect ratios ($L_{\text{eff}}/D_{\text{eff}} > 1$) and small ratios of the rod length to the screening length ($\kappa L < 1$).

An important result of this work is that highly charged short rods at low salt concentrations (i.e., at strong Coulomb couplings) have a strong tendency to form plastic crystals upon compression. The plasticity stems from the large effective diameter, which make the rods behave essentially as inflated repulsive spheres with only small nonspherical interactions that are too weak to cause orientational ordering in the crystalline phase. This finding could be important in the study of silica or gold nanorods, that have reasonably large hard-core aspect ratio (such as $L/D \simeq 5$). Here, liquid crystalline phases could be expected, but only if the charge on the rods is small enough.

Acknowledgement

We thank Marjolein Dijkstra for performing the Monte Carlo calculations presented in Sec. 2.4 and depicted in Fig. 2.2.

The work presented in this chapter is also published in the article:
"Effective shape and phase behavior of short charged rods"
Phys. Rev. E, 79:041401, 2009.

Chapter 3

Charge renormalization of Janus particles

Abstract

Nonlinear ionic screening theory for heterogeneously charged spheres is developed in terms of a mode-decomposition of the surface charge. A far-field analysis of the resulting electrostatic potential leads to a natural generalization of charge renormalization from purely monopolar to dipolar, quadrupolar, etc., including 'mode-couplings'. Our scheme is generally applicable to large classes of surface heterogeneities, and is explicitly applied here to Janus spheres with differently charged upper and lower hemispheres, revealing strong renormalization effects for all multipoles.

3.1 Introduction

The past few years have seen an explosion of newly synthesized colloidal (nano)particles that are *not* spherically symmetric, either by shape (e.g. dumbbells, snowmen, cubes) or by surface pattern (patches, stripes) [1]. A broken rotational symmetry also occurs when particles are adsorbed to air–water or oil–water interfaces [70], as in for example, colloidal monolayers [71, 72], Pickering emulsions [73], or bijels [74, 75]. Moreover, recent atomic force microscopy studies have shown that even supposedly homogeneous colloidal surfaces can actually be heterogeneous on length scales as

large as 100 nm [26, 27], while atomic corrugations and facets render any nm-sized particle strictly heterogeneous. An important consequence of surface heterogeneity is anisotropy of the mutual effective forces, which directly affects the self-assembly process of the (nano)colloids into large-scale structures, for instance into linear chains [26, 27, 72, 76, 77].

An important problem is thus to establish relationships between shape and surface heterogeneity on the one hand and effective interactions and large-scale self-assembly structures on the other [1]. Apart from specific forces (e.g., hydrophobic, van der Waals) the effective interactions between dispersed particles often involve a strong generic electrostatic component, which is well described, for homogeneously charged objects, by linear-screening theory provided renormalized charges instead of bare charges are used [78–82]. Renormalization of heterogeneously distributed surface charge is an open problem, for which we develop a systematic theory in this chapter. We go beyond recent linear screening treatments [52, 83–87] and formulate a new and efficient framework for computing *nonlinear* ionic screening effects of heterogeneously charged spheres dispersed in a 1:1 electrolyte. Our theory generalizes Alexander's notion of ion-condensation induced charge renormalization [78–82] to include not only the monopole but also the dipole, quadrupole, etc., as well as their nonlinear couplings. These multipole modes can be important if one wishes to calculate the electrostatic force between particles, as was shown already for clay platelets [88]. Our scheme is versatile and can be applied to essentially any type of charge heterogeneity. We focus on applications to Janus spheres composed of two differently charged hemispheres [11, 12].

3.2 Charge renormalization

In this section, we present the concept of charge renormalization. It is based on the correspondence between linear and nonlinear Poisson-Boltzmann theory, developed by Alexander et al. [78], and subsequently extended by Trizac et al. [80]. The nonlinear Poisson-Boltzmann (PB) equation introduced in Sec. 1.3 is notoriously difficult to solve in a general geometry. In contrast, the linearized Poisson-Boltzmann (LPB) theory introduced in Sec. 1.4 is relatively tractable. It also has the upshot of being a convenient description for a dilute many-body system of colloidal particles, by simply adding pair interactions of all pairs of particles. The downside of this linearization is of course that it fails to accurately describe the effects of large differences in the electrostatic potential. Therefore, the linearized description of a highly charged colloidal particle gets worse as the charge increases. In order to give an idea of the nonlinear-screening properties of highly charged colloidal systems, Alexander et al.

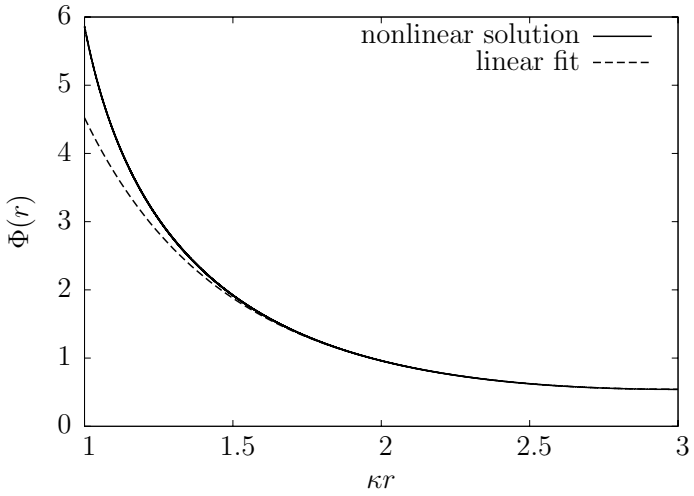

Figure 3.1: Nonlinear and linear solution to the Poisson-Boltzmann equation, with equal values for $\Phi(R)$ and $\Phi'(R) = 0$, for $\kappa a = 1$, $\kappa R = 3$, $\kappa l_B = 0.01$, and $Z = 2250$.

[78] developed an effective description that goes by the name of *charge renormalization*. It estimates the long-range behavior of a charged colloid by fitting a linear solution to the numerical solution of the nonlinear theory. To this end, a simple geometry is chosen to solve the nonlinear problem. This geometry is a spherical cell, referred to as a Wigner-Seitz cell [89].

Following the description of Trizac et al. [80], we consider a spherical colloidal particle of radius a, and total surface charge Ze, in the center of a spherical cell of radius R. The nonlinear PB equation (1.6) can be solved straightforwardly by numerical integration for the boundary conditions

$$\Phi'(a) = -\frac{Zl_B}{a^2}, \tag{3.1}$$

$$\Phi'(R) = 0, \tag{3.2}$$

where l_B is the Bjerrum length. The first condition imposes a discontinuity in the electric field at the particle surface that corresponds with the surface charge density $\sigma = Ze/4\pi a^2$. The second condition imposes charge neutrality of the cell. An example of a solution is given in Fig. 3.1, for $\kappa a = 1$, $\kappa R = 3$, $\kappa l_B = 0.01$, and $Z = 2250$. The numerical calculation yields a numerical value for the boundary value $\Phi(R) \equiv \Phi_R$. We can use this value to linearize the PB equation in the cell with respect to deviations

from that potential,

$$\Phi''(r)+\frac{\Phi'(r)}{r}=\kappa^2\sinh\Phi_R+\kappa^2\cosh\Phi_R(\Phi(r)-\Phi_R)\qquad\text{for } a<r<R. \tag{3.3}$$

This yields a different kind of LPB equation compared to Eq. (1.15), where we linearized with respect to $\Phi=0$. We solve Eq. (3.3) analytically, for the boundary conditions

$$\Phi(R)=\Phi_R, \tag{3.4}$$

$$\Phi'(R)=0. \tag{3.5}$$

This yields the solution

$$\Phi(r)=\Phi_R+\tanh\Phi_R\left(\frac{(\bar\kappa R+1)\exp[\bar\kappa(r-R)]}{2\bar\kappa r}+\frac{(\bar\kappa R-1)\exp[-\bar\kappa(r-R)]}{2\bar\kappa r}-1\right), \tag{3.6}$$

where $\bar\kappa^2=\kappa^2\cosh\Phi_R$. We give an example for this solution in Fig. 3.1, for $\kappa a=1$, $\kappa R=3$, $\kappa l_\mathrm{B}=0.01$, and $Z=2250$, where it is evident that the linear solution (3.6) correctly fits the behavior of the nonlinear solution in the vicinity of the cell surface. When we evaluate the derivative of the linear solution (3.6) at the particle surface $\Phi'(a)$, we obtain the *renormalized* charge Z^* by setting $\Phi'(a)=-Z^*l_\mathrm{B}/a^2$. The result is plotted in Fig. 3.2 for $\kappa a=1$, $\kappa R=3$, $\kappa l_\mathrm{B}=0.01$, and different values of Z. Note that $Z^*\simeq Z$ for small Z, and that a charge saturation effect occurs for high Z. There, the renormalized charge Z^* becomes constant, and is not effected by increasing the actual charge. In the following sections, we generalize this scheme for heterogeneous charge distributions.

3.3 Model

We consider an index-matched suspension of N colloidal spheres of radius a in a bulk solvent of permittivity ε and volume V at temperature T. The solvent also contains point-like monovalent cations (charge $+e$) and anions (charge $-e$), which are provided by bringing the system in contact with a salt reservoir at fugacity ρ_s. Here e is the elementary charge. A relatively simple treatment of this many-body problem is provided by the cell model [78–82], in which a single colloid is considered in the center of a spherical cell of radius R and volume $(4\pi/3)R^3=V/N$. This model is introduced in Sec. 3.2. We denote the surface charge density of this central colloidal particle by $e\sigma(\theta,\varphi)$, where θ and φ are the standard spherical meridional and azimuthal angle, respectively, with respect to a laboratory frame. Within a mean-field approximation, the concentration profiles of the cations and anions in the solvent can

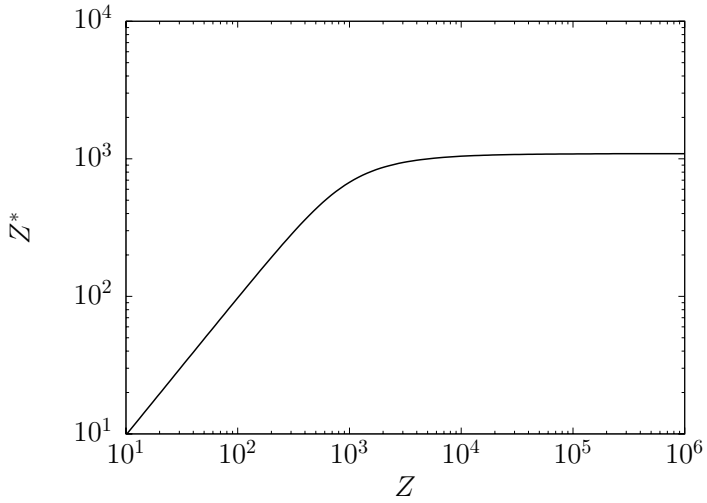

Figure 3.2: Renormalized charge as a function of actual charge for $\kappa a = 1$, $\kappa R = 3$, and $\kappa l_B = 0.01$.

be written as Boltzmann distributions $\rho_\pm(\mathbf{r}) = \rho_s \exp[\mp\Phi(\mathbf{r})]$, where $k_B T\Phi(\mathbf{r})/e$ is the electrostatic potential at position $\mathbf{r} = (r\sin\theta\cos\varphi, r\sin\theta\sin\varphi, \cos\theta)$, with k_B the Boltzmann constant and $r = |\mathbf{r}|$. Note that $\Phi(\mathbf{r}) = 0$ in the salt reservoir, and that $\rho_\pm(\mathbf{r}) = 0$ for $r < a$ due to hard-core exclusion. The potential must satisfy the Poisson equation $\nabla^2\Phi(\mathbf{r}) = -4\pi l_B(\rho_+(\mathbf{r}) - \rho_-(\mathbf{r}))$, where we defined the Bjerrum length $l_B = e^2/4\pi\varepsilon k_B T$. Combining the Poisson and Boltzmann equations gives

$$\Phi''(\mathbf{r}) + \frac{2\Phi'(\mathbf{r})}{r} - \frac{\mathscr{L}^2\Phi(\mathbf{r})}{r^2} = \begin{cases} 0 & r < a, \\ \kappa^2 \sinh\Phi(\mathbf{r}) & r > a, \end{cases} \tag{3.7}$$

where a prime denotes a radial derivative,

$$\mathscr{L}^2 \equiv -\left[\partial_\theta^2 + \frac{\partial_\theta}{\tan\theta} + \frac{\partial_\varphi^2}{\sin^2\theta}\right], \tag{3.8}$$

and $\kappa^{-1} = \sqrt{1/8\pi l_B \rho_s}$ is the screening length. On the colloidal surface, $r = a$, Gauss' law imposes the boundary condition (BC)

$$\lim_{r\downarrow a}\Phi'(r,\theta,\varphi) = \lim_{r\uparrow a}\Phi'(r,\theta,\varphi) - 4\pi l_B\sigma(\theta,\varphi). \tag{3.9}$$

Electroneutrality of the cell imposes $\int \mathrm{d}\varphi\mathrm{d}\theta\sin\theta\,\Phi'(R,\theta,\varphi) = 0$ at $r = R$, which is a sufficiently stringent BC to close the system of equations in the spherically symmetric

case. Now, however, an additional BC is to be specified for the angular dependence at $r = R$, depending on the environment of the cell. For now, we assume an environment that is characterized via 'isotropic' boundary conditions,

$$\partial_\theta \Phi(R,\theta,\varphi) = \partial_\varphi \Phi(R,\theta,\varphi) = 0. \tag{3.10}$$

Thus the electrostatic potential at the cell boundary is a constant, which is not necessarily zero. We will discuss this choice, and its consequences, in Sec. 3.6.

3.4 Theory

For a given $\sigma(\theta,\varphi)$ one can solve (3.7) with BCs for $\Phi(\mathbf{r})$, for example, numerically on a discrete (r,θ,φ) grid. The approach we take, however, avoids a cumbersome 3-dimensional grid in favor of a systematic expansion of the angular dependence in spherical harmonics. For notational convenience and illustration purposes we restrict attention here to φ-independent cases where the expansion involves only Legendre polynomials $P_\ell(x)$ with $x = \cos\theta$.

The first step in this analysis is the decomposition of the colloidal surface charge into surface multipoles $\sigma_\ell = \frac{2\ell+1}{2}\int_{-1}^{+1} \mathrm{d}x \sigma(x) P_\ell(x)$, such that

$$\sigma(x) = \sum_{\ell=0}^{\infty} \sigma_\ell P_\ell(x). \tag{3.11}$$

Similarly we decompose

$$\Phi(r,x) = \sum_{\ell=0}^{\infty} \Phi_\ell(r) P_\ell(x). \tag{3.12}$$

For $r < a$, the electrostatic potential assumes the regular form $\Phi_\ell(r) = (r/a)^\ell \Phi_\ell(a)$, in the absence of charge inside the colloidal particle. Therefore, the BCs for the solution to Eq. (3.7) for $r > a$ are given by

$$\Phi'_\ell(a) = \frac{\ell}{a}\Phi_\ell(a) - 4\pi l_\mathrm{B}\sigma_\ell \qquad \text{for } \ell \geq 0, \tag{3.13}$$

$$\Phi'_0(R) = 0, \qquad \text{and} \quad \Phi_\ell(R) = 0 \quad \text{for } \ell \geq 1, \tag{3.14}$$

where the derivative on the colloidal surface is taken *outside* the particle. These BCs conveniently decouple for the different ℓs. By contrast, the nonlinear sinh term in (3.7) induces 'mode-coupling' between *all* Legendre components $\Phi_\ell(r)$—not to be confused with mode-couplings in dynamical slowing down. This coupling is obviously unpractical for a numerical treatment.

The second step of our analysis resolves this mode-coupling problem by 'ordering' the modes systematically. We introduce a dimensionless 'switching' parameter A, and consider the auxiliary charge distribution $\sigma^{(A)}(x) = \sum_{\ell=0}^{\infty} A^\ell \sigma_\ell P_\ell(x)$, such that $A = 0$ describes a homogeneous charge distribution and $A = 1$ the heterogeneous one of interest. We also define the corresponding auxiliary potential $\Phi^{(A,L)}(r,x) = \sum_{n=0}^{L} A^n \phi_n(r,x)$, where L sets the order of the truncation and where the expansion coefficients can themselves be expanded as $\phi_n(r,x) = \sum_{\ell=0}^{n} f_{n,\ell}(r) P_\ell(x)$. This potential is defined as the truncated solution of Eq. (3.7) with BCs (3.13) and (3.14) in which the charge distribution $\sigma(x)$ is replaced with the auxiliary charge distribution $\sigma^{(A)}(x)$. The functions $f_{n,\ell}(r)$ are independent of A and will be calculated numerically below for the cases of interest $n \geq \ell$ (which is assumed implicitly from now on). Since $\sigma^{(A)}(x)$ is invariant under the simultaneous transformation $A \to -A$ and $x \to -x$ one checks that $f_{n,\ell}(r) = 0$ for $n + \ell$ odd, that is, we only consider ℓ and n both even or both odd.

Replacing $\sigma(x)$ by $\sigma^{(A)}(x)$ and $\Phi(r,x)$ by $\Phi^{(A)}(r,x)$, inserting the corresponding expansions into the BC's, and equating all orders of A yields at $r \downarrow a$ and $r = R$

$$f'_{n,\ell}(a) = \frac{\ell}{a} f_{n,\ell}(a) - 4\pi l_B \sigma_\ell \delta_{n,\ell}, \tag{3.15}$$

$$f'_{n,0}(R) = 0, \qquad \text{and} \quad f_{n,\ell}(R) = 0 \quad \text{for } \ell \geq 1, \tag{3.16}$$

where $\delta_{n,\ell}$ is the Kronecker delta. When the same replacement and expansion procedure is applied to the PB equation (3.7), one finds upon expanding the argument of the sinh term with respect to A a hierarchy of second-order differential equations for $f_{n,\ell}(r)$, with a structure that allows for an order-by-order sequential solution. For $n = \ell = 0$ we obtain for $r \in [a,R]$ the spherically symmetric nonlinear PB equation in the cell, $f''_{0,0}(r) + \frac{2}{r} f'_{0,0}(r) = \kappa^2 \sinh f_{0,0}(r)$, which we solve numerically with the BCs given in (3.15) and (3.16) on a radial grid. We thus consider $f_{0,0}(r)$ as a known function from now on. For $n \geq 1$ we obtain

$$f''_{n,\ell}(r) + \frac{2}{r} f'_{n\ell}(r) - \Big(\frac{\ell(\ell+1)}{r^2} + \kappa^2 \cosh f_{0,0}(r) \Big) f_{n,\ell}(r) = \kappa^2 S_{n,\ell}(r), \tag{3.17}$$

where $S_{n,\ell}(r)$ acts as a source term of the form $S_{1,1} = 0$, $S_{2,0} = \frac{1}{6} f_{1,1}^2 \sinh f_{0,0}$, $S_{2,2} = 2S_{2,0}$, $S_{3,1} = f_{1,1}(f_{2,0} + \frac{2}{5} f_{2,2}) \sinh f_{0,0} + \frac{1}{10} f_{1,1}^3 \cosh f_{0,0}$, $S_{3,3} = \frac{3}{5} f_{1,1} f_{2,2} \sinh f_{0,0} + \frac{1}{15} f_{1,1}^3 \cosh f_{0,0}$. Explicit expressions for higher-order terms can be generated straightforwardly. The key observation is that $S_{n,\ell}$ only depends on $f_{n',\ell'}$s with $n' < n$, that is, a hierarchy of terms follows spontaneously. Thus (3.17) with the BCs (3.15) and (3.16) can be solved for $n = \ell = 1$, which in turn determines $S_{2,0}(r)$ and $S_{2,2}(r)$ such that $f_{2,0}(r)$ and $f_{2,2}(r)$ can be solved, etc. The nonlinear mode-coupling, represented explicitly by $\cosh f_{0,0}(r)$ and $S_{n,\ell}(r)$, renders the linear equation (3.17) highly nontrivial,

yet numerical solution on a radial grid $r \in [a,R]$ is straightforward. With $f_{n,\ell}(r)$ determined for $L \geq n \geq \ell \geq 0$ for some cut-off L, we can set $A = 1$ to explicitly construct the potential of interest $\Phi(r,x) = \sum_{\ell=0}^{L} \Phi_\ell(r) P_\ell(x)$ with $\Phi_\ell(r) = \sum_{n=\ell}^{L} f_{n,\ell}(r)$.

3.5 Results

The theory developed so far is directly applicable to any uniaxial charge distribution, while generalizations to azimuthal dependencies and nonspherical shapes are feasible. In this chapter we illustrate our scheme for the prototype heterogeneous charge distribution of Janus spheres characterized by surface charge densities σ_N and σ_S on the northern $(x > 0)$ and southern $(x < 0)$ hemisphere, respectively [11, 12, 28]. The nonvanishing modes are thus $\sigma_0 = (\sigma_N + \sigma_S)/2$ and $\sigma_\ell = g\sigma_0(2\ell+1)(-1)^{(\ell-1)/2}\frac{(\ell-2)!!}{(\ell+1)!!}$ for ℓ odd. Here we defined the dimensionless heterogeneity parameter

$$g = \frac{\sigma_N - \sigma_S}{\sigma_N + \sigma_S}, \tag{3.18}$$

which together with the total charge $Z_0 = 4\pi a^2 \sigma_0$ fully characterizes the distribution. Below we set $\kappa a = 1$, $R/a = 3$, and $L = 13$ throughout unless stated otherwise, and we identify $Z_0 l_B/a$ as the only other relevant dimensionless combination. For $Z_0 l_B/a = 22.5$ and $g \in \{0, 0.5, 0.8\}$, Fig. 3.3(a) shows the θ-dependence of σ (inset) and Φ for several r, revealing isotropy (as expected) for a homogeneous surface charge ($g = 0$, arrows) and strong anisotropy for the heterogeneous cases $g = 0.5$ ($\sigma_N = 3\sigma_S$, dot-dashed) and $g = 0.8$ ($\sigma_N = 9\sigma_S$, solid lines); the (small) oscillations with θ at $r = a$ are numerical artifacts due to the truncation at $L = 13$. The θ-dependence of the potential weakens, as expected, for increasing distances r. Figure 3.3(b) shows $\Phi_\ell(r)$ for $\ell = 0, 1, 2$ and $g = 0.5$. Interestingly, the modes with $\ell = 1, 2$ have a nonvanishing electric field in the interior of the particle. The overall magnitude and spatial variation of Φ in Fig. 3.3 show the need for nonlinear screening theory. Nevertheless, in analogy to the spherically symmetric case [78–82] one can describe the far-field potential ($r \simeq R$) and hence the colloidal interactions in terms of *linear* screening theory (dashed curves in Fig. 3.3(b)) with the renormalized surface charge distribution $\sigma^*(x) = \sum_\ell \sigma_\ell^* P_\ell(x)$ that we will calculate below.

In the far field ($r \simeq R$), we treat the deviation of $\Phi(r,x)$ from its angular average $\Phi_0(R) \equiv \chi_0$ at $r = R$ as a small expansion parameter, such that (3.7) for $r > a$ can be linearized as:

$$\nabla^2 \Phi(r,x) \simeq \bar{\kappa}^2 [\tanh \chi_0 + (\Phi(r,x) - \chi_0)], \tag{3.19}$$

with $\bar{\kappa}^2 = \kappa^2 \cosh \chi_0$. The uniaxial solutions to this linear Poisson-Boltzmann (LPB)

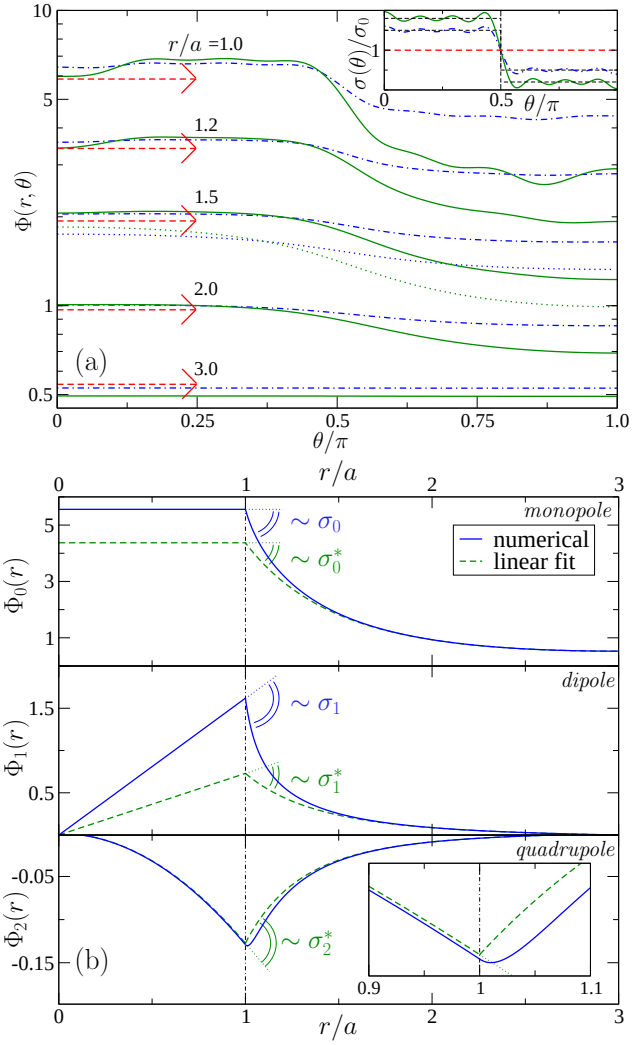

Figure 3.3: (a) Angular dependence of the potential (at several distances r) and the surface charge (inset) of a Janus sphere, for $\kappa a = 1$, $Z_0 l_B/a = 22.5$, $R/a = 3$, and $L = 13$, for charge heterogeneities (see text) $g = 0$ (arrows), $g = 0.5$ (dot-dashed), and $g = 0.8$ (solid curves). Dotted curves for $r/a = 1.5$ and $g \in \{0.5, 0.8\}$ stem from a Yukawa-segment model (see text). (b) Radial dependence of the monopole ($\ell = 0$), dipole ($\ell = 1$), and quadrupole ($\ell = 2$) potentials $\Phi_\ell(r)$ (solid lines), and their far-field linear-screening approximations (dashed curves), for $g = 0.5$. Angles defined at $r = a$ relate to the bare and renormalized modes of the surface charge (see text).

equation read

$$\Phi(r,x) \simeq \chi_0 - \tanh\chi_0 + \sum_{\ell=0}^{\infty} \big[a_\ell i_\ell(\bar{\kappa}r) + b_\ell k_\ell(\bar{\kappa}r)\big] P_\ell(x), \tag{3.20}$$

where i_ℓ and k_ℓ are the modified spherical Bessel functions of the first and second kinds, respectively. The coefficients a_ℓ and b_ℓ are integration constants that we fix by matching the full LPB solution at $r = R$, to $\Phi_\ell(R) \equiv \chi_\ell$ and $\Phi'_\ell(R) \equiv \chi'_\ell$ of the nonlinear problem. This leads for every ℓ to the linear two by two problem

$$\chi_\ell = (\chi_0 - \tanh\chi_0)\delta_{\ell,0} + a_\ell i_\ell(\bar{\kappa}R) + b_\ell k_\ell(\bar{\kappa}R), \tag{3.21}$$

$$\chi'_\ell = \bar{\kappa}\Big(a_\ell i'_\ell(\bar{\kappa}R) + b_\ell k'_\ell(\bar{\kappa}R)\Big), \tag{3.22}$$

which results in explicit expressions for a_ℓ and b_ℓ given by

$$a_\ell = \frac{\nu_\ell\left(k_{\ell+1}(\bar{\kappa}R) - \frac{\ell}{\bar{\kappa}R}k_\ell(\bar{\kappa}R)\right) + \chi'_\ell k_\ell(\bar{\kappa}R)}{i_\ell(\bar{\kappa}R)k_{\ell+1}(\bar{\kappa}R) + i_{\ell+1}(\bar{\kappa}R)k_\ell(\bar{\kappa}R)}, \tag{3.23}$$

$$b_\ell = \frac{\nu_\ell\left(i_{\ell+1}(\bar{\kappa}R) + \frac{\ell}{\bar{\kappa}R}i_\ell(\bar{\kappa}R)\right) - \chi'_\ell i_\ell(\bar{\kappa}R)}{i_\ell(\bar{\kappa}R)k_{\ell+1}(\bar{\kappa}R) + i_{\ell+1}(\bar{\kappa}R)k_\ell(\bar{\kappa}R)}, \tag{3.24}$$

where $\nu_\ell = \chi_\ell - (\chi_0 - \tanh\chi_0)\delta_{\ell,0}$. The dashed curves in Fig. 3.3(b) are the result of such a far-field fit. With a_ℓ and b_ℓ explicitly known, one can extrapolate the LPB solution to $r = a$ to yield, with (3.13) and standard Bessel function relations, the renormalized multipoles

$$\sigma^*_\ell = -\frac{\bar{\kappa}}{4\pi l_B}\Big(a_\ell i_{\ell+1}(\bar{\kappa}a) - b_\ell k_{\ell+1}(\bar{\kappa}a)\Big). \tag{3.25}$$

This expression is the multipole generalization of the well-known charge renormalization [78–82].

A first illustration of multipole renormalization is shown in Fig. 3.3(b). There, the angles represent slope discontinuities at $r = a$ which are proportional to σ_ℓ (nonlinear theory) and σ^*_ℓ (far-field fit). For $\ell = 0, 1$ we see $\sigma^*_\ell < \sigma_\ell$, which means that the effective charge and dipole are renormalized downward. Interestingly, however, for $\ell = 2$ the inset in the lowest panel reveals upward renormalization since $\sigma^*_2 \neq 0$ while $\sigma_2 = 0$, that is, the Janus particle has a mode-coupling induced far-field quadrupole signature. Multipole renormalization is quantified further in Figs. 3.4–3.6, where (scaled) renormalized multipoles $Z^*_\ell = 4\pi a^2\sigma^*_\ell$ are shown for the monopole $\ell = 0$ in Fig. 3.4, the dipole $\ell = 1$ in Fig. 3.5 (scaled with g), and the higher-order multipoles $\ell = 1$–6 in Fig. 3.6. All multipoles are shown as a function of $Z_0 l_B/a$. Furthermore, in Fig. 3.4 and 3.5, we chose several truncation levels L and heterogeneities g, and also

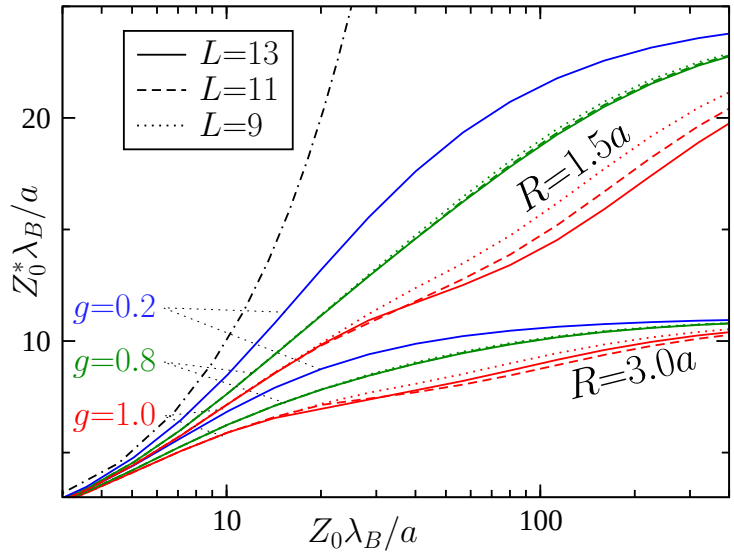

Figure 3.4: Renormalized (scaled) monopole Z_0^* for several g, L (see text) of a Janus sphere as a function of the total charge $Z_0 l_B/a$. The graph includes data for cell radii $R/a = 1.5$ and $R/a = 3.0$. The dot-dashed curve denotes $Z_0^* = Z_0$.

picked two cell radii R. The dot-dashed curves denote the linear limit $Z_\ell^* = Z_\ell$. Figures 3.4 and 3.5 show that all curves for $L = 13$ superimpose on those of $L = 9, 11$ for all Z_0 and $g \lesssim 0.8$, indicative of excellent convergence in this parameter regime; for $g = 1$ the convergence deteriorates for $Z_0 l_B/a \gtrsim 15$. The R dependence in Figs. 3.4 and 3.5 shows the strongest renormalization in the largest cell, not unlike the homogeneous-charge case [78–82]. Interestingly, in the nonlinear regime $Z_0 l_B/a \gtrsim 10$, Fig. 3.4 shows a mode-coupling induced reduction of Z_0^* by 10s of percents when g increases from 0 to 1. In other words, in contrast to the more usual 'linear' electrostatics we now have a far-field monopole potential that is not only determined by the net charge but in fact also by the charge heterogeneity. This is a key finding, relevant for understanding patchy-particle interactions. The mode coupling has an even stronger effect on renormalization of Z_1^*, for which Figs. 3.5(a) and 3.5(b) show a pronounced maximum in between the low-Z_0 linear-screening regime and the high-Z_0 regime in which Z_1^* becomes even *vanishingly small* for all gs considered. Fig. 3.6 shows, for $g = 0.4$, that in fact *all* Z_ℓ^* with $\ell \neq 0$ vanish in the limit of large Z_0, while they all show an intermediate regime with finite values even for $\ell = 2, 4, 6$, for which $\sigma_\ell = 0$. The underlying physics for non-oppositely charged hemispheres with $\sigma_N > \sigma_S > 0$ (that is,

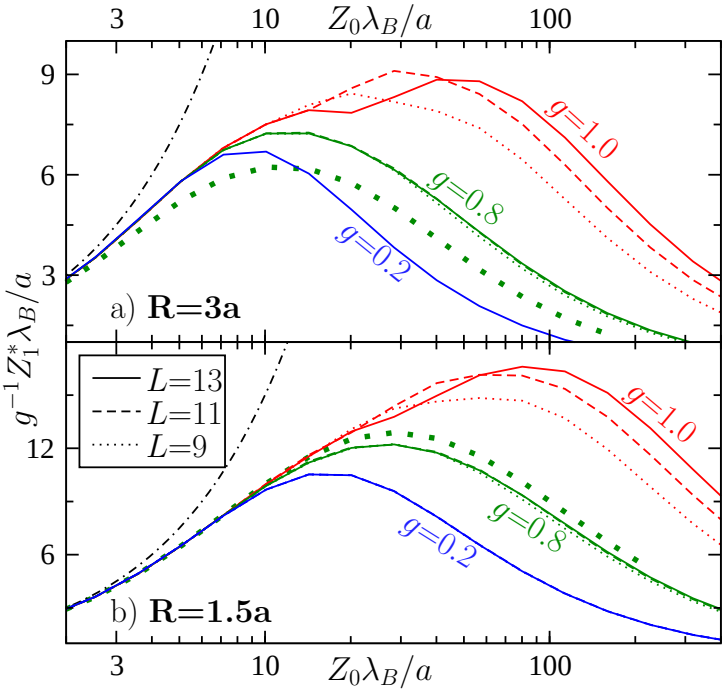

Figure 3.5: Renormalized (scaled) dipole Z_1^* for several g, L (see text) of a Janus sphere as a function of the total charge $Z_0 l_B/a$. The upper and the lower graph represent cell sizes $R/a = 3.0$ and $R/a = 1.5$ respectively. The thick dotted lines denote the (scaled) difference of the renormalized northern and southern charge presumed distributed homogeneously (see text) for $g = 0.8$. The dot-dashed curves in both graphs denote $Z_1^* = Z_1$.

with $0 < g < 1$) is that both σ_N and σ_S renormalize, if both are high enough, to the same saturated value, giving rise to a pure far-field monopole without multipoles.

The idea might emerge that both hemispheres renormalize their charge independent of each other, that is, some of the results could suggest that the renormalized charge density on the colloidal surface is a function which depends only locally on the bare charge density. If that were the case, it would suffice to calculate the renormalized surface charge-density for σ_N and σ_S, as if both were the charge density of a monopole. The cell radius is to be kept unchanged. The thick dotted lines in Figs. 3.5(a) and 3.5(b) denote the resulting dipole charge for $g = 0.8$, which is calculated with the obtained (renormalized) σ_N^* and σ_S^* by $\frac{3}{4}(\sigma_N^* - \sigma_S^*)$. The correspondence with the solid line is at best reasonable but not perfect. Also the effective monopole is

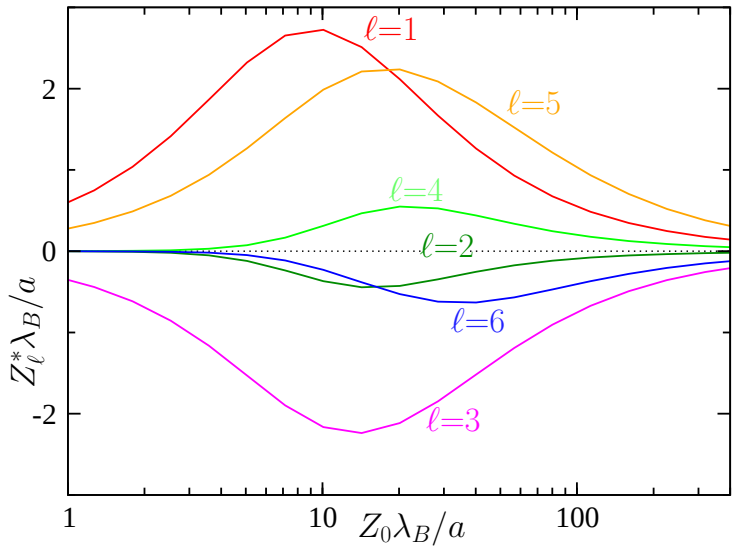

Figure 3.6: Renormalized (scaled) multipoles Z_ℓ^* of a Janus sphere as a function of the total charge $Z_0 l_B/a$. The parameters here are $g = 0.4$ and $L = 13$.

not accurately predicted. This can can be seen from Fig. 3.7, where we investigate the cell-size dependence of the the effective monopole for $g = 0.4, 0.8$ and for $\kappa a = 1, 3$. We included data from the full theory (depicted by symbols) and the predicted values by $2\pi a^2(\sigma_N^* + \sigma_S^*)$ as a solid line. One can see that the monopole charge is underestimated for a wide range of cell radii, especially for larger cells. Nevertheless, there is qualitative agreement on the increase of the renormalized charge with higher values for κa. The difference with the full theory is expected to be the largest for very heterogeneously charged particles. Indeed, we see the largest discrepancy in Figs. 3.7(a) and 3.7(b) for $g = 0.8$. Apparently, the interactions between the hemispheres do play a role, which in fact can also be concluded from the induced multipoles of even orders in Fig. 3.6. Further research might give more insight into the characteristics of these interactions.

3.6 Discussion and Conclusion

The newly emerging general picture is that nonlinear ionic screening of heterogeneously distributed surface charges strongly affects the far-field symmetry of the potential, and hence also the symmetry of the effective interactions and the self-assem-

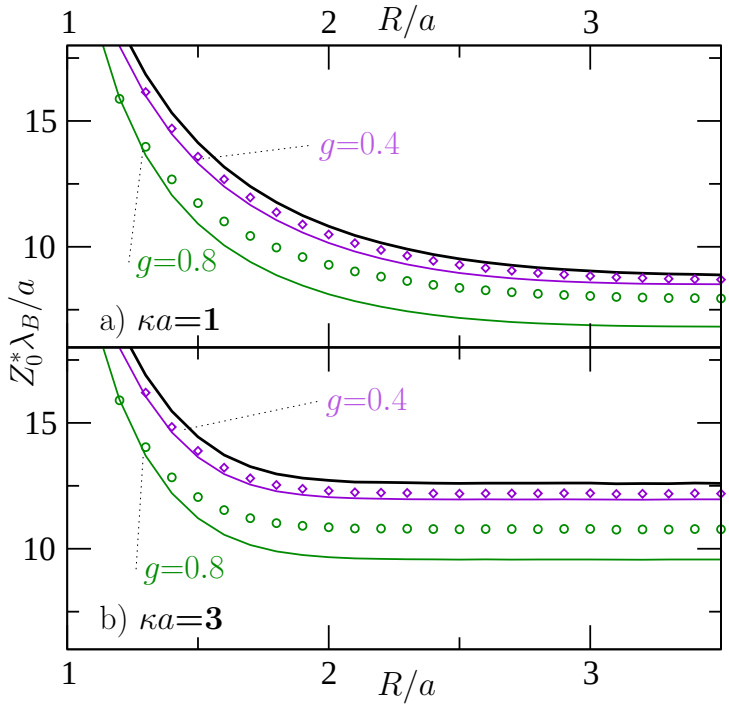

Figure 3.7: Renormalized monopole charge Z_0^* for several g of a Janus sphere as a function of the cell size R, both for $Z_0 l_B/a = 22.5$, in (a) for $\kappa a = 1$ and in (b) for $\kappa a = 3$. The thick solid line corresponds to a pure bare monopole, yielding $g = 0$. The diamonds ($g = 0.4$) and circles ($g = 0.8$) show the data from the full theory, using $L = 13$. The thinner solid lines denote the average of the renormalized northern and southern charge presumed distributed homogeneously (see text) for $g = 0.4$ and $g = 0.8$.

bling structures. The systematics of the present screening theory could be a firm basis to further study these intricate features of heterogeneously charged particles. The category of particles which are described by $g > 1$, carrying positive and negative charges on the two hemispheres, are particularly interesting. Because the present method is not very efficient at high values of g, we have developed an alternative method to treat these mainly dipolar particles within a mode expansion as well. This will be presented in further work.

It is tempting to model Janus spheres by a Yukawa-segment model [28] in which every surface element $\mathrm{d}S$ contributes $\sigma^*(x) l_B s^{-1} \exp[-\kappa s]\mathrm{d}S$ to the (dimensionless) potential at a distance s. Here the renormalized charge densities on both hemispheres

is obtained from the renormalized monopole and dipole charge density via

$$\sigma^*(x) = \begin{cases} \sigma_0^* + \frac{2}{3}\sigma_1^* & \text{for } x < 0, \\ \sigma_0^* - \frac{2}{3}\sigma_1^* & \text{for } x \geq 0. \end{cases} \tag{3.26}$$

The dotted curves in Fig. 3.3(a) show that agreement with our full calculations is reasonable though not quantitative. The Yukawa model ignores the ionic hard-core exclusion and the non-vanishing anisotropic electric fields in the interior of the particle. Therefore, effectively it describes the (dimensionless) potential of a charge configuration in which oppositely charged ions were able to approach the heterogeneously charged surface from two sides, such that this potential is more suppressed compared to the full theory.

We return to the choice of the boundary conditions on the cell surface (3.10), which we called 'isotropic' BCs. This denomination follows from the fact that, considering two randomly oriented neighboring cells, the cell-surface potentials of two cells should match on the spot where they touch, giving rise to a constant cell-surface potential. Nevertheless the choice of BCs is not unique. We can also supply the system with 'nematic' boundary conditions, corresponding to the situation that all cells are perfectly aligned such that cells only touch on opposite spots. On these spots the electrostatic potential should match, and we can also demand continuity of the electric field. The BCs then become

$$\begin{aligned} \Phi(R,\theta,\varphi) &= \Phi(R,\pi-\theta,\pi+\varphi), \\ \Phi'(R,\theta,\varphi) &= -\Phi'(R,\pi-\theta,\pi+\varphi). \end{aligned} \tag{3.27}$$

In fact one can even interpolate between 'isotropic' and 'nematic' BCs by introducing an orientation distribution function, which will be discussed in chapters 4 and 5. In the present chapter, we only consider systems in which the description using isotropic BCs, given by (3.10), is reasonable. However, for the parameters used in this chapter, it turns out that this particular choice for the BCs did not noticeably affect the values of the renormalized charges. We do not see a significant change by turning to nematic BCs (3.27). This insensitivity to the choice of BCs is due to the fact that the nonlinear behavior is an effect which takes place close to the colloidal surface, where these BCs have the least influence on the electrostatic potential. Furthermore, the only multipoles which are directly affected by the particular choice of BCs are the nonzero ($\ell > 0$) even multipoles, which are small for Janus particles. We therefore think that the obtained values for the renormalized multipoles can be applied in a model to describe the behavior of a many-body system within linear theory, no matter what the orientations of the surrounding colloids are. Since the monopole and multipole potentials decay for large r equally fast as $\exp[-\bar{\kappa}r]/r$ [90], where $\bar{\kappa}^{-1}$ is the decay length,

the higher-order renormalized multipole charges are expected to contribute in dense as well as dilute systems.

In summary, we developed a systematic framework for nonlinear ionic screening of heterogeneously charged spheres. The scheme allows for an explicit far-field analysis that generalizes charge renormalization from the well-studied homogeneous case (pure monopoles) [78–82] to the heterogeneous case (dipoles, quadrupoles, etc. and their nonlinear couplings). Application to charged Janus spheres shows (i) a 40% reduction of the effective monopole for $g = 1$ (charged and uncharged hemisphere) compared to $g = 0$ (homogeneously charged sphere), (ii) a mode-coupling induced far-field effective quadrupole component without an actual surface quadrupole, (iii) a pure far-field monopole with vanishing higher-order multipoles in the saturated high-charge limit, and (iv) no quantitative agreement with a simple Yukawa-segment model based on renormalized multipoles. Our study opens the way to systematic microscopic calculations of effective electrostatic interactions between Janus (and other patchy) particles. In addition, our analyses reveal non-vanishing electric fields inside heterogeneously charged particles, which could couple to interior dipoles and affect (anisotropic) mutual Van der Waals forces. Given that the presently introduced expansion technique can be generalized to other geometries—for example, patterned planar surfaces or ellipsoidal patchy colloids—our technique and findings are directly relevant for gaining microscopic understanding of effective interactions and ultimately phase behaviour of a large class of dispersions of patchy or patterned nanoparticles, colloids, or proteins [1].

Acknowledgement

We thank Niels Boon, Elma Carvajal Gallardo, and Stephan Zheng for performing all numerical calculations presented in this chapter.

The work presented in this chapter has been accepted for publication in the article:
"Screening of heterogeneous surfaces: Charge renormalization of Janus particles"
J. Phys.: Condens. Mat., expected publication: June 2010.

Chapter 4

A cell model for heterogeneously charged colloids

Abstract

In this chapter, we extend the original Poisson-Boltzmann cell model by, for example, Marcus [91], Ohtsuki et al. [92] and Alexander et al. [78]. The goal is to formulate a model that can be used to describe suspensions of heterogeneously charged colloidal particles. We introduce some basic concepts on which we build this model. An application will be treated in chapter 5.

4.1 Introduction

The Poisson-Boltzmann (PB) cell model, as formulated by Alexander et al. [78], is a simplified description of a many-body system of homogeneously charged colloidal spheres. In this description, only a single colloidal particle is considered in the center of a spherical cell with a volume that is equal to the volume per particle. Through this simplification, a lot of detail of the system is discarded. However, due to its simplicity, the model can be quite useful. We would like to apply the same kind of simplification to the description of anisotropic charged colloidal particles. Anisotropy in charged colloidal systems can stem from two different sources. First, the shape of the charged colloidal particle can be anisotropic (e.g., ellipsoidal or cylindrical). Second, the charge distribution on a colloidal sphere can be heterogeneous (e.g., patches

or stripes). In both cases, each particle in the suspension has a distinct orientation, as well as a position. This means that we have to describe such systems by characterizing the orientational distribution as well as the positional distribution. Our generalization of the PB cell model includes a description of the orientational distribution of the colloidal particles, as well as a possibility to choose nonspherical cell shapes. The basis of our model is the generalization of the Poisson-Boltzmann cell model by Biesheuvel et al. [93] considering mixtures, together with the insight of Onsager [20] that a distribution of orientations can be considered in the same way as mixtures. In principle, this model can be used to predict the phase behavior of a large class of colloidal and nanoparticles, because an anisotropic (as well as spherical) particle shape can be treated. However, here we restrict ourselves to a system of spherical colloidal particles.

4.2 The cell model for mixtures

We start by giving the prerequisites for the ordinary spherically symmetric cell model (see Fig. 4.1). In this simple case, we consider a system of N identical, spherically symmetric colloidal particles in a volume V. These particles have radius a and a surface charge Ze—where e is the elementary charge—assumed to be homogeneously distributed over the particle surface. The system is presumed to be in osmotic contact with a reservoir of monovalent cations and anions at total concentration $2\rho_s$, with charge $\pm e$. Both the particle and the surrounding medium are considered to be dielectric media, where ε_{in} and ε_{out} are the permittivities of the particle and the solvent, respectively.

Within Poisson-Boltzmann theory, one relates the density profiles $\rho_{\pm}(\mathbf{r})$ of the ions to the electrostatic potential $\Psi(\mathbf{r})$ in a fixed configuration of the colloidal particles. This complicated nonlinear N-body problem can be simplified considerably by considering a single colloidal particle in the center of a Wigner-Seitz cell surrounded by the ions. This cell is approximated by a spherical shape (of radius R) instead of space filling. The volume of the cell is fixed by the available volume per particle,

$$\frac{4\pi}{3}R^3 = \frac{V}{N}. \tag{4.1}$$

We treat the ions in a mean-field description, such that we obtain the Poisson-Boltzmann (PB) equation

$$\nabla^2\Phi(\mathbf{r}) = \begin{cases} 0 & \text{for } 0 < |\mathbf{r}| < a, \\ \kappa^2 \sinh\Phi(\mathbf{r}) & \text{for } a < |\mathbf{r}| < R, \end{cases} \tag{4.2}$$

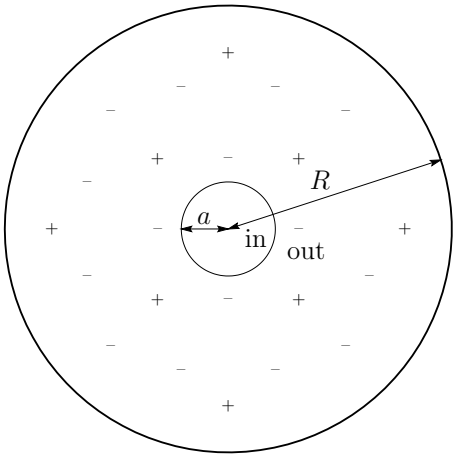

Figure 4.1: Illustration of the Poisson-Boltzmann cell model. A colloidal particle of radius a is surrounded by ions. It is situated in the center of a spherical cell of radius R.

where $\kappa^{-1} = \sqrt{\varepsilon_{\text{out}}/2\rho_{\text{s}}\beta e^2}$ is the Debye screening length, and $\Phi = \beta e \Psi$ is the dimensionless electrostatic potential, where $\beta = 1/k_{\text{B}}T$. This second-order nonlinear partial differential equation describes the electrostatic effects of the ions in the cell volume surrounding the colloidal particle. The boundary conditions are determined by the charge on the particle and the assumption of cell electroneutrality. The first set of boundary conditions is given by

$$\Phi(\mathbf{r})\Big|_{r\uparrow a} = \Phi(\mathbf{r})\Big|_{r\downarrow a}, \tag{4.3}$$

$$\varepsilon_{\text{in}} \frac{\partial}{\partial r}\Phi(\mathbf{r})\Big|_{r\uparrow a} = \beta e^2 \frac{Z}{4\pi a^2} + \varepsilon_{\text{out}} \frac{\partial}{\partial r}\Phi(\mathbf{r})\Big|_{r\downarrow a}, \tag{4.4}$$

which fixes the electric field at the particle surface. In Eq. (4.4), Z is the number of elementary charges on the particle surface. Because of the homogeneous surface charge distribution, there is no electric field inside the particle. This reduces boundary condition (4.4) to

$$\frac{\partial}{\partial r}\Phi(\mathbf{r})\Big|_{r\downarrow a} \equiv \Phi'(a) = -\frac{Z l_{\text{B}}}{a^2}, \tag{4.5}$$

where $l_{\text{B}} = \beta e^2/4\pi\varepsilon_{\text{out}}$ is the Bjerrum length of the solvent. The second boundary condition combines the total system electroneutrality with the presumption that all

cells are equivalent. It fixes the electric field at the cell boundary, according to Gauss' law

$$\Phi'(R) = 0. \tag{4.6}$$

The PB equation (4.2) together with the boundary conditions (4.5) and (4.6) form a closed set and describe the basic Poisson-Boltzmann cell model as studied, for example, in Refs. [78, 80, 94].

Now we discuss the case of a mixture of equally sized homogeneously charged colloidal species with surface charges $Z_i e$. Again, the particles have radius a and are positioned in the center of a spherical cell of radius R. The PB equation (4.2) is solved separately for each colloidal species i, and the notion of electroneutrality is applied to the system as a whole [93]. Each solution $\Phi_i(r)$ is determined by the surface charge density on the corresponding colloidal species

$$\Phi_i'(a) = -\frac{Z_i l_{\mathrm{B}}}{a^2}. \tag{4.7}$$

Given that the cells of each pair of species are considered to be neighboring, it is natural to apply a mean-field description, in which one imposes a common boundary value Φ_R for the potential on every cell surface. This value is—by definition of this mean-field approach—equal to the average value of the electrostatic potential at the cell boundary for different species. Hence, we have

$$\Phi_i(R) = \sum_j x_j \Phi_j(R) \equiv \Phi_R \qquad \forall i, \tag{4.8}$$

where $x_i = N_i/N$ is the molar fraction of species i, such that

$$\sum_i x_i = 1. \tag{4.9}$$

The boundary value Φ_R is fixed by setting the average value of the charge contained in the cells for different species to zero. According to Gauss' law, this is achieved by imposing

$$\sum_i x_i \Phi_i'(R) = 0. \tag{4.10}$$

The PB equation (4.2) applied to each species i together with the boundary conditions (4.7), (4.8), and (4.10) again form a closed set.

When one allows for a different cell radius R_i for each colloidal species, a factor R_i^2 must be included in the summation of Eq. (4.10). This yields a slightly different boundary condition,

$$\sum_i x_i R_i^2 \Phi_i'(R) = 0. \tag{4.11}$$

One subsequently imposes a set of physically motivated conditions on these radii. These conditions must comply with the fact that the average cell volume of the system is given by

$$\frac{4\pi}{3}\sum_i x_i R_i^3 = \frac{V}{N}. \tag{4.12}$$

In the case of mixtures where the charge of all species has the same sign, one can fix each R_i by imposing the condition that the electric field must vanish at the cell boundary of each species [95]. This condition is equivalent with imposing electroneutrality on the cell of each species separately. There is no guarantee, however, that this is possible for a general mixture of charged spheres.

4.3 Heterogeneous charge distributions

We now consider a system of spherical colloidal particles that are *not* homogeneously charged, such as Janus particles [12]. Again, the system consists of N identical spherical particles of radius a in a volume V. We apply the same Poisson-Boltzmann theory, such that the electrostatic potential obeys the PB equation (4.2). As before, we position each particle in a simplified Wigner-Seitz cell, and the PB equation must be solved for each "species." However, the cell shape need not be spherical. Also, in this case we replace the species index i by an orientation $\hat{\omega}$, and each solution is denoted by $\Phi(\hat{\omega};\mathbf{r})$. In the spirit of Onsager, we can view particles of different orientation as different species, and treat this system as a mixture where the different particle species have distinct charge distributions.

In this chapter, we focus on charge distributions that are cylindrically symmetric with respect to the particle orientation $\hat{\omega}$. This enables us to specify this orientation by a pair of angles θ, φ, through

$$\hat{\omega} = (\sin\theta\cos\varphi, \sin\theta\sin\varphi, \cos\theta), \tag{4.13}$$

whereas the general case would require a third *Euler angle* ψ. The charge distribution gives us the boundary condition on the particle surface at each position $a\hat{\mathbf{n}}$,

$$\Phi_{\text{in}}(\hat{\omega};a\hat{\mathbf{n}}) = \Phi_{\text{out}}(\hat{\omega};a\hat{\mathbf{n}}), \tag{4.14}$$

$$\varepsilon\,\hat{\mathbf{n}}\cdot\nabla\Phi_{\text{in}}(\hat{\omega};a\hat{\mathbf{n}}) = 4\pi l_{\text{B}}\sigma(\hat{\omega};\hat{\mathbf{n}}) + \hat{\mathbf{n}}\cdot\nabla\Phi_{\text{out}}(\hat{\omega};a\hat{\mathbf{n}}), \tag{4.15}$$

where $\sigma(\hat{\omega};\hat{\mathbf{n}})$ is the surface charge density (in units of e) that belongs to a particle with an orientation $\hat{\omega}$, and $\varepsilon = \varepsilon_{\text{in}}/\varepsilon_{\text{out}}$ is the relative dielectric constant of the particle with respect to the surrounding solvent. The labels "in" and "out" denote the solutions inside the colloidal particle and outside the particle, respectively.

4.3.1 Cell shapes

We want to formulate our model, such that it contains a description for nonspherical cell shapes. Such a description may prove important in the prediction of orientational-symmetry breaking, where the mean distance between particles is directionally dependent. In such cases, the approximation of Wigner-Seitz cells as spherical becomes very poor. To keep our description as comprehensible as possible, we first give a formulation in the context of a mixture of particles, such that we have a discrete number of species. Afterwards, we will generalize this description towards a continuous particle-orientation distribution.

Consider the (closed convex) cell surface—belonging to species i—defined by the set

$$S_i = \left\{ \mathbf{R}_i(\alpha,\beta) \middle| \alpha \in [0,\pi], \beta \in [0,2\pi] \right\}, \tag{4.16}$$

where we parameterize the surface by the spherical angles α and β. These angles are not the standard spherical coordinates, but those of the surface normal unit vector with respect to the laboratory frame,

$$\hat{\mathbf{n}}(\alpha,\beta) = (\sin\alpha\cos\beta, \sin\alpha\sin\beta, \cos\alpha). \tag{4.17}$$

A useful quantity in the description of surfaces is the *metric*, which determines the relation between infinitesimal distances on the surface and variations in the parameterization coordinates. The metric of this surface is defined by the tensor

$$g_{\mu\nu} = \partial_\mu \mathbf{R}_i(\alpha,\beta) \cdot \partial_\nu \mathbf{R}_i(\alpha,\beta), \tag{4.18}$$

where ∂_μ denotes differentiation with respect to the variable $\mu \in \{\alpha,\beta\}$. In some of the following expressions, we omit the argument (α,β) for readability. The choice of parameterization is special in the sense that one can relate the Jacobian

$$\sqrt{g} \equiv \sqrt{\det[g_{\mu\nu}]} = \sqrt{[(\partial_\alpha \mathbf{R}_i)\cdot\partial_\alpha \mathbf{R}_i][(\partial_\beta \mathbf{R}_i)\cdot\partial_\beta \mathbf{R}_i] - [(\partial_\alpha \mathbf{R}_i)\cdot\partial_\beta \mathbf{R}_i]^2}, \tag{4.19}$$

to the Gaussian curvature $K_i(\alpha,\beta)$ by a very simple relation,

$$\sqrt{g} = \frac{\sin\alpha}{K_i(\alpha,\beta)}. \tag{4.20}$$

The Gaussian (or intrinsic) curvature is equal to $(R_1 R_2)^{-1}$, where R_1 and R_2 are the two radii of curvature that locally determine the shape of the surface. The nature of the relation in Eq. (4.20) can be understood by the fact that the surface locally resembles an ellipsoid. It is parameterized in such a way that the two distinct radii of curvature are related to the two orthogonal directions associated with the spherical angles α and

β. For each of these directions, the proper integration measure is related to a radius of curvature. The factor $\sin\alpha$ is due to the spherical nature of the angles α and β. One calculates the Gaussian curvature, at position $\mathbf{R}_i(\alpha,\beta)$ on the cell surface of species i, by using the following expression:

$$K_i(\alpha,\beta) = \frac{\det[k_{\mu\nu}]}{g}, \tag{4.21}$$

where

$$k_{\mu\nu} \equiv (\partial_\mu \hat{\mathbf{n}}) \cdot \partial_\nu \mathbf{R}_i \tag{4.22}$$

is the curvature tensor.

To make the generalization toward a continuous orientational distribution, we simply replace the notation of the Gaussian curvature in Eq. (4.20) by $K(\hat{\omega};\hat{\mathbf{n}})$, and of the cell shape by the function $\mathbf{R}(\hat{\omega};\hat{\mathbf{n}})$.

4.3.2 The boundary conditions

The reason for giving the identity in Eq. (4.20) is to determine boundary conditions that are imposed locally on a curved cell surface. Since we no longer have spherical symmetry, these conditions are determined by the position on the cell surface as well as the local curvature. We will now generalize the expressions in Eqs. (4.8) and (4.11), such that they apply to the system of interest. The following approach is illustrated by Fig. 4.2, which shows the directionality that must be included in the appropriate boundary conditions.

First, we generalize the concept of a fixed cell surface potential, as given by Φ_R in Eq. (4.8). Similar to the cell model for mixtures, the value of this potential is defined as the average value of the electrostatic potential at the cell boundary for different species. However, the average value is taken at the position of opposite orientation

$$\Phi(\hat{\omega};\mathbf{R}(\hat{\omega};\hat{\mathbf{n}})) = \langle\Phi\rangle_R(-\hat{\mathbf{n}}) \equiv \Phi_R(-\hat{\mathbf{n}}) \qquad \forall\hat{\omega}, \tag{4.23}$$

and instead of a summation over species weighted by the molar fractions x_i, we have an integration over particle orientations $\hat{\omega}$ weighted by the orientational distribution function (ODF) $f(\hat{\omega})$

$$\Phi_R(\hat{\mathbf{n}}) \equiv \int \mathrm{d}\hat{\omega} f(\hat{\omega})\Phi(\hat{\omega};\mathbf{R}(\hat{\omega};\hat{\mathbf{n}})). \tag{4.24}$$

This distribution is normalized such that

$$\int \mathrm{d}\hat{\omega} f(\hat{\omega}) = 1. \tag{4.25}$$

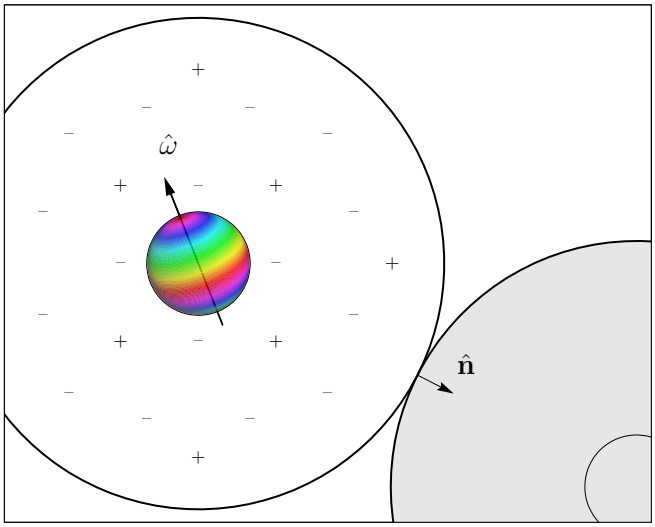

Figure 4.2: Illustration of the Poisson-Boltzmann cell model for heterogeneous charge distributions. For each direction $\hat{\mathbf{n}}$ perpendicular to the cell surface, we determine the appropriate boundary conditions.

The boundary condition (4.23) ensures that the potential of two touching cells—at positions $\mathbf{R}(\hat{\omega};\hat{\mathbf{n}})$ and $\mathbf{R}(\hat{\omega}';-\hat{\mathbf{n}})$, respectively—belonging to arbitrary "species" $\hat{\omega}$ and $\hat{\omega}'$ is continuous. Consequently, the definition of the cell surface potential $\Phi_R(\hat{\mathbf{n}})$ is such that it is always an even function

$$\Phi_R(\hat{\mathbf{n}}) = \Phi_R(-\hat{\mathbf{n}}). \tag{4.26}$$

Second, we have to impose a boundary condition that fixes this cell surface potential. However, if we only impose global electroneutrality on the system, we obtain a boundary condition that is too general for a solution that is *not* spherically symmetric. It would ensure that the average value (over all "species") of the charge contained in each Wigner-Seitz cell vanishes. By applying Gauss' law, we see that this condition is satisfied by setting the average value of the electric field integrated over the surface to zero

$$\int \mathrm{d}\hat{\mathbf{n}} \int \mathrm{d}\hat{\omega} f(\hat{\omega}) \frac{\hat{\mathbf{n}} \cdot \nabla\Phi(\hat{\omega};\mathbf{R}(\hat{\omega};\hat{\mathbf{n}}))}{K(\hat{\omega};\hat{\mathbf{n}})} = 0, \tag{4.27}$$

where the curvature $K(\hat{\omega};\hat{\mathbf{n}})$ appears as a part of the integration measure $\mathrm{d}S = \mathrm{d}\hat{\mathbf{n}}/K$ by virtue of Eq. (4.20). Interestingly, the global electroneutrality condition (4.27) fixes

only the isotropic contribution to the cell surface potential. Therefore, we impose an additional condition that is based on the concept of continuity of the electric field flux from one cell to another. The difference between the outward flux at the cell boundary and the average inward flux of neighboring cells is represented by

$$\Delta F(\hat{\omega};\hat{\mathbf{n}}) \equiv \frac{\hat{\mathbf{n}}\cdot\nabla\Phi(\hat{\omega};\mathbf{R}(\hat{\omega};\hat{\mathbf{n}}))}{K(\hat{\omega};\hat{\mathbf{n}})} - \int \mathrm{d}\hat{\omega}' f(\hat{\omega}') \frac{\hat{\mathbf{n}}\cdot\nabla\Phi(\hat{\omega}';\mathbf{R}(\hat{\omega}';-\hat{\mathbf{n}}))}{K(\hat{\omega}';-\hat{\mathbf{n}})}, \tag{4.28}$$

where the curvature $K(\hat{\omega};\hat{\mathbf{n}})$ is included to represent the curvature dependence of the infinitesimal excess flux in the set of orientations within $\mathrm{d}\hat{\mathbf{n}}$ around $\hat{\mathbf{n}}$. This quantity is averaged over all particle orientations and set to zero, in order to insure global electric field flux conservation

$$\langle \Delta F \rangle_R(\hat{\mathbf{n}}) = 0, \tag{4.29}$$

which is equivalent to imposing

$$\hat{\mathbf{n}}\cdot\left\langle \frac{\nabla\Phi}{K} \right\rangle_R (\hat{\mathbf{n}}) = \hat{\mathbf{n}}\cdot\left\langle \frac{\nabla\Phi}{K} \right\rangle_R (-\hat{\mathbf{n}}), \tag{4.30}$$

This condition does fix the cell surface potential, and it defines an average boundary value of the electric field flux such that it is an odd function of $\hat{\mathbf{n}}$. Finally, one has the freedom to choose a different cell shape for each orientation $\hat{\omega}$ as long as the average cell volume is equal to the available volume per particle

$$\int \mathrm{d}\hat{\omega} f(\hat{\omega}) v(\hat{\omega}) = \frac{V}{N}, \tag{4.31}$$

where $v(\hat{\omega})$ is the volume of the cell that belongs to orientation $\hat{\omega}$. Analogous to the cell model for mixtures described in Sec. 4.2, we must impose a set of physically motivated conditions on these cell shapes. The cell volume—as well as the cell shape relative to the orientation $\hat{\omega}$—may well depend on the degree of orientational-symmetry breaking. If orientational symmetry is broken, minimization of free energy may favor disproportionate partitioning of the total volume over particles of different orientation.

4.3.3 Equally sized spherical cells

To illustrate the general procedure of our cell model, we present a simple special case here. Since our model does not impose any restrictions on the choice of cell shapes, other than Eq. (4.31), we are allowed to choose the same cell shape for all "species": a sphere of radius R. To this end, we set

$$\mathbf{R}(\hat{\omega};\hat{\mathbf{n}}) = R\hat{\mathbf{n}} \qquad \forall\hat{\omega}, \tag{4.32}$$

where $(4\pi/3)R^3 = V/N$. We fix the position of each particle at the center of the spherical Wigner-Seitz cell, and the PB equation must be solved for each orientation. The set of boundary conditions at the particle surface given by (4.14) and (4.15) is applied unchanged. However, the boundary condition (4.23) can be simplified to

$$\Phi(\hat{\omega}; R\hat{\mathbf{n}}) = \langle\Phi\rangle_R(-\hat{\mathbf{n}}) \equiv \Phi_R(-\hat{\mathbf{n}}) \qquad \forall\hat{\omega}, \tag{4.33}$$

where

$$\langle\Phi\rangle_R(\hat{\mathbf{n}}) = \int \mathrm{d}\hat{\omega} f(\hat{\omega})\Phi(\hat{\omega}; R\hat{\mathbf{n}}). \tag{4.34}$$

The boundary condition (4.30) leads to the condition

$$\hat{\mathbf{n}} \cdot \langle\nabla\Phi\rangle_R(\hat{\mathbf{n}}) = \hat{\mathbf{n}} \cdot \langle\nabla\Phi\rangle_R(-\hat{\mathbf{n}}), \tag{4.35}$$

where we have multiplied both sides of the equation with a factor $K = R^{-2}$. We will use the boundary conditions (4.33) and (4.35) in chapter 5. There we apply this model to spherical colloidal particles with a cylindrically symmetric charge distribution, in the approximation of linearized Poisson-Boltzmann theory.

4.4 Special limiting cases: perfectly isotropic and perfectly aligned

In this section, we apply specific choices for the ODF. In turn, these choices yield a specific form for the boundary conditions (4.23) and (4.30). The resulting models are less intricate than the full model we presented in the previous section. Also, these models yield boundary conditions that one would expect from a naive description of such systems.

Let us take a look at the model that our boundary conditions yield when we implement specific ODFs. First, we consider a perfectly isotropic orientational distribution

$$f_{\mathrm{iso}}(\hat{\omega}) = \frac{1}{4\pi}. \tag{4.36}$$

Since in such a system there is no preferential direction, we argue that all solutions—for different particle orientations—are equivalent. Also, the cell shape of all "species" should be invariant under simultaneous rotations of the particle orientation and the surface unit normal vector,

$$\mathbf{R}_{\mathrm{iso}}(\hat{\omega}; \hat{\mathbf{n}}) \equiv \mathbf{R}_{\mathrm{iso}}(\hat{\omega} \cdot \hat{\mathbf{n}}). \tag{4.37}$$

Consequently, the cell surface potential $\Phi_R(\hat{\mathbf{n}})$ is independent of the position on the cell surface

$$\Phi_{\mathrm{iso}}(\hat{\omega}; \mathbf{R}_{\mathrm{iso}}(\hat{\omega} \cdot \hat{\mathbf{n}})) = \Phi_R. \tag{4.38}$$

This result is in accordance with the notion that in the isotropic case the average over all particle orientations [Eq. (4.24)] is equal to the average over all orientations $\hat{\mathbf{n}}$ of the position on the cell surface, and that this average no longer depends on either orientation. Therefore, the boundary condition (4.30) is equivalent to the condition that each cell is electroneutral

$$\hat{\mathbf{n}} \cdot \left\langle \frac{\nabla \Phi_{\mathrm{iso}}}{K} \right\rangle_R (\hat{\mathbf{n}}) = \int \mathrm{d}\hat{\mathbf{n}} \frac{\hat{\mathbf{n}} \cdot \nabla \Phi_{\mathrm{iso}}(\hat{\omega}; \mathbf{R}_{\mathrm{iso}}(\hat{\omega} \cdot \hat{\mathbf{n}}))}{K(\hat{\omega} \cdot \hat{\mathbf{n}})} = 0. \tag{4.39}$$

Alternatively, we can choose a perfectly aligned orientational distribution

$$f_{\parallel}(\hat{\omega}) = \delta(\hat{\omega} - \hat{\mathbf{z}}). \tag{4.40}$$

Clearly, in this case there is only one solution to be determined

$$\Phi_{\parallel}(\hat{\mathbf{z}}; \mathbf{r}) \equiv \Phi_{\parallel}(\mathbf{r}), \tag{4.41}$$

and only one relevant cell shape

$$\mathbf{R}_{\parallel}(\hat{\mathbf{z}}; \hat{\mathbf{n}}) \equiv \mathbf{R}_{\parallel}(\hat{\mathbf{n}}). \tag{4.42}$$

The boundary conditions (4.23) and (4.30) become

$$\Phi_{\parallel}(\mathbf{R}_{\parallel}(\hat{\mathbf{n}})) = \Phi_{\parallel}(\mathbf{R}_{\parallel}(-\hat{\mathbf{n}})), \tag{4.43}$$

$$\frac{\hat{\mathbf{n}} \cdot \nabla \Phi_{\parallel}(\mathbf{R}_{\parallel}(\hat{\mathbf{n}}))}{K(\hat{\mathbf{n}})} = \frac{\hat{\mathbf{n}} \cdot \nabla \Phi_{\parallel}(\mathbf{R}_{\parallel}(-\hat{\mathbf{n}}))}{K(-\hat{\mathbf{n}})}. \tag{4.44}$$

Evidently, the choice of a perfectly aligned orientational distribution leads to periodic boundary conditions, where each position $\mathbf{R}_{\parallel}(\hat{\mathbf{n}})$ on the cell surface is identified with position $\mathbf{R}_{\parallel}(-\hat{\mathbf{n}})$.

Chapter 5

Orientational ordering of heterogeneously charged colloids in a fluid

Abstract

We apply the generalized Poisson-Boltzmann cell model—developed in chapter 4—to spherical colloidal particles with a heterogeneous surface charge distribution. This model was obtained by generalizing existing cell models for mixtures of homogeneously charged colloidal spheres. Our model has similar features as Onsager's second-virial theory for liquid crystals, but it predicts no orientational ordering if there is no positional ordering. This implies that all phases of heterogeneously charged colloids that are liquidlike with respect to translational degrees of freedom are also isotropic with respect to particle orientation.

5.1 Introduction

Already a long time ago, Marcus [91], Ohtsuki et al. [92], and Alexander et al. [78] realized that the cell model approach of Wigner and Seitz [89] to calculate the properties of electrons in solids can also be applied to colloidal matter. In this case, there are no quantum effects and, instead of a wave function, one calculates the ion distributions around charged colloidal particles dispersed in a liquid medium. In the

simplest case, the colloidal dispersion consists of one colloidal species immersed in a 1:1 electrolyte solution. The colloidal particles are homogeneously charged and have a spherical shape. Additionally, the simplification of taking a spherical Wigner-Seitz cell—instead of space filling—is a reasonable approximation in fluid phases with no broken translational symmetry.

A number of extensions has been made to this basic cell model. There is the eccentric Poisson-Boltzmann cell model [92, 96] and the heterogeneous—or polydisperse—cell model [93, 95] to describe mixtures. Additionally, the cell model has been extended by applying cylindrical Wigner-Seitz cells for the description of disk-shaped and rodlike particles [97, 98]. In the present chapter, we make an extension toward particles with a heterogeneous surface charge distribution, such as patterned colloids [1] or Janus particles [12]. Janus particles are characterized by two distinct regions of surface area. Each of these "faces" has a different chemical composition, which can create spontaneous particle aggregation [11]. Our aim is toward a description of self-organization of these particles from single-particle properties. The cell model can be a powerful tool, giving a simple description of these complex systems. From this description, a number of thermodynamic quantities can be derived such as free energy and osmotic pressure.

We investigate how surface charge heterogeneity influences the distribution of particle orientations in the case of a homogeneous positional distribution. This case can be considered as a simplified description of a fluid of these particles but also as an oversimplified description of a solid. The particle interactions are implemented through boundary conditions on the surface of the Wigner-Seitz cell, and we choose to neglect any correlations between the orientational and positional ordering. The basis of our model is the generalization of the Poisson-Boltzmann cell model by Biesheuvel et al. [93] considering mixtures, together with the insight of Onsager [20] that a distribution of orientations can be considered in the same way as mixtures. In principle, this model can be used to predict the phase behavior of a large class of colloidal and nanoparticles because an anisotropic (as well as spherical) particle shape can be treated. However, here we restrict ourselves to a system of spherical colloidal particles.

5.2 Application to linearized Poisson-Boltzmann theory

A solution of the full nonlinear problem in the context of the cell model introduced in chapter 4 can be obtained numerically, but it turns out to be very involved (see chapter 3). Therefore, we restrict ourselves here to the linearized version of Poisson-Boltzmann theory. In this case, the nonlinear right hand side of the PB equation is

linearized around a certain value. We denote it by Φ_0, such that the linearized Poisson-Boltzmann (LPB) equation is given by

$$\nabla^2\Phi_{\text{out}}(\hat{\omega};\mathbf{r}) = \kappa^2\cosh\Phi_0(\Phi_{\text{out}}(\hat{\omega};\mathbf{r}) - \Phi_0) + \kappa^2\sinh\Phi_0. \tag{5.1}$$

In some cases, the value for Φ_0 is chosen to be zero. This choice is meaningful if the concentration of colloids, as well as the total surface charge density, is low. Alternatively, its value can be set to the isotropically averaged value of the potential at the cell boundary. This choice is particularly useful when one has the boundary values of the potential and the electric field from numerical calculations of the nonlinear PB equation—such as ascertained in chapter 3. These can be used to fit renormalized charge distributions on the particle surface using the expression in Eq. (5.5). Lastly, one can apply the Donnan potential as the value around which to perform the linearization. This value requires no other input than the colloid concentration, its particle radius, its total surface charge, and the reservoir salt concentration [94]. In this chapter, we leave Φ_0 unspecified.

Inside the colloidal particle Φ still satisfies the Laplace equation. It is natural in this case to expand both the inner and the outer solutions in spherical harmonics. This leads to two sets of coefficients, which have to be matched at the particle surface. Inside the particle

$$\Phi_{\text{in}}(\hat{\omega};\mathbf{r}) = \sum_{\ell=0}^{\infty}\sum_{m=-\ell}^{+\ell} A_{\ell,m}(\hat{\omega})r^{\ell}Y_{\ell,m}(\theta,\phi), \tag{5.2}$$

whereas in the electrolyte

$$\Phi_{\text{out}}(\hat{\omega};\mathbf{r}) = \Phi_0 - \tanh\Phi_0 + \sum_{\ell=0}^{\infty}\sum_{m=-\ell}^{+\ell}[B_{\ell,m}(\hat{\omega})i_{\ell}(\bar{\kappa}r) + C_{\ell,m}(\hat{\omega})k_{\ell}(\bar{\kappa}r)]Y_{\ell,m}(\theta,\phi), \tag{5.3}$$

where $\bar{\kappa}^2 = \kappa^2\cosh\Phi_0$, and i_ℓ and k_ℓ are the modified spherical Bessel functions of order ℓ of the first and second kinds, respectively. The set of boundary conditions on the particle surface is given by Eqs. (4.14) and (4.15), where we decompose the charge distribution as

$$\sigma(\hat{\omega};\hat{\mathbf{n}}) = \sum_{\ell=0}^{\infty}\frac{2\ell+1}{4\pi}\sigma_{\ell}P_{\ell}(\hat{\omega}\cdot\hat{\mathbf{n}}). \tag{5.4}$$

Next, we impose the boundary conditions at the cell surface, which are given in Eqs. (4.33) and (4.35). Together, this yields the general solution for the dimensionless

electrostatic potential in the cell interior

$$\begin{aligned}\Phi_{\text{out}}(\hat{\boldsymbol{\omega}};\mathbf{r}) = \Phi_0 - \tanh\Phi_0 &\\ + l_{\text{B}}\bar{\kappa}^{-1}\sum_{\ell=0}^{\infty}\frac{(2\ell+1)\sigma_\ell}{\Xi_\ell(\varepsilon;\bar{\kappa}a,\bar{\kappa}R)}\big[k_\ell(\bar{\kappa}r)i_\ell(\bar{\kappa}R) - i_\ell(\bar{\kappa}r)k_\ell(\bar{\kappa}R)\big]P_\ell(\hat{\boldsymbol{\omega}}\cdot\hat{\mathbf{r}}) &\\ + l_{\text{B}}\bar{\kappa}^{-1}\underbrace{\sum_{\ell=0}^{\infty}}_{\ell\text{ even}}\frac{(2\ell+1)\sigma_\ell}{\Lambda_\ell(\varepsilon;\bar{\kappa}a,\bar{\kappa}R)\bar{\kappa}^2R^2\Xi_\ell(\varepsilon;\bar{\kappa}a,\bar{\kappa}R)} &\\ \times\Xi_\ell(\varepsilon;\bar{\kappa}a,\bar{\kappa}r)\int \mathrm{d}\hat{\boldsymbol{\omega}}' f(\hat{\boldsymbol{\omega}}')P_\ell(\hat{\boldsymbol{\omega}}'\cdot\hat{\mathbf{r}}),&\end{aligned} \tag{5.5}$$

where

$$\Xi_\ell(\varepsilon;\bar{\kappa}a,\bar{\kappa}R) \equiv -\left(k_\ell'(\bar{\kappa}a) - \frac{\varepsilon\ell}{\bar{\kappa}a}k_\ell(\bar{\kappa}a)\right)i_\ell(\bar{\kappa}R) + \left(i_\ell'(\bar{\kappa}a) - \frac{\varepsilon\ell}{\bar{\kappa}a}i_\ell(\bar{\kappa}a)\right)k_\ell(\bar{\kappa}R), \tag{5.6}$$

$$\Lambda_\ell(\varepsilon;\bar{\kappa}a,\bar{\kappa}R) \equiv \frac{\partial\Xi_\ell(\varepsilon;\bar{\kappa}a,\bar{\kappa}R)}{\partial(\bar{\kappa}R)}, \tag{5.7}$$

and ε is defined in Sec. 4.3 as the relative dielectric constant of the particle with respect to the surrounding solvent. The details of the derivation of the expression in Eq. (5.5) can be found in appendix B. Note that the first sum (over all ℓ) does not depend on the ODF, whereas it does depend on the particle orientation $\hat{\boldsymbol{\omega}}$. This contribution to the potential is purely due to the particle at the center of the cell, and it vanishes at the cell boundary. Conversely, the second sum (over even ℓ) does not depend on the particle orientation, whereas it does depend on the ODF. This means that it describes the effect of all the surrounding particles. Moreover, it vanishes in the limit of infinite dilution ($R\to\infty$).

The grand potential for the ion distribution in a single cell is given by [94]

$$\begin{aligned}\beta\Omega_{\text{cell}}(\hat{\boldsymbol{\omega}}) = \rho_{\text{s}}\int_{\text{out}}\mathrm{d}\mathbf{r}\big\{\Phi_{\text{out}}(\hat{\boldsymbol{\omega}};\mathbf{r})\sinh[\Phi_{\text{out}}(\hat{\boldsymbol{\omega}};\mathbf{r})] - 2\cosh[\Phi_{\text{out}}(\hat{\boldsymbol{\omega}};\mathbf{r})] + 2\big\} &\\ + \frac{a^2}{2}\int\mathrm{d}\hat{\mathbf{n}}\sigma(\hat{\boldsymbol{\omega}};\hat{\mathbf{n}})\Phi_{\text{out}}(\hat{\boldsymbol{\omega}};a\hat{\mathbf{n}}),&\end{aligned} \tag{5.8}$$

where the label "out" at the integral symbol denotes integration over the cell interior (i.e., the domain of Φ_{out}), and ρ_{s} is the reservoir salt concentration (such that $\kappa^2 = 8\pi l_{\text{B}}\rho_{\text{s}}$). We cannot evaluate this expression analytically. Therefore, we expand the integrant of the first term in Eq. (5.8) to linear order in $\Phi_{\text{out}}(\hat{\boldsymbol{\omega}};\mathbf{r}) - \Phi_0$ to find

$$\beta\Omega_{\text{cell}}(\hat{\boldsymbol{\omega}}) \simeq \beta\Omega_0 + \beta\Omega_{\text{iso}} + \beta\Omega_{\text{int}}, \tag{5.9}$$

where

$$\beta\Omega_0 \equiv \frac{4\pi}{3}(R^3 - a^3)\rho_s(\Phi_0 \sinh\Phi_0 - 2\cosh\Phi_0 + 2), \tag{5.10}$$

$$\beta\Omega_{\rm iso} \equiv \rho_s(\Phi_0\cosh\Phi_0 - \sinh\Phi_0)\int_{\rm out} d\mathbf{r}(\Phi_{\rm out}(\hat{\omega};\mathbf{r}) - \Phi_0), \tag{5.11}$$

$$\beta\Omega_{\rm int} \equiv \frac{a^2}{2}\int d\hat{\mathbf{n}}\sigma(\hat{\omega};\hat{\mathbf{n}})\Phi_{\rm out}(\hat{\omega};a\hat{\mathbf{n}}). \tag{5.12}$$

It turns out that $\beta\Omega_{\rm int}$ depends on the particle orientation and the ODF, whereas the other two terms depend on neither. The expression we obtain can be derived through another route, by expanding the original nonlinear functional of the ion profiles $\rho_\pm(\hat{\omega};\mathbf{r})$ up to second order with respect to a density $\rho_{\pm,0} = \rho_s\exp[\mp\Phi_0]$. Minimizing this functional with respect to the ion profiles yields the LPB equation (5.1), and the accompanying expressions for the ion profiles $\rho_\pm(\hat{\omega};\mathbf{r}) \simeq \rho_{\pm,0}[1 \pm \Phi_0 \mp \Phi_{\rm out}(\hat{\omega};\mathbf{r})]$. Substitution of this expression into the functional yields Eq. (5.9).

5.3 Onsager-like second-order density functional theory

We now approximate the total free energy (per colloidal particle) of the system by averaging over all particle orientations. Also, we add a hard-sphere contribution, and an entropic contribution which is analogous to mixing entropy

$$\frac{\beta\mathscr{F}[f]}{N} \simeq \frac{\beta\mathscr{F}_{\rm HS}}{N} + \int d\hat{\omega} f(\hat{\omega})\ln[4\pi f(\hat{\omega})] + \int d\hat{\omega} f(\hat{\omega})\beta\Omega_{\rm cell}(\hat{\omega}). \tag{5.13}$$

The contribution $\beta\mathscr{F}_{\rm HS}/N$ represents the kinetic and entropic contributions due to the translational degrees of freedom of the colloidal particles. This part will not pose any significance in the rest of this chapter, since we are only interested in the effects of charge anisotropy on the particle-orientation distribution. Using the identity

$$\int d\hat{\mathbf{n}}\sigma(\hat{\omega};\hat{\mathbf{n}})P_\ell(\hat{\omega}'\cdot\hat{\mathbf{n}}) = \sigma_\ell P_\ell(\hat{\omega}\cdot\hat{\omega}'), \tag{5.14}$$

which can be easily derived from Eq. (5.4) using the addition theorem, we derive the following expression for the free energy:

$$\frac{\beta\mathscr{F}[f]}{N} \simeq \frac{\beta\mathscr{F}_0}{N} + \int d\hat{\omega} f(\hat{\omega})\ln[4\pi f(\hat{\omega})] + \frac{1}{2}\int d\hat{\omega} f(\hat{\omega})\int d\hat{\omega}' f(\hat{\omega}')K(\hat{\omega},\hat{\omega}'), \tag{5.15}$$

where

$$\frac{\beta\mathscr{F}_0}{N} \equiv \frac{\beta\mathscr{F}_{\rm HS}}{N} + \beta\Omega_0 + (\Phi_0 - \tanh\Phi_0)\left(\frac{a^2\sigma_0}{2} - \frac{4\pi}{3}(R^3 - a^3)\rho_{\rm s}\sinh\Phi_0\right) + \frac{a^2\sigma_0}{2}(\Phi_0 - \tanh\Phi_0) + \frac{a^2 l_{\rm B}\bar{\kappa}^{-1}}{2}\sum_{\ell=0}^{\infty}\frac{(2\ell+1)\sigma_\ell^2}{\Xi_\ell(\varepsilon;\bar{\kappa}a,\bar{\kappa}R)}\left[k_\ell(\bar{\kappa}a)i_\ell(\bar{\kappa}R) - i_\ell(\bar{\kappa}a)k_\ell(\bar{\kappa}R)\right], \qquad (5.16)$$

and

$$K(\hat{\omega},\hat{\omega}') \equiv \frac{l_{\rm B}}{\bar{\kappa}^5 R^2}\underbrace{\sum_{\ell=0}^{\infty}}_{\ell\ \text{even}}\frac{(2\ell+1)\sigma_\ell^2 P_\ell(\hat{\omega}\cdot\hat{\omega}')}{\Lambda_\ell(\varepsilon;\bar{\kappa}a,\bar{\kappa}R)\Xi_\ell(\varepsilon;\bar{\kappa}a,\bar{\kappa}R)}. \qquad (5.17)$$

Note that the third term of $\beta\mathscr{F}_0/N$ vanishes if one chooses the Donnan potential for the value of Φ_0. Also, the entire contribution from $\beta\mathscr{F}_0/N$ vanishes upon taking the functional derivative with respect to $f(\hat{\omega})$.

The structure of the free-energy functional (5.15) is remarkably similar to that of Onsager's second-virial theory for hard rods [20]. In the case of spherocylinders, the kernel $K(\hat{\omega},\hat{\omega}')$ stems from hard-core interactions, and it is equal to the product of the rod density and the orientation-dependent excluded volume of one rod in the vicinity of another,

$$K(\hat{\omega},\hat{\omega}') = \frac{N}{V}\left[\frac{4\pi}{3}D^3 + 2\pi L^2 D + 2L^2 D\sin\gamma\right], \qquad (5.18)$$

where L is the rod length, D is the rod diameter. The angle $\gamma\in[0,\pi]$ between the two rod orientations is defined by $\cos\gamma \equiv \hat{\omega}\cdot\hat{\omega}'$. Onsager's second-virial theory predicts the existence of an isotropic–nematic transition caused by the competition between orientational and translational entropy. In the low-density isotropic phase, the "mixing" term $\int {\rm d}\hat{\omega} f(\hat{\omega})\ln[4\pi f(\hat{\omega})]$ is minimized by an isotropic orientational distribution, whereas the contribution due to the average excluded volume $\frac{1}{2}\int {\rm d}\hat{\omega} f(\hat{\omega})\int {\rm d}\hat{\omega}' f(\hat{\omega}')K(\hat{\omega},\hat{\omega}')$ is minimized in the high-density nematic phase. This transition only occurs if the length-to-diameter ratio L/D is large, such that the kernel $K(\hat{\omega},\hat{\omega}')$ is sufficiently anisotropic, with a maximum at $\gamma=\pi/2$. In the limit $L\gg D$, the description by Onsager is quantitative.

In the present case, the kernel stems from anisotropic electrostatic interactions, and we will investigate if—under the present approximations—these can give rise to such a symmetry-breaking transition. In both cases, the kernel is rotationally invariant, i.e., it only depends on the mutual relative orientation of the unit vectors $\hat{\omega}$ and $\hat{\omega}'$—through the dot product $\hat{\omega}\cdot\hat{\omega}'$. Figure 5.1 shows the values of the kernel $K(\hat{\omega},\hat{\omega}')$ for two distinct surface charge distributions $\sigma(\hat{\omega},\hat{\mathbf{n}})$. The angle θ between

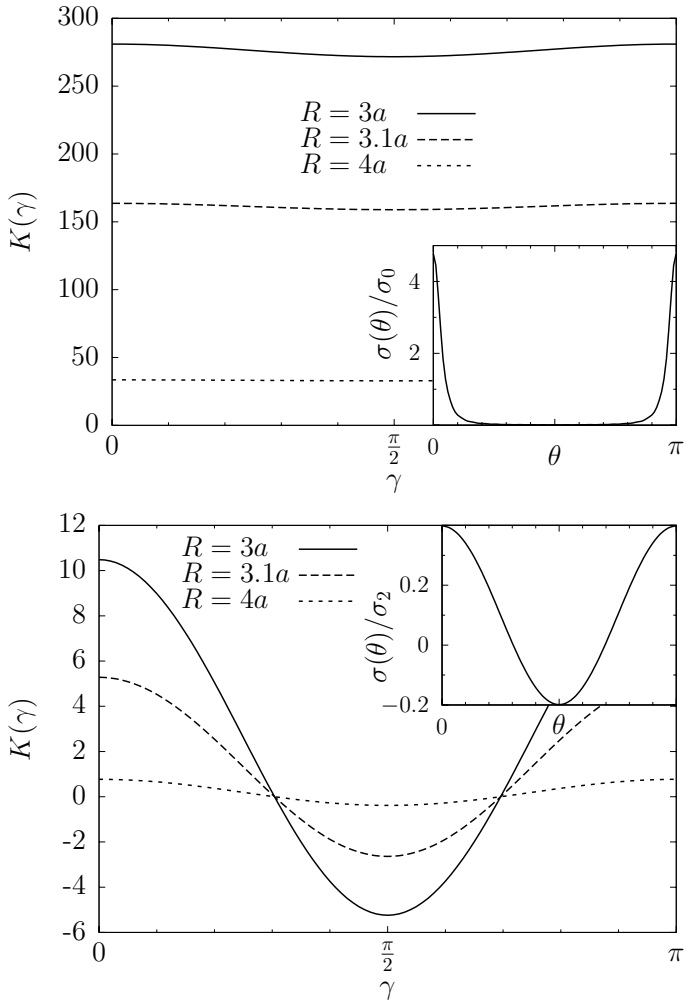

Figure 5.1: The kernel $K(\hat{\omega},\hat{\omega}')$ for different values of the cell radius R, and two distinct charge distributions. We fixed the values $\bar{\kappa}a = 1$, $\varepsilon = 1$, and $\bar{\kappa}l_B = 0.01$. The inset in each graph shows the corresponding charge distribution as a function of the angle θ between the axis of symmetry and the position vector on the surface. The charge distribution in the top graph is scaled with $\sigma_0 = 10^3\bar{\kappa}^2$, whereas the scaling in the lower graph is given by $\sigma_2 = 10^3\bar{\kappa}^2$.

the axis of symmetry and the position vector on the surface is defined by $\cos\theta \equiv \hat{\omega}\cdot\hat{\mathbf{n}}$. The top graph shows a highly peaked distribution around $\theta = 0$ and $\theta = \pi$ in the inset. However, the kernel is much less anisotropic in this case. The lower graph has a purely quadrupolar distribution, which reflects in the fact that the kernel has the same orientational dependence. In both cases, the kernel has a *minimum* at $\gamma = \pi/2$. Consequently, we expect no isotropic–nematic transition. In the next section, we argue that this conclusion holds for any choice of parameters.

5.4 Bifurcation theory

The ODF that minimizes the free energy (5.15) obeys the Euler-Lagrange equation

$$\ln[4\pi f(\hat{\omega})] = \lambda - \int \mathrm{d}\hat{\omega}' f(\hat{\omega}') K(\hat{\omega},\hat{\omega}'), \tag{5.19}$$

where we introduced the Lagrange multiplier λ to ensure the normalization of f given by Eq. (4.25). The Euler-Lagrange equation can be rewritten in a form that always satisfies this normalization

$$f(\hat{\omega}) = \frac{\exp\left[-\int \mathrm{d}\hat{\omega}' f(\hat{\omega}') K(\hat{\omega},\hat{\omega}')\right]}{\int \mathrm{d}\hat{\omega}' \exp\left[-\int \mathrm{d}\hat{\omega}'' f(\hat{\omega}'') K(\hat{\omega}',\hat{\omega}'')\right]}. \tag{5.20}$$

One easily checks that $f_{\mathrm{iso}}(\hat{\omega}) = 1/4\pi$ is a solution of Eq. (5.20), describing the perfectly isotropic phase. Due to its nonlinear character, one can expect additional (anisotropic) solutions to this equation. Finding explicit expressions for these solutions, however, is difficult; although good insight can be obtained from a bifurcation analysis. The goal of this analysis is to determine if—and for what parameters—an instability can be found in the reference solution with respect to a perturbation.

We choose the isotropic ODF (4.36) as a reference, and expand around this solution by writing $f(\hat{\omega}) = 1/4\pi + \delta f(\hat{\omega})$, with δf a small deviation. Following the same scheme as Kayser and Raveché [43] applied to Onsager's model of hard rods, which was extended by Mulder [99], we find the bifurcation equation

$$\delta f(\hat{\omega}) = -\frac{1}{4\pi}\int \mathrm{d}\hat{\omega}' K(\hat{\omega},\hat{\omega}')\delta f(\hat{\omega}') \equiv -\mathscr{K}[\delta f](\hat{\omega}). \tag{5.21}$$

This is an eigenvalue equation, for which a nontrivial solution exists if the integral operator $\mathscr{K}$ has eigenvalues -1. The parameter value for which this occurs is called the bifurcation point, where an anisotropic solution branches off from the (isotropic) reference solution. The solution to the bifurcation equation (5.21) can be given in

terms of eigenfunctions of $\mathscr{K}$. On the basis of rotational-symmetry arguments, we find that these eigenfunctions are the Legendre polynomials of the dot product of the orientation $\hat{\omega}$ with respect to an arbitrary direction,

$$\frac{1}{4\pi}\int \mathrm{d}\hat{\omega}' K(\hat{\omega},\hat{\omega}') P_\ell(\hat{\omega}'\cdot\hat{\mathbf{z}}) = \lambda_\ell P_\ell(\hat{\omega}\cdot\hat{\mathbf{z}}), \tag{5.22}$$

where the eigenvalues λ_ℓ follow from Eq. (5.17),

$$\lambda_\ell = \begin{cases} \dfrac{l_\mathrm{B}}{\bar{\kappa}^5 R^2}\dfrac{\sigma_\ell^2}{\Lambda_\ell(\varepsilon;\bar{\kappa}a,\bar{\kappa}R)\Xi_\ell(\varepsilon;\bar{\kappa}a,\bar{\kappa}R)} & \text{for } \ell \text{ even}, \\ 0 & \text{for } \ell \text{ odd}. \end{cases} \tag{5.23}$$

The bifurcation point is determined by $\lambda_\ell = -1$. However, all eigenvalues λ_ℓ are positive. Therefore, the bifurcation equation (5.21) has no solution, and there is no bifurcation point. The understanding of the origin of this property of the coefficients lies in the fact that both $\Xi_\ell(\varepsilon;\bar{\kappa}a,\bar{\kappa}R)$ and $\Lambda_\ell(\varepsilon;\bar{\kappa}a,\bar{\kappa}R)$ approach their minimum in the limit $R \to a$. Moreover, these limits are non-negative since

$$\lim_{R\to a}\Xi_\ell(\varepsilon;\bar{\kappa}a,\bar{\kappa}R) = \frac{1}{\bar{\kappa}^2 a^2}, \tag{5.24}$$

$$\lim_{R\to a}\Lambda_\ell(\varepsilon;\bar{\kappa}a,\bar{\kappa}R) = \frac{\varepsilon\ell}{\bar{\kappa}^3 a^3}. \tag{5.25}$$

The breaking of orientational symmetry—if it exists—cannot be captured using bifurcation theory in this version of the Poisson-Boltzmann cell model. It is due to the (local) stability of the isotropic solution that holds for all values of the parameters. However, strictly speaking, this does not exclude another (globally) stable solution.

In principle, the Euler-Lagrange equation (5.20) can be solved numerically—for example, by an iteration procedure—for any given charge distribution. Alternatively, it can be rewritten as a (nonlinear) system of equations for the expansion coefficients f_ℓ of the ODF,

$$f(\hat{\omega}) = \sum_\ell \frac{2\ell+1}{4\pi} f_\ell P_\ell(\hat{\omega}\cdot\hat{\mathbf{z}}). \tag{5.26}$$

Using the eigenvalues λ_ℓ to rewrite the Euler-Lagrange equation, we obtain

$$f_\ell = \frac{\displaystyle\int \mathrm{d}\hat{\omega} P_\ell(\hat{\omega}\cdot\hat{\mathbf{z}}) \exp\left[-\sum_{\ell'}(2\ell'+1) f_{\ell'}\lambda_{\ell'} P_{\ell'}(\hat{\omega}\cdot\hat{\mathbf{z}})\right]}{\displaystyle\int \mathrm{d}\hat{\omega} \exp\left[-\sum_{\ell'}(2\ell'+1) f_{\ell'}\lambda_{\ell'} P_{\ell'}(\hat{\omega}\cdot\hat{\mathbf{z}})\right]}. \tag{5.27}$$

All solutions satisfy $f_0 = 1$, and $f_\ell = 0$ for ℓ odd, independent of the choice of charge distribution. Additionally, if we impose the simple form

$$K(\hat{\omega}, \hat{\omega}') = \lambda_0 + \lambda_2 P_2(\hat{\omega} \cdot \hat{\omega}'), \tag{5.28}$$

then the right-hand side of Eq. (5.27) can be calculated analytically for any given value of ℓ. The resulting expression for $\ell = 2$ is a function of the product $f_2\lambda_2$, which we denote by $g(f_2\lambda_2)$. It has the property that $g(t) > 0$ for $t < 0$, $g(t) < 0$ for $t > 0$, and $g(0) = 0$. Hence, if $\lambda_2 > 0$, the only solution of the equation $f_2 = g(f_2\lambda_2)$ is given by $f_2 = 0$. Consequently, the right-hand side of Eq. (5.27) is identically zero for all $\ell > 0$. In other words, for the simple kernel (5.28), we can rigorously show that the isotropic reference solution is the *only* possible solution. On the basis of physical arguments, we expect—but cannot proof rigorously—that anisotropic solutions do not exist either for kernels with higher-order contributions (with positive amplitudes λ_ℓ).

The results in this section strongly suggest that there must be positional order before there can be orientational ordering in suspensions of Janus or other patchy particles. In other words, we do not expect liquid-crystal phases, and the transition from an isotropic state to a fully ordered crystal phase—if it exists—may well be intermitted by a plastic-crystal phase. Our simple cell model, however, does not take into account the positional correlations of the plastic crystal phase, due to the mean-field nature of the applied boundary conditions at the cell surface.

5.5 Conclusion and outlook

We developed a simple cell model in the context of Poisson-Boltzmann theory for heterogeneously charged colloidal spheres. The boundary conditions—on the colloid surface as well as on the Wigner-Seitz cell surface—depend on the charge heterogeneity and the orientational distribution of the colloidal particles. Within a linear approximation to Poisson-Boltzmann theory, these boundary conditions give rise to a free-energy functional of the orientational distribution function $f(\hat{\omega})$ that is very similar to the one used in Onsager's second-order virial approximation in the description of the isotropic–nematic transition of hard rods [20]. The present description, however, does *not* give rise to orientational ordering. Since our model treats the position of the colloids in a mean-field description—and since we do expect some degree of orientational ordering at sufficiently high particle density—this result suggests that (electrostatics-induced) orientational ordering requires the existence of positional ordering. Therefore, we predict no orientational ordering in fluids of these particles, i.e., no liquid-crystal phases. The present theory, however, is based on a number of

assumptions that must be addressed, and some caution is advised in the interpretation of this result.

First of all, we do not expect that the choice of *linearized* Poisson-Boltzmann theory has a significant effect on our conclusions, although it is known that nonlinear screening affects the long-range orientation dependence of the electrostatic potential around heterogeneously charged colloidal particles (see chapter 3). The reason for this is that our conclusions arise from the boundary conditions on the cell surface. In the case of charge renormalization, this linearization is applied to fit an effective charge which describes the asymptotic behavior correctly. Therefore, all conclusions in this chapter should still hold, when the charge distribution is replaced by an effective (renormalized) one.

Furthermore, in the case of a high surface charge of dipolar character, the conclusion that there is no orientational alignment can be rather counterintuitive. Experimental evidence of this alignment always coincides with the formation of chains [100, 101], with a polarity pointing in the direction along the chain, due to the dipole moment of the constituents. However, such chainlike structures have a strong orientation–position correlation that is not captured by the cell model as formulated here. Our prediction of the absence of liquid-crystal phases in these systems is consistent with the types of phases found in simulations of dipolar particles such as isotropic-fluid, string-fluid, and gel phases at low density, and face-centered-cubic, hexagonal-close-packed, and body-centered-tetragonal solid phases at high density [102]. Indeed, no liquid-crystal phases were found.

Finally, we showed it to be impossible to find solutions that branch off from the (isotropic) reference solution, using bifurcation theory, because this reference solution fails to become unstable. Hypothetically, stable *anisotropic* solutions that do not connect to the (metastable) reference solution might still exist. However, our model belongs to a class of models—investigated by Mulder [99]—for which this type of solution has not been found. Our explicit analysis of the simple case in Sec. 5.4—concerning a charge distribution consisting of a monopole and quadrupole charge only—supports this conclusion.

A potentially serious shortcoming of our model is the mean-field treatment of the colloidal particles. The present model does not include any positional or orientational correlations. The nature of these correlations can be related in a simple way to systems of oppositely charged colloidal particles [103, 104]. The number of bonds between oppositely charged particles in these systems depends on the colloid density. Also, for the dense liquid phase—coexisting with a dilute vapor phase provided the Debye screening length is large enough—the pair distribution function shows that a colloidal particle is surrounded by different layers of colloidal species with alternating signs of charge [103]. The first surrounding layer has an opposite charge with respect to the

particle in the origin; the next layer is like charged and so on. These systems also display multiple crystal structures, which have different coordination number. The same notion can be applied to particles of different orientations to include orientational pair correlations in the cell model.

One could consider to expand the class of Poisson-Boltzmann cell models by incorporating a description of these correlations. More specifically, one can choose a different approach to the way that the surface potential Φ_R is determined. In the present models, this potential is independent of the colloidal species (or orientation) to which the cell belongs. Also, each colloidal species (or orientation) has an equivalent weight—equal to its molar fraction (or value of the ODF)—in the average of the potential and electric field flux at the cell boundary. This property is due to the mean-field description which is used, through the assumption that the surrounding of a particle at the cell boundary is independent from the species it belongs to, or equivalently, its orientation. However, if this restriction is lifted, one may include the fact that the surroundings do depend on this property through the pair distribution function.

Additionally, a jellium approximation can be applied in the same way it is applied to monodisperse systems of homogeneously charged colloidal spheres and rods [105, 106]. In this description, there is no need for a certain cell shape and volume. Moreover, the jellium model has a natural way to include particle pair correlations [107, 108]. Finally, there is an opportunity to apply the Poisson-Boltzmann cell model to nonspherical cells [109]. The boundary conditions can be imposed in the same way as in this chapter. However, this complicates the expression of the appropriate boundary conditions since a nonspherical shape will couple different spherical harmonic modes. The shape of these cells must be controlled by additional constraints such as the minimization of free energy. Also, the choice of shapes must be motivated by physical arguments. We leave these options for future studies.

The work presented in this chapter is also published in the article:
"Poisson-Boltzmann cell model for heterogeneously charged colloids"
Phys. Rev. E, 80:041402, 2009.

Chapter 6

Orientational ordering of heterogeneously charged colloids on a lattice

Abstract

We perform a bifurcation analysis of orientational-symmetry breaking for a certain class of heterogeneously charged colloidal spheres on a simple cubic lattice. At weak coupling—i.e., high temperature, low charge, strong screening, or low density—these particles have an isotropic orientational distribution. We determine the parameter values belonging to critical coupling, for which this isotropic state becomes unstable with respect to orientational ordering.

6.1 Introduction

In the previous chapter, we predicted the absence of orientational ordering of heterogeneously charged spheres in the absence of positional ordering. In the simulation study of Goyal et al. [102], the same conclusion is obtained for a system of colloidal dipoles. In this chapter, we investigate wether orientational ordering is possible for heterogeneously charged spheres that *are* positionally ordered. In addition, we determine the conditions that must be satisfied in order to obtain this orientational ordering and the possible directions of symmetry breaking. This transition is characteristic

for plastic-crystal–ordered-crystal transitions, for which the general idea is that strong isotropic repulsions can cause the system to crystallize at high densities without the need for orientational order. Consequently, the question arises under what conditions the anisotropic screened-Coulomb interactions can drive orientational ordering. We will restrict ourselves here to a bifurcation analysis [43, 99] of a system of particles on a simple cubic lattice. These particles are fixed to their positions, allowing only for a freedom of orientation. We investigate the stability of the orientationally disordered state, that is, to which extent the plastic-crystal phase is stable with respect to an orientationally ordered crystal phase.

6.2 Model

We consider a system of N heterogeneously charged colloidal spheres of radius a on a lattice. Each particle is fixed to a lattice site—such that the center of the sphere and the lattice point coincide—but it has freedom of orientation. We only consider cylindrically symmetric charge distributions, such that the orientation of a particle can be denoted by a unit vector $\hat{\boldsymbol{\omega}}$. The system is immersed in an electrolytic solvent in contact with a salt reservoir of monovalent cations and anions at total concentration $2\rho_\mathrm{s}$. We apply Poisson-Boltzmann theory to this electrolyte. In principle, this means that we must find the (dimensionless) electrostatic potential that obeys the nonlinear second-order partial differential equation

$$\nabla^2\Phi(\mathbf{r}) = \begin{cases} 0 & \exists_i |\mathbf{r}-\mathbf{R}_i| < a, \\ \kappa^2 \sinh\Phi(\mathbf{r}) & \forall_i |\mathbf{r}-\mathbf{R}_i| > a, \end{cases} \tag{6.1}$$

where $\kappa^{-1} = \sqrt{\varepsilon_\mathrm{out}/2\rho_\mathrm{s}\beta e^2}$ is the Debye screening length, in which ε_out is the permittivity of the solvent, $\beta = 1/k_\mathrm{B}T$, and e is the elementary charge; $\{\mathbf{R}_i\}$ denotes the set of lattice points, and it includes the origin. The appropriate boundary conditions on the particle surfaces impose a continuous potential and a discontinuity in the electric field corresponding to the surface charge distributions. These distributions depend on the angle between each particle orientation and the fixed (lattice) frame. In principle, this defines a many-body problem, in which we should consider the thermodynamic limit $N \to \infty$ and therefore an infinite lattice. The entropy due to orientation degrees of freedom has to be taken into account, whereas we ignore translation degrees of freedom because these have no influence on the orientational distribution.

The problem as outlined above is deviously difficult to solve, if not impossible. Therefore, we apply a number of approximations to simplify our calculations. We linearize the Poisson-Boltzmann equation, and approximate the electrostatic energy of the system by pairwise additive interactions $V(\hat{\boldsymbol{\omega}}, \hat{\boldsymbol{\omega}}'; \mathbf{R}-\mathbf{R}')$ between particles at

positions $\mathbf{R}$ and $\mathbf{R}'$, and with orientations $\hat{\omega}$ and $\hat{\omega}'$, respectively. This allows us to express the electrostatic energy of the particle in the origin as a sum of pair interactions over all other lattice positions. In the thermodynamic limit, this expression is independent of the choice of origin, and it therefore represents twice the potential energy per particle. Finally, motivated by the fact that the pair interactions are screened, we truncate this lattice sum to only include a finite range of these interactions. In this chapter, we choose a simple cubic lattice, and include interactions up to a distance of three lattice spacings. We define the free energy (per particle) by

$$\frac{\beta F}{N} = \int \mathrm{d}\hat{\omega} f(\hat{\omega}) \ln\big[4\pi f(\hat{\omega})\big] + \frac{1}{2}\int \mathrm{d}\hat{\omega} f(\hat{\omega}) \int \mathrm{d}\hat{\omega}' f(\hat{\omega}') \sum_{\{\mathbf{R}_i \neq 0\}} \beta V(\hat{\omega}, \hat{\omega}'; \mathbf{R}_i). \tag{6.2}$$

The first contribution is the orientational entropy—where we assume that all particle orientations are described by the same single-particle orientational distribution function (ODF) $f(\hat{\omega})$, which is normalized to unity,

$$\int \mathrm{d}\hat{\omega} f(\hat{\omega}) = 1. \tag{6.3}$$

The second contribution is a sum of all (effective) pair interactions—between a particle at the origin and the particles at all other lattice positions—and averaged over all particle orientations. The orientational average is weighted by the ODF.

Here we give a brief description of the pair interaction and its constituents, of which we give a more detailed picture in appendix C. The pair interaction depends on the heterogeneous surface charge distribution (in units of e), which is expanded in Legendre polynomials, such that

$$\sigma(\hat{\omega}; \hat{\mathbf{n}}) = \sum_{\ell=0}^{\infty} \frac{2\ell+1}{4\pi} \sigma_\ell P_\ell(\hat{\omega} \cdot \hat{\mathbf{n}}). \tag{6.4}$$

We use these "surface multipoles" to define the effective multipole moments of the surface charge distribution (also in units of e)

$$Q_\ell^{\mathrm{eff}} = \frac{\sigma_\ell}{-\kappa^2 \left(\frac{(\varepsilon_{\mathrm{out}} - \varepsilon_{\mathrm{in}})\ell}{\varepsilon_{\mathrm{out}} \kappa a} k_\ell(\kappa a) - k_{\ell+1}(\kappa a) \right)}, \tag{6.5}$$

where $\varepsilon_{\mathrm{in}}$ is the permittivity of the colloidal particle, and k_ℓ are the modified spherical Bessel functions of the second kind. These effective multipoles give rise to screened-

Coulomb interactions of pairs of point multipoles, yielding the following expression:

$$\beta V(\hat{\omega},\hat{\omega}';\mathbf{R}) = 8\pi\kappa l_{\mathrm{B}} \underbrace{\sum_{\ell=0}^{\infty}\sum_{\ell'=0}^{\infty}\sum_{L=0}^{\infty}}_{\ell+\ell'+L\ \text{even}} \frac{(2\ell+1)(2\ell'+1)(2L+1)}{4\pi} \left[\begin{pmatrix} \ell & \ell' & L \\ 0 & 0 & 0 \end{pmatrix}\right]^2 \times (-1)^{\ell'} Q_{\ell}^{\mathrm{eff}} Q_{\ell'}^{\mathrm{eff}} k_L(\kappa R) P_{\ell,\ell',L}(\hat{\omega},\hat{\omega}',\hat{\mathbf{R}}). \quad (6.6)$$

We used the standard notation of the Wigner $3j$-symbols, and introduced the rotational invariants $P_{\ell,\ell',L}$, which correspond to the ordinary Legendre polynomials in the following special cases:

$$P_{\ell,0,\ell}(\hat{\omega},\hat{\omega}',\hat{\mathbf{R}}) = P_{\ell}(\hat{\omega}\cdot\hat{\mathbf{R}}), \quad (6.7)$$

$$P_{\ell,\ell',L}(\hat{\omega},\hat{\mathbf{R}},\hat{\mathbf{R}}) = P_{\ell}(\hat{\omega}\cdot\hat{\mathbf{R}}) \qquad \text{for } \ell+\ell'+L \text{ even}. \quad (6.8)$$

The details of the rotational invariants and the Wigner $3j$-symbols are given in appendix C. Finally, we note that the pair interaction in Eq. (6.6) reduces to the DLVO-potential [38, 39] in the limit of homogeneous charge distributions—for which $\sigma_\ell = \sigma_0\delta_{\ell,0}$. This correspondence includes the associated factor concerning the numerator of the expression in Eq. (6.5) for the effective point charge Q_0^{eff}.

6.3 Bifurcation theory

The ODF that minimizes the free energy in Eq. (6.2), and that obeys the normalization (6.3), is given by the Euler-Lagrange equation

$$f(\hat{\omega}) = \frac{\exp\left[-\int \mathrm{d}\hat{\omega}' f(\hat{\omega}') K(\hat{\omega},\hat{\omega}')\right]}{\int \mathrm{d}\hat{\omega}' \exp\left[-\int \mathrm{d}\hat{\omega}'' f(\hat{\omega}'') K(\hat{\omega}',\hat{\omega}'')\right]}, \quad (6.9)$$

where we define the kernel

$$K(\hat{\omega},\hat{\omega}') \equiv \frac{1}{2}\sum_{\{\mathbf{R}_i\neq 0\}} \Big[\beta V(\hat{\omega},\hat{\omega}';\mathbf{R}_i) + \beta V(\hat{\omega},\hat{\omega}';-\mathbf{R}_i)\Big]. \quad (6.10)$$

We have used the fact that the functional derivative of the second term of the right-hand side of Eq. (6.2)—i.e., the interaction term—operates on both $f(\hat{\omega})$ and $f(\hat{\omega}')$. Since the pair interaction in Eq. (6.6) is not invariant under the interchange of orientations $\hat{\omega}$ and $\hat{\omega}'$, this derivative has two distinct terms, of which one obeys $V(\hat{\omega}',\hat{\omega};\mathbf{R}) = V(\hat{\omega},\hat{\omega}';-\mathbf{R})$. In contrast to the case in chapter 5, this kernel is *not* rotationally invariant, due to the coupling to the underlying lattice. Consequently, the isotropic ODF

$f_{\rm iso}(\hat{\boldsymbol{\omega}}) = 1/4\pi$ is not generally a solution to Eq. (6.9). We first investigate which restrictions should be enforced to obtain such an isotropic solution, since we cannot study isotropic–aligned transitions if there exists no isotropic phase.

Basically, the Euler-Lagrange equation (6.9) yields an isotropic solution if the right-hand side—more specifically, the numerator—does not depend on $\hat{\boldsymbol{\omega}}$ upon inserting the isotropic solution $f_{\rm iso}(\hat{\boldsymbol{\omega}}')$. Using that

$$\frac{1}{4\pi}\int \mathrm{d}\hat{\boldsymbol{\omega}}' K(\hat{\boldsymbol{\omega}},\hat{\boldsymbol{\omega}}') = 4\pi\kappa l_{\rm B} Q_0^{\rm eff} \sum_{\{\mathbf{R}_i\neq 0\}} \sum_{\ell=0}^{\infty} \left[1+(-1)^{\ell}\right] \frac{2\ell+1}{4\pi} Q_\ell^{\rm eff} k_\ell(\kappa R_i) P_\ell(\hat{\boldsymbol{\omega}}\cdot\hat{\mathbf{R}}_i), \tag{6.11}$$

we can identify two cases that allow for the existence of an isotropic distribution. Specifically,

$$\text{(I)}: \qquad Q_0^{\rm eff} = 0; \tag{6.12}$$

$$\text{(II)}: \qquad Q_\ell^{\rm eff} = 0 \qquad \text{for } \ell > 2 \text{ even}. \tag{6.13}$$

Contributions for $\ell = 2$ or ℓ odd vanish because for lattices with cubic symmetry

$$\sum_{\{\mathbf{R}_i\neq 0\}} k_\ell(\kappa R_i) P_\ell(\hat{\boldsymbol{\omega}}\cdot\hat{\mathbf{R}}_i) = 0 \qquad \text{for } \ell \text{ odd or } \ell = 2. \tag{6.14}$$

Therefore, nonzero values of $Q_\ell^{\rm eff}$ for ℓ odd or $\ell = 2$ permit an isotropic solution to the Euler-Lagrange equation (6.9). For simplicity, we only treat charge distributions with contributions up to $\ell = 2$ in this chapter. Thus we assume $Q_\ell^{\rm eff} = 0$ for all values of $\ell > 2$, and we are ensured that an isotropic reference solution exists.

6.3.1 Bifurcation equations

Having established the previous conditions, we now engage in a bifurcation analysis of the system at hand. We expand the ODF as

$$f(\hat{\boldsymbol{\omega}}) \simeq f_{\rm iso} + \varepsilon f_1(\hat{\boldsymbol{\omega}}) + \varepsilon^2 f_2(\hat{\boldsymbol{\omega}}) + \varepsilon^3 f_3(\hat{\boldsymbol{\omega}}), \tag{6.15}$$

where $\int \mathrm{d}\hat{\boldsymbol{\omega}} f_i(\hat{\boldsymbol{\omega}}) = 0$ for $i \geq 1$, due to the normalization of f. This expansion establishes a one-parameter family of solutions that branches off from the isotropic reference solution. We also expand a control parameter

$$\lambda \simeq \lambda_0 + \varepsilon\lambda_1 + \varepsilon^2\lambda_2 + \varepsilon^3\lambda_3. \tag{6.16}$$

We have a limited number of independent dimensionless quantities that we can choose as a control parameter λ: the ratio of the Bjerrum length to the screening length $\kappa l_{\rm B}$;

the charge moments Q_ℓ^{eff} for $\ell = 0, 1, 2$, although $\ell = 0$ has no influence on rotational-symmetry breaking; or the ratio of the cubic lattice constant to the screening length, which influence the sum over all lattice points $\{\mathbf{R}_i \neq 0\}$. We will show that this choice has no influence on the solution of the bifurcation equations. Without specifying the quantity that plays the role of λ for now, we introduce the explicit dependence of the kernel on this control parameter. We obtain the expansion

$$K(\lambda;\hat{\omega},\hat{\omega}') \simeq K_0(\hat{\omega},\hat{\omega}') + \varepsilon K_1(\hat{\omega},\hat{\omega}') + \varepsilon^2 K_2(\hat{\omega},\hat{\omega}') + \varepsilon^3 K_3(\hat{\omega},\hat{\omega}'), \tag{6.17}$$

where

$$K_0(\hat{\omega},\hat{\omega}') = K(\lambda_0;\hat{\omega},\hat{\omega}'), \tag{6.18}$$

$$K_1(\hat{\omega},\hat{\omega}') = \lambda_1 K'(\lambda_0;\hat{\omega},\hat{\omega}'), \tag{6.19}$$

$$K_2(\hat{\omega},\hat{\omega}') = \lambda_2 K'(\lambda_0;\hat{\omega},\hat{\omega}') + \frac{\lambda_1^2}{2} K''(\lambda_0;\hat{\omega},\hat{\omega}'), \tag{6.20}$$

$$K_3(\hat{\omega},\hat{\omega}') = \lambda_3 K'(\lambda_0;\hat{\omega},\hat{\omega}') + \lambda_1\lambda_2 K''(\lambda_0;\hat{\omega},\hat{\omega}') + \frac{\lambda_1^3}{6} K'''(\lambda_0;\hat{\omega},\hat{\omega}'), \tag{6.21}$$

in which the prime denotes a derivative with respect to λ. The bifurcation equations are obtained by inserting the expansions (6.15) and (6.17) into the Euler-Lagrange equation (6.9), and equating terms on both sides for each order in ε. The first, second, and third order yield

$$f_1(\hat{\omega}) = -\frac{1}{4\pi}\int \mathrm{d}\hat{\omega}' f_1(\hat{\omega}') K_0(\hat{\omega},\hat{\omega}'), \tag{6.22}$$

$$\begin{aligned} f_2(\hat{\omega}) = &-\frac{1}{4\pi}\int \mathrm{d}\hat{\omega}' \big[f_2(\hat{\omega}') K_0(\hat{\omega},\hat{\omega}') + f_1(\hat{\omega}') K_1(\hat{\omega},\hat{\omega}')\big] \\ &+ \frac{1}{2}\left\{4\pi\big[f_1(\hat{\omega})\big]^2 - \int \mathrm{d}\hat{\omega}' \big[f_1(\hat{\omega}')\big]^2\right\}, \end{aligned} \tag{6.23}$$

$$\begin{aligned} f_3(\hat{\omega}) = &-\frac{1}{4\pi}\int \mathrm{d}\hat{\omega}' \big[f_3(\hat{\omega}') K_0(\hat{\omega},\hat{\omega}') + f_2(\hat{\omega}') K_1(\hat{\omega},\hat{\omega}') + f_1(\hat{\omega}') K_2(\hat{\omega},\hat{\omega}')\big] \\ &+ 4\pi f_1(\hat{\omega}) f_2(\hat{\omega}) - \int \mathrm{d}\hat{\omega}' f_1(\hat{\omega}') f_2(\hat{\omega}') \\ &- \frac{4\pi}{3}\left\{4\pi\big[f_1(\hat{\omega})\big]^3 - \int \mathrm{d}\hat{\omega}' \big[f_1(\hat{\omega}')\big]^3\right\}, \end{aligned} \tag{6.24}$$

respectively. Usually, Eq. (6.22) is referred to as *the* bifurcation equation. Additionally—assuming that the isotropic solution is stable for small values of λ—the lowest value of λ_0 for which Eq. (6.22) has a solution is called the bifurcation point. We continue our analysis by finding this bifurcation point. To this end, we expand all

functions of the bifurcation equation (6.22) in spherical harmonics. We introduce

$$f_i(\hat{\boldsymbol{\omega}}) = \sum_{\ell,m} f_{\ell,m}^{(i)} Y_{\ell,m}(\hat{\boldsymbol{\omega}}), \tag{6.25}$$

$$K(\lambda;\hat{\boldsymbol{\omega}},\hat{\boldsymbol{\omega}}') = \sum_{\ell,m}\sum_{\ell',m'} K_{\ell,m;\ell',m'}(\lambda) Y_{\ell,m}(\hat{\boldsymbol{\omega}}) Y_{\ell',m'}(\hat{\boldsymbol{\omega}}'), \tag{6.26}$$

where

$$K_{\ell,m;\ell',m'}(\lambda) = 4\pi\kappa l_{\mathrm{B}} \left[(-1)^{\ell} + (-1)^{\ell'}\right] \sqrt{4\pi(2\ell+1)(2\ell'+1)} Q_{\ell}^{\mathrm{eff}} Q_{\ell'}^{\mathrm{eff}}$$
$$\times \sum_{L,M} \sqrt{(2L+1)} \begin{pmatrix} \ell & \ell' & L \\ 0 & 0 & 0 \end{pmatrix} \begin{pmatrix} \ell & \ell' & L \\ m & m' & M \end{pmatrix} \sum_{\{\mathbf{R}_i \neq 0\}} k_L(\kappa R_i) Y_{L,M}(\hat{\mathbf{R}}_i). \tag{6.27}$$

Inserting these expansion into the bifurcation equation (6.22), and using the orthogonality of the spherical harmonics, we find a linear set of equation for the coefficients of f_1,

$$f_{\ell,m}^{(1)} = -\frac{1}{4\pi} \sum_{\ell',m'} K_{\ell,m;\ell',-m'}(\lambda_0) f_{\ell',m'}^{(1)}. \tag{6.28}$$

The explicit form of Eq. (6.27) imposes a number of constraints on possible nonzero (nontrivial) contributions to this set of equations. First of all, the expression of the first line in Eq. (6.27) allows only for the values

$$(\ell,\ell') \in \big\{(0,0),(1,1),(0,2),(2,0),(2,2)\big\}, \tag{6.29}$$

since we assumed $Q_{\ell}^{\mathrm{eff}} = 0$ for $\ell > 2$. Next, the Wigner $3j$-symbols in the second line of the expression ensure that all contributions to the sum over L and M obey $|\ell - \ell'| \leq L \leq \ell + \ell'$, as well as the condition that $\ell + \ell' + L$ is even. Therefore, the values that L assumes—corresponding to the values of ℓ and ℓ' in each instance—are given by:

$$\begin{array}{ll} L = 0 & \text{for } \ell = \ell' = 0, \\ L \in \{0,2\} & \text{for } \ell = \ell' = 1, \\ L = 2 & \text{for } \ell = 0 \text{ and } \ell' = 2, \\ L = 2 & \text{for } \ell = 2 \text{ and } \ell' = 0, \\ L \in \{0,2,4\} & \text{for } \ell = \ell' = 2. \end{array} \tag{6.30}$$

Furthermore, the lattice sum is zero for $L = 2$, because of cubic symmetry. Therefore, the only combinations contributing to the coefficients $K_{\ell,m;\ell',m'}$ are:

$$\ell = \ell' = 0 \text{ and } L = 0, \tag{6.31}$$

$$\ell = \ell' = 1 \text{ and } L = 0, \tag{6.32}$$

$$\ell = \ell' = 2 \text{ and } L \in \{0,4\}. \tag{6.33}$$

Finally, the second Wigner $3j$-symbol imposes the restriction $m+m'+M=0$. Since M must obey $|M| \leq L$, the values of L that belong to nonzero contributions in turn restrict the values of m and m' of the coefficient $K_{\ell,m;\ell',m'}$ that it can contribute to. Moreover, the lattice sum vanishes for $M=2$ or M odd. The combination of these restriction result in a limited number of values that m and m' may assume for nonzero contributions,

$$\left.\begin{array}{ll} m=m'=0 & \text{for } \ell=\ell'=0, \\ m=-m' \in \{-1,0,1\} & \text{for } \ell=\ell'=1, \\ m=-m' \in \{-2,-1,0,1,2\} \text{ or } & \\ m=m' \in \{-2,2\} & \text{for } \ell=\ell'=2. \end{array}\right. \tag{6.34}$$

6.3.2 Solutions

Any solution of the bifurcation equation (6.28) can be written as a set of coefficients $\{f^{(1)}_{\ell,m}\}$, of which at least one is nonzero. When we interpret this set as a vector, and the summation in Eq. (6.28) as matrix multiplication, we need the vector to be an eigenvector of the matrix with coefficients $K_{\ell,m;\ell,-m'}$, and the eigenvalue to be -4π. However, the eigenvalues of this matrix depends on the control parameter λ, and are generally different for distinct values of ℓ. We must find the eigenvectors and corresponding eigenvalues for each value of ℓ. Fortunately, we can easily calculate the coefficients of Eq. (6.27), and cast them into the shape of a matrix $K_\ell(\lambda)$ for each value of $\ell=\ell'$,

$$\big[K_\ell(\lambda)\big]_{m,m'} \equiv -\frac{1}{4\pi} K_{\ell,m;\ell,-m'}(\lambda), \tag{6.35}$$

where m denotes the row number and m' the column number. Using the matrices K_ℓ, we can rewrite the bifurcation equations as matrix equations.

The case for $\ell=0$

Although the combination $\ell=\ell'=0$ has one possible combination of values $m=0$ and $m'=0$,

$$K_0(\lambda) = -2\kappa l_{\mathrm{B}} \big(Q_0^{\mathrm{eff}}\big)^2 \sum_{\{\mathbf{R}_i \neq 0\}} k_0(\kappa R_i), \tag{6.36}$$

a nontrivial solution of the corresponding equation $f^{(1)}_{0,0} = K_0(\lambda_0) f^{(1)}_{0,0}$ does not exist since $K_0(\lambda) < 0$ for all values of λ. Moreover, it is not allowed, since it does not break rotational symmetry, nor does it respect the normalization of f.

The case for $\ell = 1$

In the case where $\ell = \ell' = 1$, there are nine combinations of m and m'—of which three are nonzero—such that

$$K_1(\lambda) = 2\kappa l_{\mathrm{B}} \left(Q_1^{\mathrm{eff}}\right)^2 \sum_{\{\mathbf{R}_i \neq 0\}} k_0(\kappa R_i) \begin{pmatrix} 1 & 0 & 0 \\ 0 & 1 & 0 \\ 0 & 0 & 1 \end{pmatrix}. \tag{6.37}$$

The corresponding bifurcation equation is given by

$$\begin{pmatrix} f_{1,1}^{(1)} \\ f_{1,0}^{(1)} \\ f_{1,-1}^{(1)} \end{pmatrix} = K_1(\lambda_0) \cdot \begin{pmatrix} f_{1,1}^{(1)} \\ f_{1,0}^{(1)} \\ f_{1,-1}^{(1)} \end{pmatrix}, \tag{6.38}$$

where we impose

$$f_{1,1}^{(1)} = -\left(f_{1,-1}^{(1)}\right)^*, \tag{6.39}$$

$$f_{0,0}^{(1)} = \left(f_{0,0}^{(1)}\right)^*, \tag{6.40}$$

because the ODF is real-valued. This yields three linearly independent solutions, each with the same eigenvalue, that we set to one in order to obtain λ_0,

$$2\kappa l_{\mathrm{B}} \left(Q_1^{\mathrm{eff}}\right)^2 \sum_{\{\mathbf{R}_i \neq 0\}} k_0(\kappa R_i) \Bigg|_{\lambda_0} = 1, \tag{6.41}$$

such that

$$K_1(\lambda_0) = \begin{pmatrix} 1 & 0 & 0 \\ 0 & 1 & 0 \\ 0 & 0 & 1 \end{pmatrix}. \tag{6.42}$$

In Sec. 6.4, we will show that the solution for $\ell = 1$ describes magnetic ordering, in which the orientation of all particles tend to align in a single direction. This ordering differs from a "nematic" ordering, in the sense that it does not exhibit up–down symmetry.

The case for $\ell = 2$

For $\ell = \ell' = 2$, the sum over L and M in Eq. (6.27) comprises two contributions: one for $L = 0$, and one for $L = 4$. Each consists of 25 combinations of values for m and m'—of which five are nonzero for the first contribution, and seven are nonzero for the second contribution—yielding

$$K_2(\lambda) = -2\kappa l_{\mathrm{B}} \left(Q_2^{\mathrm{eff}}\right)^2 \sum_{\{\mathbf{R}_i \neq 0\}} k_0(\kappa R_i) \begin{pmatrix} 1 & 0 & 0 & 0 & 0 \\ 0 & 1 & 0 & 0 & 0 \\ 0 & 0 & 1 & 0 & 0 \\ 0 & 0 & 0 & 1 & 0 \\ 0 & 0 & 0 & 0 & 1 \end{pmatrix} - 2\kappa l_{\mathrm{B}} \left(Q_2^{\mathrm{eff}}\right)^2 \sum_{\{\mathbf{R}_i \neq 0\}} k_4(\kappa R_i) P_4(\hat{\mathbf{R}}_i \cdot \hat{\mathbf{z}}) \begin{pmatrix} \frac{3}{7} & 0 & 0 & 0 & \frac{15}{7} \\ 0 & -\frac{12}{7} & 0 & 0 & 0 \\ 0 & 0 & \frac{18}{7} & 0 & 0 \\ 0 & 0 & 0 & -\frac{12}{7} & 0 \\ \frac{15}{7} & 0 & 0 & 0 & \frac{3}{7} \end{pmatrix}, \tag{6.43}$$

where we have simplified the expression of the second contribution by applying the symmetry that belongs to the cubic lattice. Due to this symmetry, we can rewrite the contributions for $m = m' = \pm 2$ by using

$$\sum_{\{\mathbf{R}_i \neq 0\}} k_4(\kappa R_i) Y_{4,\pm 4}(\hat{\mathbf{R}}_i) = 3\sqrt{\frac{10}{\pi}} \sum_{\{\mathbf{R}_i \neq 0\}} k_4(\kappa R_i) P_4(\hat{\mathbf{R}}_i \cdot \hat{\mathbf{z}}). \tag{6.44}$$

The bifurcation equation corresponding to this matrix is given by

$$\begin{pmatrix} f_{2,2}^{(1)} \\ f_{2,1}^{(1)} \\ f_{2,0}^{(1)} \\ f_{2,-1}^{(1)} \\ f_{2,-2}^{(1)} \end{pmatrix} = K_2(\lambda_0) \cdot \begin{pmatrix} f_{2,2}^{(1)} \\ f_{2,1}^{(1)} \\ f_{2,0}^{(1)} \\ f_{2,-1}^{(1)} \\ f_{2,-2}^{(1)} \end{pmatrix}, \tag{6.45}$$

where we impose

$$f_{2,2}^{(1)} = \left(f_{2,-2}^{(1)}\right)^*, \tag{6.46}$$

$$f_{2,1}^{(1)} = -\left(f_{2,-1}^{(1)}\right)^*, \tag{6.47}$$

$$f_{2,0}^{(1)} = \left(f_{2,0}^{(1)}\right)^*, \tag{6.48}$$

again because of the reality of f. In this case there are two distinct eigenvalues. One of these is twofold degenerate, and it is given by

$$-2\kappa l_{\mathrm{B}}\left(Q_2^{\mathrm{eff}}\right)^2 \sum_{\{\mathbf{R}_i\neq 0\}} k_0(\kappa R_i) - \frac{36}{7}\kappa l_{\mathrm{B}}\left(Q_2^{\mathrm{eff}}\right)^2 \sum_{\{\mathbf{R}_i\neq 0\}} k_4(\kappa R_i) P_4(\hat{\mathbf{R}}_i\cdot\hat{\mathbf{z}}). \tag{6.49}$$

This expression is negative or zero for all parameter values. Therefore, there is no value of λ that will yield an eigenvalue equal to 1, and the eigenvectors that correspond to this eigenvalue will not contribute to symmetry breaking. The other eigenvalue is threefold degenerate, and has a possible solution for λ when we set it to 1. This solution is denoted by λ_0, and it is determined by

$$-2\kappa l_{\mathrm{B}}\left(Q_2^{\mathrm{eff}}\right)^2 \sum_{\{\mathbf{R}_i\neq 0\}} k_0(\kappa R_i)\Bigg|_{\lambda_0} + \frac{24}{7}\kappa l_{\mathrm{B}}\left(Q_2^{\mathrm{eff}}\right)^2 \sum_{\{\mathbf{R}_i\neq 0\}} k_4(\kappa R_i) P_4(\hat{\mathbf{R}}_i\cdot\hat{\mathbf{z}})\Bigg|_{\lambda_0} = 1. \tag{6.50}$$

The corresponding eigenvectors are given by

$$\begin{pmatrix} f_{2,2}^{(1)} \\ f_{2,1}^{(1)} \\ 0 \\ f_{2,-1}^{(1)} \\ -f_{2,2}^{(1)} \end{pmatrix}, \tag{6.51}$$

which is composed of three linearly independent contributions. We will denote it as "nematic" ordering, since—in contrast to the solution found for $\ell = 1$—it does exhibit up–down symmetry.

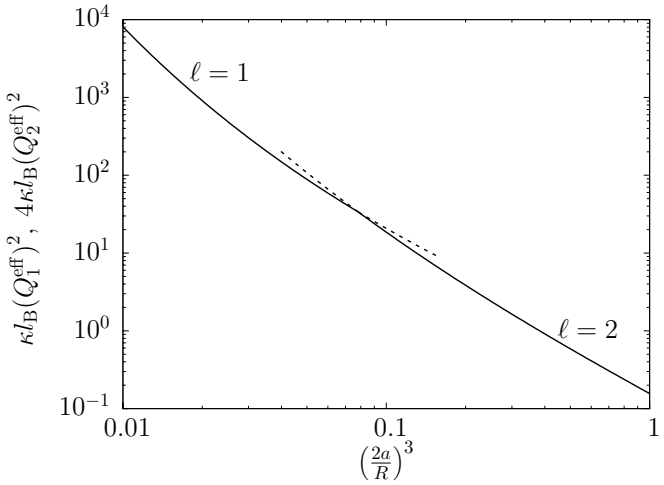

Figure 6.1: Bifurcation diagram for the interaction strength $\kappa l_B \left(Q_1^{\text{eff}}\right)^2$ versus the density $(2a/R)$—scaled with the close-packing density for a simple cubic lattice—for $\kappa a = 1$, where $Q_2^{\text{eff}} = \frac{1}{2} Q_1^{\text{eff}}$ is fixed, and R is the lattice constant. For small values of κl_B—i.e., high temperatures—an isotropic–magnetic ($\ell = 1$) ordering transition takes place upon increasing the density. For larger values, the transition is isotropic–"nematic" ($\ell = 2$).

6.3.3 Results

Evidently, there are two symmetry-breaking solutions: one for $\ell = 1$ and one for $\ell = 2$. Again, if we suppose here that the isotropic reference solution is stable for small values of λ, such that the symmetry breaking occurs upon increasing λ, the solution which sets in first will be the symmetry-breaking solution. We now adopt our description for a given charge distribution by fixing the effective charge moments Q_ℓ^{eff} and varying the temperature through the dimensionless parameter κl_B. On the other hand, we vary the packing fraction through the dimensionless parameter $(2a/R)^3$—which must lie in the range $[0,1]$—where R is the lattice spacing that determines the sum over all lattice points $\{\mathbf{R}_i \neq 0\}$. The parameter $(2a/R)^3$ describes the colloid density scaled with the close-packing density for a simple cubic lattice. Both parameters can be chosen—or interpreted—as the control parameter, but the results do not depend on this choice. Figure 6.1 shows the two curves that describe solutions (6.41) and (6.50) to the bifurcation equation (6.22), where we fixed the ratio between the effective charge moments by setting $Q_2^{\text{eff}} = \frac{1}{2} Q_1^{\text{eff}}$. Upon increasing the density for a certain value of

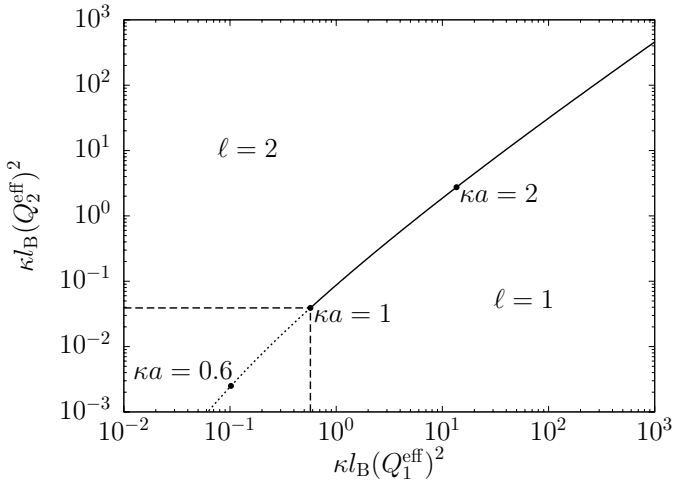

Figure 6.2: Parameter space within which we discern three regions: (I) isotropic–"magnetic" ($\ell = 1$) transitions; (II) isotropic–"nematic" ($\ell = 2$) transitions; (III) no transition—to the lower left of the dashed lines in the case where $\kappa a = 1$.

the interaction strength $\kappa l_{\mathrm{B}}\left(Q_1^{\mathrm{eff}}\right)^2$, one either reaches the curve for $\ell = 1$ first or the one for $\ell = 2$. This determines what solution causes the instability in the isotropic solution, although we cannot establish if the new solution—with lower symmetry—will be stable upon increasing the density further beyond the bifurcation point. For values of $\kappa l_{\mathrm{B}}\left(Q_1^{\mathrm{eff}}\right)^2$ lower than ~ 0.156, there is no bifurcation point, because the density cannot be increased beyond close packing. There is one point where the curves of the two solutions intersect. The values of $\kappa l_{\mathrm{B}}\left(Q_1^{\mathrm{eff}}\right)^2$ and $\kappa l_{\mathrm{B}}\left(Q_2^{\mathrm{eff}}\right)^2$ that belong to this point depend on the ratio between the two effective charge moments, and they are shown in Fig. 6.2 for arbitrary values of this ratio. The solid curve in this diagram gives the collection of these points. It defines the boundary between two regions for which the solutions for $\ell = 1$ or $\ell = 2$ are reached first, respectively. The solid curve is continued by the dotted line beyond the value for which no symmetry breaking occurs—because of close packing—in the case of $\kappa a = 1$. Similar boundary points are shown for $\kappa a = 0.6$ and $\kappa a = 2$. The dashed line determine the boundaries of a region in which neither solutions for $\ell = 1$ or $\ell = 2$ can be reached. Similar lines can be drawn for $\kappa a = 0.6$ and $\kappa a = 2$ parallel to the dashed lines. Within these boundaries, the isotropic solution is stable up to the close-packing density $(2a/R)^3 = 1$.

6.4 Directions of symmetry breaking

In this section we discuss the details of the solution one obtains from the bifurcation equation. If there is rotational-symmetry breaking, the system adopts *cylindrical* symmetry for the particle-orientation distribution with respect to a certain direction. In a rotationally invariant system [99], this direction is arbitrary. However, since we have a coupling to the underlying lattice, this need not be the case in the present study. We therefore investigate what possible directions of symmetry breaking can occur, beginning with the case for $\ell = 2$, because it is much simpler than the case for $\ell = 1$, which we treat secondly.

6.4.1 The case for $\ell = 2$

For notational convenience, we write the solution the bifurcation equation for $\ell = 2$ as

$$f_1(\hat{\omega}) = \mathrm{i}bY_{2,2}(\hat{\omega}) + \alpha Y_{2,1}(\hat{\omega}) - \alpha^* Y_{2,-1}(\hat{\omega}) - \mathrm{i}bY_{2,-2}(\hat{\omega}), \tag{6.52}$$

where α is a complex number and b is a real number. This solution can be expressed by three linearly independent contributions: the real and imaginary parts of α, and b. We will show that combinations of these will give rise to four distinct solutions, each of which describes the alignment along a certain direction $\hat{\mathbf{n}}$, as well as its opposite $(-\hat{\mathbf{n}})$. The functions that describe f_1 have the form of a second order Legendre polynomial $P_2(\hat{\omega}\cdot\hat{\mathbf{n}})$, where $\hat{\mathbf{n}}$ points in one of four directions. These functions are no longer completely independent, and one can be written as minus the sum of the other three. In order to determine these directions, we examine the second-order bifurcation equation (6.23), which we expand in spherical harmonics, such that

$$\begin{aligned} f^{(2)}_{\ell,m} = & -\frac{1}{4\pi}\sum_{\ell',m'}\left[K_{\ell,m;\ell',-m'}(\lambda_0)f^{(2)}_{\ell',m'} + \lambda_1 K'_{\ell,m;\ell',-m'}(\lambda_0)f^{(1)}_{\ell',m'}\right] \\ & + \frac{1}{2}\Bigg\{(-1)^m\sqrt{4\pi(2\ell+1)}\sum_{\ell',m'}\sum_{\ell'',m''}\sqrt{(2\ell'+1)(2\ell''+1)}\begin{pmatrix}\ell & \ell' & \ell''\\ 0 & 0 & 0\end{pmatrix} \\ & \qquad\times\begin{pmatrix}\ell & \ell' & \ell''\\ -m & m' & m''\end{pmatrix}f^{(1)}_{\ell',m'}f^{(1)}_{\ell'',m''} \\ & - \sqrt{4\pi}\delta_{\ell,0}\delta_{m,0}\sum_{\ell',m'}(-1)^{m'}f^{(1)}_{\ell',m'}f^{(1)}_{\ell',-m'}\Bigg\}. \end{aligned} \tag{6.53}$$

The specific case we examine is determined by $\ell = 2$, for which we already established that λ_0 is a solution to Eq. (6.28) for the specific form of f_1 given in Eq. (6.52). A general expression for the $\ell = 2$ contribution to f_2 can be decomposed into a part that

has the same form as f_1 and a part that is orthogonal to f_1—i.e., a decomposition in eigenvectors of the matrix $K_2(\lambda)$. In the same line of reasoning as Mulder [99], we only consider the bifurcation equation (6.53) for components—or linear combinations thereof—that correspond to the eigenfunctions that contribute to f_1. Essentially, we project the second-order bifurcation equation (6.23) onto these specific eigenfunctions instead of the complete set of spherical harmonics, such that: (I) we eliminate its dependence on f_2; (II) we end up with a set of equations for α and b. We cast this set of equations into the convenient form

$$\frac{7\sqrt{30\pi}}{2}\lambda_1 K_2'(\lambda_0)\frac{\alpha+\alpha^*}{2} = -\frac{(\alpha-\alpha^*)b}{2\mathrm{i}}, \tag{6.54}$$

$$\frac{7\sqrt{30\pi}}{2}\lambda_1 K_2'(\lambda_0)\frac{\alpha-\alpha^*}{2\mathrm{i}} = -\frac{(\alpha+\alpha^*)b}{2}, \tag{6.55}$$

$$\frac{7\sqrt{30\pi}}{2}\lambda_1 K_2'(\lambda_0)b = -\frac{(\alpha+\alpha^*)(\alpha-\alpha^*)}{4\mathrm{i}}, \tag{6.56}$$

$$\tag{6.57}$$

where $K_2'(\lambda)$ denotes the derivative—with respect to λ—of the eigenvalue of the matrix $K_2(\lambda)$ corresponding to the solution f_1. The nontrivial—i.e., nonzero—solution to this set of equation yields

$$\left(\frac{\alpha+\alpha^*}{2}\right)^2 = \left(\frac{\alpha-\alpha^*}{2\mathrm{i}}\right)^2 = b^2, \tag{6.58}$$

such that the magnitudes of the real and imaginary parts of α, as well as that of b, are equal. Their signs are either mutually equal or opposite, as long as

$$\frac{7\sqrt{30\pi}}{2}\lambda_1 K_2'(\lambda_0) = -\frac{3(\alpha+\alpha^*)(\alpha-\alpha^*)b}{4\mathrm{i}(\alpha^*\alpha+b^2)}. \tag{6.59}$$

We can now write down the general solution in a form that allows us to use spherical harmonics to determine the direction of symmetry breaking. We rewrite the coefficients of f_1 as:

$$f_{2,2}^{(1)} = \mathrm{i}b = \pm\sqrt{\frac{8\pi}{5}(\alpha^*\alpha+b^2)}\,Y_{2,2}(\theta,\varphi), \tag{6.60}$$

$$f_{2,1}^{(1)} = \alpha = \pm\sqrt{\frac{8\pi}{5}(\alpha^*\alpha+b^2)}\,Y_{2,1}(\theta,\varphi), \tag{6.61}$$

$$f_{2,-1}^{(1)} = -\alpha^* = \pm\sqrt{\frac{8\pi}{5}(\alpha^*\alpha+b^2)}\,Y_{2,-1}(\theta,\varphi), \tag{6.62}$$

$$f_{2,-2}^{(1)} = -\mathrm{i}b = \pm\sqrt{\frac{8\pi}{5}(\alpha^*\alpha+b^2)}\,Y_{2,-2}(\theta,\varphi). \tag{6.63}$$

In this way, we can write the solution as

$$f_1(\hat{\omega}) = \pm\sqrt{\frac{10}{4\pi}\left(\alpha^*\alpha + b^2\right)}\, P_2(\hat{\omega}\cdot\hat{\mathbf{n}}), \tag{6.64}$$

where

$$\hat{\mathbf{n}} = (\sin\theta\cos\varphi, \sin\theta\sin\varphi, \cos\theta). \tag{6.65}$$

This form is in accordance with the reality of b, as well as the restrictions (6.58) if we choose $\varphi \in \{\pi/4, 3\pi/4, 5\pi/4, 7\pi/4\}$ and $\theta \in \{\arccos\sqrt{1/3}, -\arccos\sqrt{1/3}\}$. These directions can be viewed as the orientations of $\hat{\mathbf{n}}$ toward the eight vertices—or corners—of a cube with respect to the center. Pairs of opposite directions are equivalent due to the symmetry of P_2. The sign of f_1 is always opposite to that of the expression $\lambda_1 K_2'(\lambda_0)$, and it therefore depends on the choice of the control parameter λ—and the sign of λ_1—through

$$-\frac{21\sqrt{5\pi}\lambda_1 K_2'(\lambda_0)}{\sqrt{2\left(\alpha^*\alpha + b^2\right)}} = \pm 1. \tag{6.66}$$

6.4.2 The case for $\ell = 1$

In the case where $\ell = 1$, the rotational-symmetry breaking solution can be written as

$$f_1(\hat{\omega}) = \alpha Y_{1,1}(\hat{\omega}) + bY_{1,0}(\hat{\omega}) - \alpha^* Y_{1,-1}(\hat{\omega}), \tag{6.67}$$

where α is again a complex number and b a real number. As mentioned before, this solution introduces a magnetic ordering, for which the particle directions are more or less aligned along a particular direction—i.e., the director. Which direction this is depends on the system parameters, and can be unveiled by examining the higher-order bifurcation equations. The analysis in this part of the section yields the result that the director can have 24 equally probable direction if Q_2^{eff} has a finite value. On the other hand, if $Q_2^{\text{eff}} = 0$, then the particles have no orientational coupling to the underlying lattice, and the director can have an arbitrary orientation. To this end, it is not enough to look at the second-order bifurcation, due to the nature of this particular form of symmetry breaking. We will therefore also examine the third-order bifurcation equation.

To derive our results, we first look again at the second-order bifurcation equation (6.53). We presently focus our attention on the set of equation belonging to $\ell = 1$. As we know from the fact that λ_0 is a solution to Eq. (6.28),

$$f_{1,m}^{(2)} = -\frac{1}{4\pi}\sum_{\ell',m'} K_{1,m;\ell',-m'}(\lambda_0) f_{\ell',m'}^{(2)}, \tag{6.68}$$

for any choice of coefficients $\left\{f^{(2)}_{1,m}\right\}$. This is expressed in Eq. (6.42) by the fact that the matrix $K_1(\lambda_0)$ is equal to the 3×3 identity matrix. Furthermore, the expression in the second term of the right-hand side of Eq. (6.53) yields only a contribution for $\ell = 2$. Therefore, the remaining set of equations is given by

$$-\frac{1}{4\pi}\sum_{\ell',m'}\lambda_1 K'_{\ell,m;\ell',-m'}(\lambda_0) f^{(1)}_{\ell',m'} = 0, \tag{6.69}$$

which only has a trivial solution $\lambda_1 = 0$. The correct way to interpret this solution is that magnetic ordering is a second-order symmetry-breaking transition. We therefore proceed to the third-order bifurcation equation (6.24), which again we expand in spherical harmonics, yielding

$$\begin{aligned}
f^{(3)}_{\ell,m} = &-\frac{1}{4\pi}\sum_{\ell',m'}\left[K_{\ell,m;\ell',-m'}(\lambda_0) f^{(3)}_{\ell',m'} + \lambda_2 K'_{\ell,m;\ell',-m'}(\lambda_0) f^{(1)}_{\ell',m'}\right] \\
&+(-1)^m\sqrt{4\pi(2\ell+1)}\sum_{\ell',m'}\sum_{\ell'',m''}\sqrt{(2\ell'+1)(2\ell''+1)}\begin{pmatrix}\ell & \ell' & \ell''\\ 0 & 0 & 0\end{pmatrix} \\
&\qquad\times\begin{pmatrix}\ell & \ell' & \ell''\\ -m & m' & m''\end{pmatrix} f^{(1)}_{\ell',m'} f^{(2)}_{\ell'',m''} \\
&-\sqrt{4\pi}\,\delta_{\ell,0}\delta_{m,0}\sum_{\ell',m'}(-1)^{m'} f^{(1)}_{\ell',m'} f^{(2)}_{\ell',-m'} \\
&-\frac{1}{3}\Bigg\{(-1)^m\sqrt{4\pi(2\ell+1)}\sum_{\ell',m'}\sum_{\ell'',m''}\sqrt{(2\ell'+1)(2\ell''+1)}\begin{pmatrix}\ell & \ell' & \ell''\\ 0 & 0 & 0\end{pmatrix} \\
&\qquad\times\begin{pmatrix}\ell & \ell' & \ell''\\ -m & m' & m''\end{pmatrix} f^{(1)}_{\ell',m'} \\
&\quad\times(-1)^{m''}\sqrt{4\pi(2\ell''+1)}\sum_{k,n}\sum_{k',n'}\sqrt{(2k+1)(2k'+1)}\begin{pmatrix}\ell'' & k & k'\\ 0 & 0 & 0\end{pmatrix} \\
&\qquad\times\begin{pmatrix}\ell'' & k & k'\\ -m'' & n & n'\end{pmatrix} f^{(1)}_{k,n} f^{(1)}_{k',n'} \\
&\quad-4\pi\delta_{\ell,0}\delta_{m,0}\sum_{k,n}\sum_{k',n'}\sum_{k'',n''}\sqrt{(2k+1)(2k'+1)(2k''+1)}\begin{pmatrix}k & k' & k''\\ 0 & 0 & 0\end{pmatrix} \\
&\qquad\times\begin{pmatrix}k & k' & k''\\ n & n' & n''\end{pmatrix} f^{(1)}_{k,n} f^{(1)}_{k',n'} f^{(1)}_{k'',n''}\Bigg\}.
\end{aligned} \tag{6.70}$$

In order to solve this equation for $\ell = 1$, we need to determine the $\ell = 2$ contribution to f_2 from the second-order bifurcation equation (6.53). The general expression for f_2 is

$$f_2(\hat{\omega}) = \gamma Y_{2,2}(\hat{\omega}) + \delta Y_{2,1}(\hat{\omega}) + g Y_{2,0}(\hat{\omega}) - \delta^* Y_{2,-1}(\hat{\omega}) + \gamma^* Y_{2,-2}(\hat{\omega}) + \tilde{\alpha} Y_{1,1}(\hat{\omega}) + \tilde{b} Y_{1,0}(\hat{\omega}) - \tilde{\alpha}^* Y_{1,-1}(\hat{\omega}), \tag{6.71}$$

where γ, δ, and $\tilde{\alpha}$ are complex constants, whereas g and $\tilde{b}$ are real constants. We can now use Eq. (6.53) for $\ell = 2$ to determine the values its contribution to f_2. Close examination yields the following result:

$$\gamma = \sqrt{\frac{3\pi}{10}} \left(\frac{\alpha^2 + (\alpha^*)^2}{1 + 2A + \frac{36}{7}B} + \frac{\alpha^2 - (\alpha^*)^2}{1 + 2A - \frac{24}{7}B} \right), \tag{6.72}$$

$$\delta = \sqrt{\frac{12\pi}{5}} \frac{\alpha b}{1 + 2A - \frac{24}{7}B}, \tag{6.73}$$

$$g = \sqrt{\frac{4\pi}{5}} \frac{b^2 - \alpha^* \alpha}{1 + 2A + \frac{36}{7}B}, \tag{6.74}$$

where

$$A = \kappa l_{\mathrm{B}} \left(Q_2^{\mathrm{eff}}\right)^2 \sum_{\{\mathbf{R}_i \neq 0\}} k_0(\kappa R_i), \tag{6.75}$$

$$B = \kappa l_{\mathrm{B}} \left(Q_2^{\mathrm{eff}}\right)^2 \sum_{\{\mathbf{R}_i \neq 0\}} k_4(\kappa R_i) P_4(\hat{\mathbf{R}}_i \cdot \hat{\mathbf{z}}). \tag{6.76}$$

We now use these expressions to explicitly write down the $\ell = 1$ case for Eq. (6.53), yielding the set of equations that determine α and b. We use the derivative with respect to λ of the $\ell = 1$ contributions to the kernel. We know that $K_1(\lambda)$ is a diagonal matrix, and therefore, so is its derivative. Moreover, since all coefficients of $K_1(\lambda)$ are equal, again the same holds for its derivative. We need the derivative of this coefficient in the bifurcation point, and we simply denote it by $K_1'(\lambda_0)$. The set of equations from which we determine α and b is given by

$$\lambda_2 K_1'(\lambda_0)\alpha + \frac{2\pi}{5} \left(\frac{-2\alpha b^2 + 5\alpha^* \alpha^2 + 3(\alpha^*)^3}{1 + 2A + \frac{36}{7}B} + \frac{6\alpha b^2 + 3\alpha^* \alpha^2 - 3(\alpha^*)^3}{1 + 2A - \frac{24}{7}B} \right) = \frac{12\pi}{5} \alpha (2\alpha^* \alpha + b^2), \tag{6.77}$$

$$\lambda_2 K_1'(\lambda_0) b + \frac{2\pi}{5}\left(\frac{4b^3 - 4\alpha^*\alpha b}{1+2A+\frac{36}{7}B} + \frac{12\alpha^*\alpha b}{1+2A-\frac{24}{7}B}\right)$$
$$= \frac{12\pi}{5}\left(2\alpha^*\alpha + b^2\right)b, \tag{6.78}$$

$$\lambda_2 K_1'(\lambda_0)\alpha^* + \frac{2\pi}{5}\left(\frac{-2\alpha^* b^2 + 5\left(\alpha^*\right)^2\alpha + 3\alpha^3}{1+2A+\frac{36}{7}B} + \frac{6\alpha^* b^2 + 3\left(\alpha^*\right)^2\alpha - 3\alpha^3}{1+2A-\frac{24}{7}B}\right)$$
$$= \frac{12\pi}{5}\alpha^*\left(2\alpha^*\alpha + b^2\right), \tag{6.79}$$

We multiply both sides of Eqs. (6.77) and (6.79) by α^* and α, respectively, such that we can eliminate all terms linear and quadratic in $\alpha^*\alpha$. We then obtain

$$B\left(\alpha^*\right)^4 = B\alpha^4. \tag{6.80}$$

This imposes a restriction on the value of α, and gives a relation between $\left(\alpha^*\right)^4$, α^4, and $|\alpha|^2 = \alpha^*\alpha$, but only as long as $B \neq 0$,

$$\alpha = \sqrt{\alpha^*\alpha}\exp\left[\frac{\mathrm{i}n\pi}{4}\right], \tag{6.81}$$

$$\alpha^4 = (-1)^n\left(\alpha^*\alpha\right)^2, \tag{6.82}$$

$$\left(\alpha^*\right)^4 = (-1)^n\left(\alpha^*\alpha\right)^2, \tag{6.83}$$

for $n \in \{0,1,2,3,4,5,6,7\}$. We insert the relations (6.82) and (6.83) into Eqs. (6.77) and (6.79), respectively, such that we obtain two identical relations given by the condition

$$\lambda_2 K_1'(\lambda_0) + \frac{2\pi}{5}\left(\frac{-2b^2 + \left[5+3(-1)^n\right]\alpha^*\alpha}{1+2A+\frac{36}{7}B} + \frac{6b^2 + \left[3-3(-1)^n\right]\alpha^*\alpha}{1+2A-\frac{24}{7}B}\right)$$
$$= \frac{12\pi}{5}\left(2\alpha^*\alpha + b^2\right) \text{ or } \alpha^*\alpha = 0. \tag{6.84}$$

Additionally, we rewrite Eq. (6.78) as the condition

$$\lambda_2 K_1'(\lambda_0) + \frac{2\pi}{5}\left(\frac{4b^2 - 4\alpha^*\alpha}{1+2A+\frac{36}{7}B} + \frac{12\alpha^*\alpha}{1+2A-\frac{24}{7}B}\right)$$
$$= \frac{12\pi}{5}\left(2\alpha^*\alpha + b^2\right) \text{ or } b = 0. \tag{6.85}$$

This set of equations yields three possible nontrivial combinations of solutions. First,

$$b = 0 \text{ and } \frac{\lambda_2 K_1'(\lambda_0)}{2\alpha^*\alpha} = \frac{\pi}{5}\left(12 - \frac{5+3(-1)^n}{1+2A+\frac{36}{7}B} - \frac{3-3(-1)^n}{1+2A-\frac{24}{7}B}\right). \tag{6.86}$$

Second,

$$\alpha = 0 \text{ and } \frac{\lambda_2 K_1'(\lambda_0)}{b^2} = \frac{\pi}{5}\left(12 - \frac{8}{1+2A+\frac{36}{7}B}\right). \tag{6.87}$$

Third,

$$b^2 = \frac{3+(-1)^n}{2}\alpha^*\alpha \text{ and} \tag{6.88}$$

$$\frac{\lambda_2 K_1'(\lambda_0)}{2\alpha^*\alpha + b^2} = \frac{\pi}{5}\left(12 - \frac{1+(-1)^n}{1+2A+\frac{36}{7}B} - \frac{7-(-1)^n}{1+2A-\frac{24}{7}B}\right). \tag{6.89}$$

All of these solutions enable us to write down the following expressions for the coefficients of f_1:

$$f_{1,1}^{(1)} = \alpha = \pm\sqrt{\frac{4\pi}{3}\left(2\alpha^*\alpha + b^2\right)}\, Y_{1,1}(\theta,\varphi), \tag{6.90}$$

$$f_{1,0}^{(1)} = b = \pm\sqrt{\frac{4\pi}{3}\left(2\alpha^*\alpha + b^2\right)}\, Y_{1,0}(\theta,\varphi), \tag{6.91}$$

$$f_{1,-1}^{(1)} = -\alpha^* = \pm\sqrt{\frac{4\pi}{3}\left(2\alpha^*\alpha + b^2\right)}\, Y_{1,-1}(\theta,\varphi), \tag{6.92}$$

such that we can write the solution as

$$f_1(\hat{\omega}) = \pm\sqrt{\frac{3}{4\pi}\left(2\alpha^*\alpha + b^2\right)}\, P_1(\hat{\omega}\cdot\hat{\mathbf{n}}), \tag{6.93}$$

where

$$\hat{\mathbf{n}} = (\sin\theta\cos\varphi, \sin\theta\sin\varphi, \cos\theta). \tag{6.94}$$

The restriction (6.81) simply yields $\varphi = n\pi/4$. On the other hand, θ depends on the nature of the solution. Specifically, $b = 0$ implies $\theta = \pi/2$, whereas $\alpha = 0$ corresponds with $\theta \in \{0, \pi\}$. The third possibility is more subtle, and yields $\theta \in \{\pi/4, 3\pi/4\}$ for n even, and $\theta \in \{\arccos\sqrt{1/3}, -\arccos\sqrt{1/3}\}$ for n odd. These directions can be interpreted in the setting of a cube geometry as the orientation of $\hat{\mathbf{n}}$ with respect to its center, toward: the center of the faces for $\theta = \pi/2$ and n even, or $\theta \in \{0, \pi\}$; the center of the edges for $\theta = \pi/2$ and n odd, or $\theta \in \{\pi/4, 3\pi/4\}$ and n even; or the vertices for $\theta \in \{\arccos\sqrt{1/3}, -\arccos\sqrt{1/3}\}$ and n odd. In summary, all directions toward neighboring particles up to $\sqrt{3}$ times the lattice spacing—i.e., crystal orientations [100], [110], or [111]—can be assumed. In contrast to the case for $\ell = 2$, the sign of f_1 does *not* depend on $\lambda_2 K_1'$. Instead, the change of sign in f_1 is equivalent to replacing $\hat{\mathbf{n}}$ with $-\hat{\mathbf{n}}$, due to the anti-symmetry of P_1.

As mentioned earlier, the case where $Q_2^{\text{eff}} = 0$ is special. When applying this case in Eqs. (6.75) and (6.76), we obtain $A = 0$ and $B = 0$, such that

$$\gamma = \sqrt{6\pi}5\alpha^2, \tag{6.95}$$

$$\delta = \sqrt{12\pi}5\alpha b, \tag{6.96}$$

$$g = \sqrt{4\pi}5\big(b^2 - \alpha^*\alpha\big). \tag{6.97}$$

Additionally, the set of equations (6.77)–(6.79) all become identical—for the nontrivial case $f_1 \neq 0$—to

$$\lambda_2 K_1'(\lambda_0) = \frac{4\pi}{5}\big(2\alpha^*\alpha + b^2\big). \tag{6.98}$$

This set therefore imposes no restrictions on the direction $\hat{\mathbf{n}}$. This lack of coupling to the underlying lattice is easily understood by examining the contributing values of L to the sum of particle pair interactions in Eq. (6.6). In this case—where $Q_\ell^{\text{eff}} = 0$ for all $\ell > 1$—all contributions for particles on a cubic lattice have $L = 0$. Therefore, the orientation of the particles with respect to the lattice has no influence on the pair interaction, as $P_{\ell,\ell,0}(\hat{\omega}, \hat{\omega}', \hat{\mathbf{R}}) = P_\ell(\hat{\omega} \cdot \hat{\omega}')$. This pair interaction now results in a kernel that is rotationally invariant.

6.5 Conclusion

In this chapter, we have performed a bifurcation analysis on a model for heterogeneously charged colloidal spheres fixed on a simple cubic lattice. We limited ourselves to cylindrically-symmetric charge distributions that purely consist of a monopole, dipole, and quadrupole contribution. For low densities, or small (effective) dipole or quadrupole moments—as well as for high temperatures—an isotropic particle-orientation distribution exists. Rotational-symmetry breaking occurs for increasing (effective) dipole or quadrupole moments, or for decreasing temperatures. This symmetry breaking also occurs for increasing densities, but only if the pair interaction in strong enough, such that it occurs before close packing densities are reached.

The symmetry-breaking solutions depend on the ratio of the dipole and quadrupole charge. If the quadrupole dominates, the particle-orientation distribution is given by the second-order Legendre polynomial of the angle between the particle orientation and the crystal orientation [111]—i.e., the direction of a neighboring lattice point at a distance of $\sqrt{3}$ times the lattice spacing. There are eight such points, of which opposite pairs are equivalent. If the dipole dominates, the orientational distribution takes the shape of a first-order Legendre polynomial. The direction with respect to which the angle is taken can be any one of the lattice points at distances of 1, $\sqrt{2}$, or $\sqrt{3}$ times the lattice spacing—i.e., crystal orientations [100], [110], or [111].

This work can be extended by considering different lattice structures. Most of the conclusions in this chapter are generally applicable to any lattice with cubic symmetry. It would then be easy to predict which lattice has the lowest free energy in the case of an isotropic orientational distribution, and which kinds of orientational-symmetry breaking may occur. Another worthwhile candidate for extending this work is the application to a binary lattice, for which each set of particles has a distinct orientational distribution, depending on which sublattice its position belongs to. These extensions should be helpful in the understanding of crystal structures of nanoparticles, which often have nonspherical charge distributions.

Appendix A

The pair interaction of two charged rods

The pair interaction of two charged rods is given by Eq. (2.2), where we assume that the electrostatic interaction is determined by integrating over pairs of effective line-charge elements interacting with the screened Coulomb potential. The distance between these pairs is given by a superposition of the relative position of the rods and the combination of the position of the line elements along both rods. Since the integral in Eq. (2.2) cannot be calculated analytically, we try to simplify the calculation. By expanding the integrand in spherical harmonics, we obtain terms that factorize into two functions of the respective positions (using a special case of the expression in Gradshteyn and Ryzhik [110] for imaginary arguments, or the expression in Abramowitz and Stegun [111])

$$\begin{aligned}\frac{\exp[-|\mathbf{r}-\mathbf{s}|]}{|\mathbf{r}-\mathbf{s}|} &= \sum_{\ell=0}^{\infty}(2\ell+1)k_\ell(r)P_\ell(\hat{\mathbf{r}}\cdot\hat{\mathbf{s}})i_\ell(s) \qquad \text{for } r>s,\\ &= 4\pi\sum_{\ell=0}^{\infty}\sum_{m=-\ell}^{+\ell}k_\ell(r)Y_{\ell,m}(\hat{\mathbf{r}})i_\ell(s)Y^*_{\ell,m}(\hat{\mathbf{s}}),\end{aligned} \tag{A.1}$$

where i_ℓ and k_ℓ are the modified spherical Bessel functions of the first and second kind, respectively. These functions are given by

$$i_\ell(x) = \sqrt{\frac{\pi}{2x}} I_{\ell+\frac{1}{2}}(x), \tag{A.2}$$

$$k_\ell(x) = \sqrt{\frac{2}{\pi x}} K_{\ell+\frac{1}{2}}(x), \tag{A.3}$$

where I_ν and K_ν are the modified (cylindrical) Bessel functions of the first and second kind, respectively. The Legendre polynomials P_ℓ are expanded into spherical harmonics $Y_{\ell,m}$ using the famous addition theorem. We use the notation where $r = |\mathbf{r}|$, and $\hat{\mathbf{r}} = \mathbf{r}/r$. Finally, the asterisk "$*$" denotes complex conjugation. The unit vector as given in the arguments of each of the spherical harmonic functions should be interpreted as the two angles in spherical coordinates with respect to an arbitrarily chosen reference frame. Since the Legendre polynomials of the dot product of the two orientations are independent of this choice, so is the sum over m of the product of the two spherical harmonics. The expansion can be understood by the fact that the left-hand side is a Green's function in the case of linear screening and a vanishing potential at infinity. This Green's function can be expanded in Legendre polynomials such that it is the solution of an infinite set of ordinary differential equations instead of one partial differential equation. These equations exactly yield the modified spherical Bessel functions.

We note that one could consider rewriting the expression of the pair potential in rotational invariants (as used in Ref. [67]). These are functions of three orientations, including a sum over m of a product of three spherical harmonic functions multiplied by Clebsch-Gordon coefficients. They form a complete set of orthogonal functions dependent only on the relative orientations of $\hat{\mathbf{r}}$, $\hat{\omega}$, and $\hat{\omega}'$ with respect to each other. However, it turns out that in our case these are not really helpful. Alternatively, one could consider a resummation of the expansion in spherical harmonics, such that each term has a faster asymptotic decay than the previous term. This is not the case here, since each Bessel function k_ℓ has the same asymptotic decay as k_0 [52].

A.1 Domains of integration

The integration over line elements of both rods in Eq. (2.2) is in fact an integration with respect to the vector $l\hat{\omega} - l'\hat{\omega}'$ over a parallelogram-shaped area in the plane tangent to both rod orientations. This area is illustrated in Fig. A.1. There is a straightforward

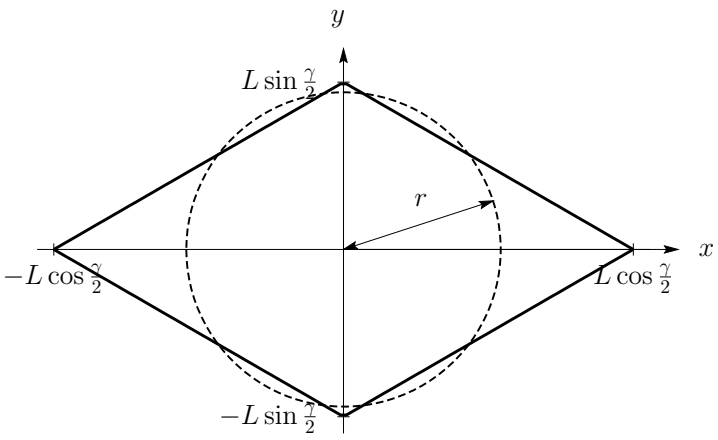

Figure A.1: Illustration of the domain of integration of the superposition of the positions of two line elements. The dashed circle of radius r divides the parallelogram into two domains.

choice for the reference frame and a substitution of variables,

$$\hat{\omega} = \left(\cos\frac{\gamma}{2}, \sin\frac{\gamma}{2}, 0\right), \tag{A.4}$$

$$\hat{\omega}' = \left(\cos\frac{\gamma}{2}, -\sin\frac{\gamma}{2}, 0\right), \tag{A.5}$$

$$l\hat{\omega} - l'\hat{\omega}' = (\rho\cos\varphi, \rho\sin\varphi, 0), \tag{A.6}$$

where γ is the angle between the two rod orientations. The polar coordinates ρ and φ describe the same plane as l and l'. These coordinates—where ρ is multiplied by the inverse screening length κ to make it dimensionless—replace the vector $\mathbf{s}$ in the expansion (A.1). Also, the coordinate r is multiplied by κ. The parallelogram can be cut up into four equivalent pieces, keeping only the terms in the expansion where ℓ and m are both even. The integral boundaries of the first quadrant ($0 \le \varphi \le \pi/2$) satisfy

$$0 \le \rho \le \rho_{\max}(\varphi, \gamma) \equiv \frac{L\sin\gamma}{2\sin\left(\varphi + \frac{\gamma}{2}\right)}. \tag{A.7}$$

It is important to note that the precise form of the expansion of the integrant of Eq. (2.2) can vary as a function of ρ, because k_ℓ and i_ℓ switch roles when $\rho > r$. We shall split the result of our expansion into each order in ℓ and m, to be examined

separately. We write

$$\beta V_{\mathrm{e}}(r,\theta,\phi;\hat{\omega},\hat{\omega}') = \kappa l_{\mathrm{B}}\lambda^2 \underbrace{\sum_{\ell=0}^{\infty}\sum_{m=-\ell}^{+\ell}}_{\ell,m \text{ even}} \frac{(-1)^{\frac{\ell+m}{2}}(2\ell+1)(\ell-m)!}{2^{\ell}\left(\frac{\ell+m}{2}\right)!\left(\frac{\ell-m}{2}\right)!}\mathscr{A}_{\ell,m}(r;\gamma)P_{\ell,m}(\cos\theta)\cos(m\phi), \quad \text{(A.8)}$$

where $P_{\ell,m}$ are the associated Legendre functions. We have used that for ℓ and m both even

$$\frac{Y_{\ell,m}(\theta,\phi)+Y_{\ell,-m}(\theta,\phi)}{2} = \sqrt{\frac{2\ell+1}{4\pi}\frac{(\ell-m)!}{(\ell+m)!}}P_{\ell,m}(\cos\theta)\cos(m\phi), \quad \text{(A.9)}$$

and

$$\left.\frac{Y^*_{\ell,m}(\vartheta,\varphi)+Y^*_{\ell,-m}(\vartheta,\varphi)}{2}\right|_{\vartheta=\frac{\pi}{2}} = (-1)^{\frac{\ell+m}{2}}\sqrt{\frac{2\ell+1}{4\pi}}\frac{\sqrt{(\ell+m)!(\ell-m)!}}{2^{\ell}\left(\frac{\ell+m}{2}\right)!\left(\frac{\ell-m}{2}\right)!}\cos(m\varphi). \quad \text{(A.10)}$$

The expression for $\mathscr{A}_{\ell,m}(r;\gamma)$ in Eq. (A.8) is an integral over the four equivalent quadrants of the product of two modified spherical Bessel functions, together with $\cos(m\varphi)$. It is given by

$$\mathscr{A}_{\ell,m}(r;\gamma) = \frac{4}{\sin\gamma}\int_0^{\frac{\pi}{2}} \mathrm{d}\varphi\,\cos(m\varphi)\mathscr{B}_{\ell}(r;\varphi,\gamma), \quad \text{(A.11)}$$

where

$$\mathscr{B}_{\ell}(r;\varphi,\gamma) = k_{\ell}(\kappa r)\int_0^{\rho_{\max}(\varphi,\gamma)} \mathrm{d}\rho\,\rho\,i_{\ell}(\kappa\rho) \quad \text{(A.12)}$$

for $r > \rho_{\max}(\varphi,\gamma)$, and

$$\mathscr{B}_{\ell}(r;\varphi,\gamma) = k_{\ell}(\kappa r)\int_0^{r} \mathrm{d}\rho\,\rho\,i_{\ell}(\kappa\rho) + i_{\ell}(\kappa r)\int_r^{\rho_{\max}(\varphi,\gamma)} \mathrm{d}\rho\,\rho\,k_{\ell}(\kappa\rho) \quad \text{(A.13)}$$

for $r < \rho_{\max}(\varphi,\gamma)$.

Let us have another look at Fig. A.1. The dashed circle indicates the value for which the variables r and s in Eq. (A.1) switch (in this case r and s are replaced by κr and $\kappa\rho$). Consider the first quadrant (i.e., the upper right-hand corner). Let us also assume $\gamma < \pi/2$, such that $\cos(\gamma/2) > \sin(\gamma/2)$. In the end, we will calculate the effective excluded volume for $0 < \gamma < \pi$, but this expression will turn out to be symmetric in $\gamma \leftrightarrow \pi - \gamma$ (due to up–down symmetry) so we need only to consider the first half of this interval. The integral boundary for ρ is given as a function of φ

by the value of ρ on the boundary of the parallelogram. However, the form of $\mathscr{B}_\ell$ changes when the boundary of the parallelogram intersects with the circle of radius r. Therefore—depending on the value of r—we have one to three domains for $\mathscr{B}_\ell$ as a function of φ

$$\begin{aligned}
&\varphi \in \left[0, \tfrac{\pi}{2}\right] && \text{for } r < \tfrac{L\sin\gamma}{2},\\
&\varphi \in [0,\alpha(r)], [\alpha(r),\beta(r)], \left[\beta(r), \tfrac{\pi}{2}\right] && \text{for } \tfrac{L\sin\gamma}{2} < r < L\sin\tfrac{\gamma}{2},\\
&\varphi \in [0,\alpha(r)], \left[\alpha(r), \tfrac{\pi}{2}\right] && \text{for } L\sin\tfrac{\gamma}{2} < r < L\cos\tfrac{\gamma}{2},\\
&\varphi \in \left[0, \tfrac{\pi}{2}\right] && \text{for } r > L\cos\tfrac{\gamma}{2},
\end{aligned}$$

where

$$\alpha(r) = \arcsin\left(\frac{L\sin\gamma}{2r}\right) - \frac{\gamma}{2}, \tag{A.14}$$

$$\beta(r) = \pi - \arcsin\left(\frac{L\sin\gamma}{2r}\right) - \frac{\gamma}{2} \tag{A.15}$$

are the angles for which the circle intersects the boundary of the parallelogram. For each of the domains (i.e., subsets of $[0,\pi/2]$), there is a corresponding circle segment and a corresponding expression for $\mathscr{B}_\ell$. If the circle segment lies in the interior of the parallelogram, we must distinguish between the interval where ρ is smaller than r and vice versa, and therefore we use Eq. (A.13). When the circle segment of this domain lies outside of the parallelogram, we use Eq. (A.12). Since $\mathscr{A}_{\ell,m}$ contains an integral of φ over the interval $[0,\pi/2]$, we split it into as many pieces as there are domains, using the corresponding expression for the integrant $\mathscr{B}_\ell$ in each domain.

A.2 The limit for parallel rods

In principle, calculations of the effective excluded volume for parallel rods involves the limit $\gamma \to 0$ of Eqs. (A.11)–(A.15). To obtain the correct result, one has to take care to perform the limit correctly in each expression, which is not straightforward. It is much easier to re-evaluate the expressions in this limit analytically, starting with Eqs. (A.4)–(A.6). We use the same reference frame, but a different substitution of variables

$$\hat{\omega} = (1,0,0), \tag{A.16}$$

$$\hat{\omega}' = (1,0,0), \tag{A.17}$$

$$l\hat{\omega} - l'\hat{\omega}' = (\pm x, 0, 0), \tag{A.18}$$

where $x = |l - l'|$. Now the integration is performed over relative positions of two points on a single line. Half of the combinations is positive ($l > l'$), the other half is negative ($l < l'$). The integration boundaries of either set is given by

$$0 \leq x \leq L. \tag{A.19}$$

The length over which each combination l, l' is realized, for a certain value of x, is given by $L - x$. In accordance with the previous expressions, we define the integral $\mathscr{A}_{\ell,m}$ for parallel rods as

$$\mathscr{A}_{\ell,m}(r;\gamma=0) = 2k_\ell(\kappa r)\int_0^L \mathrm{d}x\,(L-x)i_\ell(\kappa x) \tag{A.20}$$

for $r > L$, and

$$\mathscr{A}_{\ell,m}(r;\gamma=0) = 2k_\ell(\kappa r)\int_0^r \mathrm{d}x\,(L-x)i_\ell(\kappa x) + 2i_\ell(\kappa r)\int_r^L \mathrm{d}x\,(L-x)k_\ell(\kappa x) \tag{A.21}$$

for $r < L$. Note that the expressions are independent of m.

A.3 Notations, integrals and Taylor series expansions

In order to calculate the integral $\mathscr{A}_{\ell,m}$, we first need to calculate the integral $\mathscr{B}_\ell$ by performing the integration—with respect to the radial coordinate ρ—in Eqs. (A.12) and (A.13). Because the calculations are rather intricate, we develop here a short-hand notation to allow for relatively compact expressions. Introducing the notation

$$\mathscr{I}_\ell(z) = \int_0^z \mathrm{d}x\,x\,i_\ell(x), \tag{A.22}$$

$$\mathscr{K}_\ell(z) = \int_z^\infty \mathrm{d}x\,x\,k_\ell(x), \tag{A.23}$$

we can rewrite $\mathscr{B}_\ell$ as

$$\kappa^2\mathscr{B}_\ell(r;\varphi,\gamma) = \begin{cases} k_\ell(\kappa r)\mathscr{I}_\ell[\kappa\rho_{\max}(\varphi,\gamma)] & \text{for } r > \rho_{\max}(\varphi,\gamma), \\ k_\ell(\kappa r)\mathscr{I}_\ell(\kappa r) + i_\ell(\kappa r)\mathscr{K}_\ell(\kappa r) & \\ -i_\ell(\kappa r)\mathscr{K}_\ell[\kappa\rho_{\max}(\varphi,\gamma)] & \text{for } r < \rho_{\max}(\varphi,\gamma). \end{cases} \tag{A.24}$$

Unfortunately, there is no (easy) way to write down the expressions in Eqs. (A.22) and (A.23) explicitly for arbitrary ℓ. However, one can give explicit expressions (necessary for our calculations) for $\ell = 0, 2, 4$. First, the modified spherical Bessel functions

$$i_0(z) = \frac{\sinh(z)}{z}, \tag{A.25}$$

$$i_2(z) = \frac{(z^2+3)\sinh(z) - 3z\cosh(z)}{z^3}, \tag{A.26}$$

$$i_4(z) = \frac{(z^4+45z^2+105)\sinh(z) - (10z^3+105z)\cosh(z)}{z^5}, \tag{A.27}$$

$$k_0(z) = \frac{\exp(-z)}{z}, \tag{A.28}$$

$$k_2(z) = \frac{(z^2+3z+3)\exp(-z)}{z^3}, \tag{A.29}$$

$$k_4(z) = \frac{(z^4+10z^3+45z^2+105z+105)\exp(-z)}{z^5}. \tag{A.30}$$

Next, their integrals

$$\mathscr{I}_0(z) = \cosh(z) - 1, \tag{A.31}$$

$$\mathscr{I}_2(z) = \frac{z\cosh(z) - 3\sinh(z)}{z} + 2, \tag{A.32}$$

$$\mathscr{I}_4(z) = \frac{(z^3+35z)\cosh(z) - (10z^2+35)\sinh(z)}{z^3} - \frac{8}{3}, \tag{A.33}$$

$$\mathscr{K}_0(z) = \exp(-z), \tag{A.34}$$

$$\mathscr{K}_2(z) = \frac{(z+3)\exp(-z)}{z}, \tag{A.35}$$

$$\mathscr{K}_4(z) = \frac{(z^3+10z^2+35z+35)\exp(-z)}{z^3}. \tag{A.36}$$

Unfortunately, we cannot perform the subsequent integration—with respect to the angular coordinate φ—in Eq. (A.11) analytically, when we try to calculate $\mathscr{A}_{\ell,m}$. Therefore, we use the series expansions (for even ℓ)

$$\mathscr{I}_{2n}(z) = 2^{2n}\sum_{k=0}^{\infty}\frac{(2n+k)!z^{2n+2k+2}}{(2n+2k+2)(4n+2k+1)!k!}, \tag{A.37}$$

$$\mathscr{K}_{2n}(z) = (-1)^n\frac{(2^n n!)^2}{(2n)!} - \frac{1}{2^{2n}}\sum_{k=1}^{2n}\frac{(-1)^k(2k)!z^{2n-2k+1}}{(2n-2k+1)(2n-k)!k!}$$
$$-\frac{1}{2^{2n}}\sum_{k=0}^{\infty}\frac{k!z^{2n+2k+1}}{(2n+2k+1)(2n+k)!(2k)!} + 2^{2n}\sum_{k=0}^{\infty}\frac{(2n+k)!z^{2n+2k+2}}{(2n+2k+2)(4n+2k+1)!k!}. \tag{A.38}$$

Finally, we define the specific combination

$$\mathscr{C}_\ell(\kappa r) = k_\ell(\kappa r)\mathscr{I}_\ell(\kappa r) + i_\ell(\kappa r)\mathscr{K}_\ell(\kappa r), \tag{A.39}$$

which turns out to be given by a relatively simple expression (for even l),

$$\mathscr{C}_{2n}(\kappa r) = \frac{(n!)^2}{(2n)!}\sum_{k=0}^{n}\frac{(-1)^k(2n+2k)!}{(n+k)!(n-k)!(\kappa r)^{2k+1}} - (-1)^n\frac{(2^n n!)^2}{(2n)!}k_{2n}(\kappa r), \tag{A.40}$$

such that

$$\mathscr{C}_0(z) = \frac{1}{z} - \frac{\exp(-z)}{z}, \tag{A.41}$$

$$\mathscr{C}_2(z) = \frac{z^2-6}{z^3} + 2\frac{(z^2+3z+3)\exp(-z)}{z^3}, \tag{A.42}$$

$$\mathscr{C}_4(z) = \frac{z^4-20z^2+280}{z^5} - \frac{8}{3}\frac{(z^4+10z^3+45z^2+105z+105)\exp(-z)}{z^5}. \tag{A.43}$$

Note that in each expression the first term cancels the divergence of the second term in the limit where $z \to 0$. Hence, this limit is given by

$$\mathscr{C}_{2n}(0) = \delta_{n,0}. \tag{A.44}$$

This property is also reflected in the series expansion—useful for calculations for small κr—given by

$$\mathscr{C}_{2n}(\kappa r) = (-1)^n\frac{(2^n n!)^2}{(2n)!}\frac{\sqrt{\pi}}{2}\sum_{k=0}^{\infty}\frac{1}{\Gamma\left(\frac{k+2n+3}{2}\right)\Gamma\left(\frac{k-2n+2}{2}\right)}\left(\frac{-\kappa r}{2}\right)^k. \tag{A.45}$$

Note that the terms for even $k < 2n$ have vanishing coefficients.

The limit of parallel rods has a different set of expressions. Therefore, we define an additional notation

$$\mathscr{J}_\ell(z) = \int_0^z \mathrm{d}x\,\frac{z-x}{z}\,i_\ell(x), \tag{A.46}$$

$$\mathscr{L}_\ell(z) = \int_z^\infty \mathrm{d}x\,\frac{z-x}{z}\,k_\ell(x). \tag{A.47}$$

In this way, we split each integral in Eq. (A.21) in two parts

$$\kappa^2\mathscr{A}_{\ell,m}(r;\gamma=0) = \begin{cases} 2\kappa L k_\ell(\kappa r)\,\mathscr{J}_\ell(\kappa L) & \text{for } r > L, \\ 2\frac{L-r}{r}\mathscr{C}_\ell(\kappa r) + 2\kappa L k_\ell(\kappa r)\,\mathscr{J}_\ell(\kappa r) & \\ \quad + 2\kappa L\, i_\ell(\kappa r)[\mathscr{L}_\ell(\kappa r) - \mathscr{L}_\ell(\kappa L)] & \text{for } r < L. \end{cases} \tag{A.48}$$

Evaluation of these integrals result in slightly more complicated expressions, when compared to the expressions for $\mathscr{I}$ and $\mathscr{K}$ in Eqs. (A.31)–(A.36),

$$\mathscr{J}_0(z) = \mathrm{shi}(z) + \frac{1}{z} - \frac{\cosh(z)}{z}, \tag{A.49}$$

$$\mathscr{J}_2(z) = -\frac{1}{2}\mathrm{shi}(z) - \frac{2}{z} + \frac{z\cosh(z) + 3\sinh(z)}{2z^2}, \tag{A.50}$$

$$\mathscr{J}_4(z) = \frac{3}{8}\mathrm{shi}(z) + \frac{8}{3z} - \frac{(3z^3+70y)\cosh(z) - (5z^2+70)\sinh(z)}{8z^4}, \tag{A.51}$$

where

$$\mathrm{shi}(z) = \int_0^z \mathrm{d}x \frac{\sinh(x)}{x}, \tag{A.52}$$

is the hyperbolic sine integral.

$$\mathscr{L}_0(z) = \Gamma(0,z) - \frac{\exp(-z)}{z}, \tag{A.53}$$

$$\mathscr{L}_2(z) = -\frac{1}{2}\Gamma(0,z) + \frac{(z-3)\exp(-z)}{2z^2}, \tag{A.54}$$

$$\mathscr{L}_4(z) = \frac{3}{8}\Gamma(0,z) - \frac{(3z^3+5z^2+70y+70)\exp(-z)}{8z^4}. \tag{A.55}$$

One now has the exact solutions for $\mathscr{A}_{\ell,m}$—in the case of parallel rods—up to $\ell = 4$. However, we need the expressions in Eqs. (A.49)–(A.55) to provide a well-defined limit for $\gamma \to 0$, to use in combination with the expressions for arbitrary orientations [i.e., the series expansions in Eqs. (A.37), (A.38), and (A.40)]. Therefore, it will be convenient to also have these expressions in the form of a series expansion,

$$\mathscr{J}_{2n}(z) = 2^{2n} \sum_{k=0}^{\infty} \frac{(2n+k)!\, z^{2n+2k+1}}{(2n+2k+1)(2n+2k+2)(4n+2k+1)!k!}, \tag{A.56}$$

$$\begin{aligned}\mathscr{L}_{2n}(z) = {} & (-1)^n \frac{(2n)!}{(2^n n!)^2}\left(1 + \sum_{k=1}^{2n}\frac{1}{k} - \gamma_{\mathrm{E}} - \ln(z)\right) - (-1)^n \frac{(2^n n!)^2}{(2n)!}\frac{1}{z} \\ & - \frac{1}{2^{2n}} \sum_{k=0,k\neq n}^{2n} \frac{(-1)^k (2k)!\, z^{2n-2k}}{(2n-2k)(2n-2k+1)(2n-k)!k!} \\ & - \frac{1}{2^{2n}} \sum_{k=1}^{\infty} \frac{k!\, z^{2n+2k}}{(2n+2k)(2n+2k+1)(2n+k)!(2k)!} \\ & + 2^{2n} \sum_{k=0}^{\infty} \frac{(2n+k)!\, z^{2n+2k+1}}{(2n+2k+1)(2n+2k+2)(4n+2k+1)!k!}.\end{aligned} \tag{A.57}$$

A.4 Truncation and some examples of expressions

In principle, the calculation of each of the terms in Eq. (A.8) (i.e., each order of ℓ and m) involves an infinite series expansion in κL. We will restrict our calculations to $\ell = 0, 2$, and 4, and truncate each series expansion. Since the shape of the integration domain of $\mathscr{A}_{\ell,m}$ is a parallelogram with sides of length L, we divide out a factor L^2 to make both $\mathscr{A}_{\ell,m}$ and $\mathscr{B}_\ell$ dimensionless [i.e., we calculate $\kappa^2\mathscr{A}_{\ell,m}/(\kappa L)^2$ and $\kappa^2\mathscr{B}_\ell/(\kappa L)^2$]. This factor L^2 is combined with the prefactor $\kappa l_B \lambda^2$ in Eq. (A.8). From the definition of the charge parameter q, we can write the result as an overall prefactor $q\kappa^2 L^2$. The truncated expansion is defined as the expansion up to fourth order in κL of the expression where this prefactor is taken out. This means that we determine the series expansions of the expressions in Eqs. (A.24) and (A.48), after we divide by a factor $(\kappa L)^2$. We give some examples of the calculated expressions for $\ell = 0$ and $m = 0$, where we explicitly make the distinction between four domains in r. For $r < \frac{L\sin\gamma}{2}$,

$$\begin{aligned}
\kappa^2\mathscr{A}_{0,0}(r;\gamma) &= \frac{4}{\sin\gamma}\int_0^{\frac{\pi}{2}} \mathrm{d}\varphi \left\{ \mathscr{C}_0(\kappa r) - i_0(\kappa r)\mathscr{K}_0[\kappa\rho_{\max}(\varphi,\gamma)] \right\} \\
&\simeq \frac{2\pi}{\sin\gamma}\left(\frac{1}{\kappa r} - \frac{\exp(-\kappa r)}{\kappa r} - \frac{\sinh(\kappa r)}{\kappa r}\right) + \frac{\sinh(\kappa r)}{\kappa r}\,\kappa^2 L^2 \\
&\quad \times \left[-\ln\left(\tan\frac{\gamma}{4}\tan\frac{\pi-\gamma}{4}\right)\left(\frac{2}{\kappa L} + \frac{\kappa L\sin^2\gamma}{24} + \frac{\kappa^3 L^3\sin^4\gamma}{2560}\right)\right. \\
&\qquad + \sqrt{1+\sin\gamma}(2-\sin\gamma)\frac{\kappa L}{12} \\
&\qquad + \sqrt{1+\sin\gamma}\left(16 - 8\sin\gamma + 2\sin^2\gamma - 3\sin^3\gamma\right)\frac{\kappa^3 L^3}{3840} \\
&\qquad \left. -1 - \frac{\kappa^2 L^2}{36} - \left(7+5\cos^2\gamma\right)\frac{\kappa^4 L^4}{21600}\right].
\end{aligned} \tag{A.58}$$

The next domain is $\frac{L\sin\gamma}{2} < r < L\sin\frac{\gamma}{2}$, where the expression is a lot more involved, because the integration interval $[0, \pi/2]$ is split into three pieces,

$$
\begin{aligned}
\kappa^2 \mathscr{A}_{0,0}(r;\gamma) = \frac{4}{\sin\gamma}\Bigg\{ & \int_0^{\alpha(\kappa r)} \mathrm{d}\varphi \big\{ \mathscr{C}_0(\kappa r) - i_0(\kappa r)\mathscr{K}_0[\kappa\rho_{\max}(\varphi,\gamma)] \big\} \\
& + \int_{\alpha(\kappa r)}^{\beta(\kappa r)} \mathrm{d}\varphi\, k_0(\kappa r)\mathscr{I}_0[\kappa\rho_{\max}(\varphi,\gamma)] \\
& + \int_{\beta(\kappa r)}^{\frac{\pi}{2}} \mathrm{d}\varphi \big\{ \mathscr{C}_0(\kappa r) - i_0(\kappa r)\mathscr{K}_0[\kappa\rho_{\max}(\varphi,\gamma)] \big\} \Bigg\} \\
\simeq \frac{4}{\sin\gamma}\left(2\arcsin(\xi) - \frac{\pi}{2}\right)\left(\frac{1}{\kappa r} - \frac{\exp(-\kappa r)}{\kappa r} - \frac{\sinh(\kappa r)}{\kappa r}\right) + \frac{\sinh(\kappa r)}{\kappa r}\kappa^2 L^2 & \\
\times \Bigg[-\ln\left(\tan\frac{\gamma}{4}\tan\frac{\pi-\gamma}{4}\right)\left(\frac{2}{\kappa L} + \frac{\kappa L\sin^2\gamma}{24} + \frac{\kappa^3 L^3\sin^4\gamma}{2560}\right) & \\
+ \sqrt{1+\sin\gamma}(2-\sin\gamma)\frac{\kappa L}{12} & \\
+ \sqrt{1+\sin\gamma}\left(16 - 8\sin\gamma + 2\sin^2\gamma - 3\sin^3\gamma\right)\frac{\kappa^3 L^3}{3840} & \\
- 1 - \frac{\kappa^2 L^2}{36} - \left(7 + 5\cos^2\gamma\right)\frac{\kappa^4 L^4}{21600} & \\
- \frac{2r}{L}\operatorname{arctanh}\left(\sqrt{1-\xi^2}\right)\left(\frac{2}{\kappa r} + \xi^2\frac{\kappa r}{6} + \xi^4\frac{\kappa^3 r^3}{160}\right) & \\
- \frac{2r}{L}\sqrt{1-\xi^2}\left(\frac{\kappa r}{6} + (3\xi^2+2)\frac{\kappa^3 r^3}{480}\right. & \\
\left. - 1 - (2\xi^2+1)\frac{\kappa^2 r^2}{36} - (8\xi^4+4\xi^2+3)\frac{\kappa^4 r^4}{5400}\right)\Bigg] & \\
+ \frac{\exp(-\kappa r)}{\kappa r}\kappa^2 L^2\left[\frac{2r}{L}\sqrt{1-\xi^2}\left(1 + (2\xi^2+1)\frac{\kappa^2 r^2}{36} + (8\xi^4+4\xi^2+3)\frac{\kappa^4 r^4}{5400}\right)\right]. &
\end{aligned}
\tag{A.59}
$$

We have abbreviated

$$
\xi = \frac{L\sin\gamma}{2r}. \tag{A.60}
$$

This domain corresponds to the case where the circle of radius r intersects the edge of the parallelogram twice at each quadrant. The following domain corresponds to the case where there is just one intersection per quadrant. Recall that we assume $0 < \gamma < \pi/2$, such that this domain is given by $L\sin\frac{\gamma}{2} < r < L\cos\frac{\gamma}{2}$,

$$
\begin{aligned}
\kappa^2\mathscr{A}_{0,0}(r;\gamma) &= \frac{4}{\sin\gamma}\left\{\int_0^{\alpha(\kappa r)} \mathrm{d}\varphi\left\{\mathscr{C}_0(\kappa r) - i_0(\kappa r)\mathscr{K}_0[\kappa\rho_{\max}(\varphi,\gamma)]\right\}\right. \\
&\qquad \left. + \int_{\alpha(\kappa r)}^{\frac{\pi}{2}} \mathrm{d}\varphi\, k_0(\kappa r)\mathscr{I}_0[\kappa\rho_{\max}(\varphi,\gamma)]\right\} \\
&\simeq \frac{4}{\sin\gamma}\left(\arcsin(\xi) - \frac{\gamma}{2}\right)\left(\frac{1}{\kappa r} - \frac{\exp(-\kappa r)}{\kappa r} - \frac{\sinh(\kappa r)}{\kappa r}\right) + \frac{\sinh(\kappa r)}{\kappa r}\,\kappa^2 L^2 \\
&\times\left[-\ln\left(\tan\frac{\gamma}{4}\right)\left(\frac{2}{\kappa L} + \frac{\kappa L\sin^2\gamma}{24} + \frac{\kappa^3 L^3\sin^4\gamma}{2560}\right) + \left(\frac{1+\cos\gamma}{2}\right)^{\frac{3}{2}}\frac{\kappa L}{6}\right. \\
&\quad + \left(\frac{1+\cos\gamma}{2}\right)^{\frac{5}{2}}(7-3\cos\gamma)\frac{\kappa^3 L^3}{960} - \frac{1+\cos\gamma}{2} \\
&\quad - \left(\frac{1+\cos\gamma}{2}\right)^2(2-\cos\gamma)\frac{\kappa^2 L^2}{36} - \left(\frac{1+\cos\gamma}{2}\right)^3\left(7-6\cos\gamma+2\cos^2\gamma\right)\frac{\kappa^4 L^4}{5400} \\
&\quad - \frac{r}{L}\operatorname{arctanh}\left(\sqrt{1-\xi^2}\right)\left(\frac{2}{\kappa r} + \xi^2\frac{\kappa r}{6} + \xi^4\frac{\kappa^3 r^3}{160}\right) \\
&\quad - \frac{r}{L}\sqrt{1-\xi^2}\left(\frac{\kappa r}{6} + (3\xi^2+2)\frac{\kappa^3 r^3}{480}\right. \\
&\qquad \left.\left. - 1 - (2\xi^2+1)\frac{\kappa^2 r^2}{36} - (8\xi^4+4\xi^2+3)\frac{\kappa^4 r^4}{5400}\right)\right] \\
&+ \frac{\exp(-\kappa r)}{\kappa r}\,\kappa^2 L^2\left[\frac{1-\cos\gamma}{2} + \left(\frac{1-\cos\gamma}{2}\right)^2(2+\cos\gamma)\frac{\kappa^2 L^2}{36}\right. \\
&\qquad + \left(\frac{1-\cos\gamma}{2}\right)^3\left(7+6\cos\gamma+2\cos^2\gamma\right)\frac{\kappa^4 L^4}{5400} \\
&\qquad \left. + \frac{r}{L}\sqrt{1-\xi^2}\left(1 + (2\xi^2+1)\frac{\kappa^2 r^2}{36} + (8\xi^4+4\xi^2+3)\frac{\kappa^4 r^4}{5400}\right)\right].
\end{aligned}
\tag{A.61}
$$

Finally, the domain where $r > L\cos\frac{\gamma}{2}$ yields a more friendly expression,

$$
\begin{aligned}
\kappa^2\mathscr{A}_{0,0}(r;\gamma) &= \frac{4}{\sin\gamma}\int_0^{\frac{\pi}{2}} \mathrm{d}\varphi\, k_0(\kappa r)\mathscr{I}_0[\kappa\rho_{\max}(\varphi,\gamma)] \\
&\simeq \frac{\exp(-\kappa r)}{\kappa r}\,\kappa^2 L^2\left[1 + \frac{\kappa^2 L^2}{36} + \left(7+5\cos^2\gamma\right)\frac{\kappa^4 L^4}{21600}\right].
\end{aligned}
\tag{A.62}
$$

In the case of parallel rods, we can apply the alternative series expansions, or apply the limit $\gamma \to 0$ on the last two expressions above. Both yield the following approximations, where for $r < L$

$$\begin{aligned}
&\kappa^2 \mathscr{A}_{0,0}(r;\gamma=0) \\
&= 2\frac{L-r}{r}\left(\frac{1}{\kappa r} - \frac{\exp(-\kappa r)}{\kappa r}\right) + 2\kappa L \frac{\exp(-\kappa r)}{\kappa r}\left(\mathrm{shi}(\kappa r) + \frac{1}{\kappa r} - \frac{\cosh(\kappa r)}{\kappa r}\right) \\
&\quad + 2\kappa L \frac{\sinh(\kappa r)}{\kappa r}\left(\Gamma(0,\kappa r) - \frac{\exp(-\kappa r)}{\kappa r} - \Gamma(0,\kappa L) + \frac{\exp(-\kappa L)}{\kappa L}\right) \\
&\simeq 2\frac{L-r}{r}\left(\frac{1}{\kappa r} - \frac{\exp(-\kappa r)}{\kappa r}\right) + 2\kappa L \frac{\exp(-\kappa r)}{\kappa r}\frac{\kappa r}{2}\left(1 + \frac{\kappa^2 r^2}{36} + \frac{\kappa^4 r^4}{1800}\right) \\
&\quad + 2\kappa L \frac{\sinh(\kappa r)}{\kappa r}\left[\ln\left(\frac{L}{r}\right) - \frac{1}{\kappa L}\frac{L-r}{r} + \frac{\kappa r}{2}\left(1 - \frac{\kappa r}{6} + \frac{\kappa^2 r^2}{36} - \frac{\kappa^3 r^3}{240} + \frac{\kappa^4 r^4}{1800}\right)\right. \\
&\qquad \left. - \frac{\kappa L}{2}\left(1 - \frac{\kappa L}{6} + \frac{\kappa^2 L^2}{36} - \frac{\kappa^3 L^3}{240} + \frac{\kappa^4 L^4}{1800}\right)\right]. \qquad \text{(A.63)}
\end{aligned}$$

For $r > L$ we obtain

$$\begin{aligned}
\kappa^2 \mathscr{A}_{0,0}(r;\gamma=0) &= 2\kappa L \frac{\exp(-\kappa r)}{\kappa r}\left(\mathrm{shi}(\kappa L) + \frac{1}{\kappa L} - \frac{\cosh(\kappa L)}{\kappa L}\right) \\
&\simeq 2\kappa L \frac{\exp(-\kappa r)}{\kappa r}\frac{\kappa L}{2}\left(1 + \frac{\kappa^2 L^2}{36} + \frac{\kappa^4 L^4}{1800}\right). \qquad \text{(A.64)}
\end{aligned}$$

Likewise, there are expressions for $\ell = 2,4$. These are all used together to create an (approximate) expression for the pair interaction outside of the hard-core exclusion region. We use this pair interaction to numerically calculate the effective excluded volume. This is accomplished by a numerical integration scheme over all different domains of r, for given rod orientations. Our approach is fundamentally different from other theoretical work [51, 52], in the sense that we apply the interchange of the two positional vectors $\mathbf{r}$ and $l\hat{\omega} - l'\hat{\omega}'$. We have to do this in order to calculate the full integral over r, in contrast to the studies in Refs. [51, 52], where only a description is given of the pair interaction for rods at large distances. Conversely, if one considers nonspherical charge distributions on spherical particles, this switch is not needed when introducing rotational invariants.

Appendix B

Derivation of the anisotropic electrostatic potential in a Poisson-Boltzmann cell model

Inside the colloidal particle $\Phi(\hat{\omega};\mathbf{r})$ satisfies the Laplace equation, whereas in the electrolyte it satisfies the LPB equation. Therefore, we have to match two general solutions, using the set of boundary conditions on the particle surface. We do this by expanding both solutions in spherical harmonics. These expressions are given in Eqs. (5.2) and (5.3). We apply the set of boundary conditions on the particle surface given by Eqs. (4.14) and (4.15). To this end, we expand the surface charge distribution in spherical harmonics, using Eq. (5.4) and the addition theorem,

$$\sigma(\hat{\omega};\hat{\mathbf{n}}) = \sum_{\ell=0}^{\infty} \sum_{m=-\ell}^{+\ell} \sigma_\ell Y^*_{\ell,m}(\hat{\omega}) Y_{\ell,m}(\hat{\mathbf{n}}). \tag{B.1}$$

The arguments $\hat{\mathbf{n}}$ and $\hat{\omega}$ of the spherical harmonic function should be interpreted as the pair of spherical angles of this orientation with respect to the reference frame. Consequently, from the boundary conditions (4.14) and (4.15), we obtain the following condition on the coefficients of Φ_{out}:

$$\begin{aligned} &B_{\ell,m}(\hat{\omega}) \left(i'_\ell(\bar{\kappa}a) - \frac{\varepsilon \ell}{\bar{\kappa}a} i_\ell(\bar{\kappa}a) \right) + C_{\ell,m}(\hat{\omega}) \left(k'_\ell(\bar{\kappa}a) - \frac{\varepsilon \ell}{\bar{\kappa}a} k_\ell(\bar{\kappa}a) \right) \\ &= -4\pi l_{\text{B}} \bar{\kappa}^{-1} \sigma_\ell Y^*_{\ell,m}(\hat{\omega}). \end{aligned} \tag{B.2}$$

Next, we apply the boundary conditions at the cell surface given in Eqs. (4.33) and (4.35). This yields a linear system of equations, which can be solved analytically. However, we can choose to split the solution into two contributions. The first contribution then satisfies the boundary conditions on the particle surface—given by Eq. (B.2)—as well as the condition that the potential vanishes at the cell boundary. This is already the relevant boundary condition for all odd contributions to $\Phi(\hat{\omega};\mathbf{r})$, whereas a second contribution must be added later to the even contributions in order to satisfy the full set of boundary conditions. The coefficients that belong to the first contribution will be denoted by $B_{\ell,m}(\hat{\omega})$ and $C_{\ell,m}(\hat{\omega})$. First, we impose the vanishing potential at the cell boundary by

$$B_{\ell,m}(\hat{\omega})i_\ell(\bar{\kappa}R)+C_{\ell,m}(\hat{\omega})k_\ell(\bar{\kappa}R)=0. \tag{B.3}$$

Together with Eq. (B.2), this yields

$$B_{\ell,m}(\hat{\omega}) = -\frac{4\pi l_\mathrm{B}\bar{\kappa}^{-1}\sigma_\ell Y^*_{\ell,m}(\hat{\omega})}{\Xi_\ell(\varepsilon;\bar{\kappa}a,\bar{\kappa}R)}k_\ell(\bar{\kappa}R), \tag{B.4}$$

$$C_{\ell,m}(\hat{\omega}) = \frac{4\pi l_\mathrm{B}\bar{\kappa}^{-1}\sigma_\ell Y^*_{\ell,m}(\hat{\omega})}{\Xi_\ell(\varepsilon;\bar{\kappa}a,\bar{\kappa}R)}i_\ell(\bar{\kappa}R), \tag{B.5}$$

where $\Xi_\ell(\varepsilon;\bar{\kappa}a,\bar{\kappa}R)$ is defined in Eq. (5.6). The orientational dependence of this first contribution is such that it—and therefore all odd contributions—only depends on the angle between $\hat{\omega}$ and $\hat{\mathbf{r}}$,

$$\Phi_\mathrm{odd}(\hat{\omega};\mathbf{r}) = l_\mathrm{B}\bar{\kappa}^{-1}\underbrace{\sum_{\ell=1}^{\infty}}_{\ell\,\mathrm{odd}}(2\ell+1)\sigma_\ell P_\ell(\hat{\omega}\cdot\hat{\mathbf{r}})\frac{k_\ell(\bar{\kappa}r)i_\ell(\bar{\kappa}R)-i_\ell(\bar{\kappa}r)k_\ell(\bar{\kappa}R)}{\Xi_\ell(\varepsilon;\bar{\kappa}a,\bar{\kappa}R)}. \tag{B.6}$$

As previously mentioned, a second contribution must be added to the coefficients of the even contributions. With this contribution included, the solution $\Phi(\hat{\omega};\mathbf{r})$ satisfies the full set of boundary conditions on the cell surface given in Eqs. (4.33) and (4.35). We denote the coefficients of this secondary contribution by $\tilde{B}_{\ell,m}$ and $\tilde{C}_{\ell,m}$. Also, we show that these do not depend on the particle orientation, because the two distinct boundary conditions that govern them do not. First, the boundary condition (B.2) is already satisfied by the coefficients $B_{\ell,m}(\hat{\omega})$ and $C_{\ell,m}(\hat{\omega})$. Therefore,

$$\tilde{B}_{\ell,m}\left(i'_\ell(\bar{\kappa}a)-\frac{\varepsilon\ell}{\bar{\kappa}a}i_\ell(\bar{\kappa}a)\right)+\tilde{C}_{\ell,m}\left(k'_\ell(\bar{\kappa}a)-\frac{\varepsilon\ell}{\bar{\kappa}a}k_\ell(\bar{\kappa}a)\right)=0. \tag{B.7}$$

Second, the boundary condition (4.33) imposes a value on the coefficients that only depends on the value of the potential at the cell surface, which is necessarily independent of the orientation $\hat{\omega}$. Hence,

$$\tilde{B}_{\ell,m}i_\ell(\bar{\kappa}R)+\tilde{C}_{\ell,m}k_\ell(\bar{\kappa}R)=\phi_{\ell,m}, \tag{B.8}$$

where $\phi_{\ell,m}$ is defined by

$$\Phi_R(\hat{\mathbf{n}}) = \Phi_0 - \tanh\Phi_0 + \underbrace{\sum_{\ell=0}^{\infty}}_{\ell \text{ even}} \sum_{m=-\ell}^{+\ell} \phi_{\ell,m} Y_{\ell,m}(\hat{\mathbf{n}}). \tag{B.9}$$

Together, these conditions yield

$$\tilde{B}_{\ell,m} = -\left(k'_\ell(\bar{\kappa}a) - \frac{\varepsilon\ell}{\bar{\kappa}a} k_\ell(\bar{\kappa}a)\right) \frac{\phi_{\ell,m}}{\Xi_\ell(\varepsilon; \bar{\kappa}a, \bar{\kappa}R)}, \tag{B.10}$$

$$\tilde{C}_{\ell,m} = \left(i'_\ell(\bar{\kappa}a) - \frac{\varepsilon\ell}{\bar{\kappa}a} i_\ell(\bar{\kappa}a)\right) \frac{\phi_{\ell,m}}{\Xi_\ell(\varepsilon; \bar{\kappa}a, \bar{\kappa}R)}. \tag{B.11}$$

Finally, the boundary condition (4.35) imposes a vanishing value of the weighted average of the even contributions to the electric field flux at the cell boundary. This condition can be expressed in terms of a relation between the coefficients $B_{\ell,m}$, $C_{\ell,m}$, $\tilde{B}_{\ell,m}$, and $\tilde{C}_{\ell,m}$. By substituting the values given in Eqs. (B.4) and (B.5), we arrive at

$$\begin{aligned} \tilde{B}_{\ell,m} i'_\ell(\bar{\kappa}R) + \tilde{C}_{\ell,m} k'_\ell(\bar{\kappa}R) &= -\int \mathrm{d}\hat{\omega} f(\hat{\omega}) \left[B_{\ell,m}(\hat{\omega}) i'_\ell(\bar{\kappa}R) + C_{\ell,m}(\hat{\omega}) k'_\ell(\bar{\kappa}R)\right] \\ &= \frac{4\pi l_\mathrm{B} \bar{\kappa}^{-1} \sigma_\ell}{\Xi_\ell(\varepsilon; \bar{\kappa}a, \bar{\kappa}R) \bar{\kappa}^2 R^2} \int \mathrm{d}\hat{\omega} f(\hat{\omega}) Y^*_{\ell,m}(\hat{\omega}) \qquad \text{for } \ell \text{ even}, \end{aligned} \tag{B.12}$$

where we used

$$k_\ell(\bar{\kappa}R) i'_\ell(\bar{\kappa}R) - i_\ell(\bar{\kappa}R) k'_\ell(\bar{\kappa}R) = \frac{1}{\bar{\kappa}^2 R^2} \qquad \forall \ell, \tag{B.13}$$

which can be derived from standard identities for the modified spherical Bessel functions. The conditions in Eqs. (B.7) and (B.12) are sufficient to derive similar expressions for $\tilde{B}_{\ell,m}$ and $\tilde{C}_{\ell,m}$. However, the construction we use to derive the solution to the even contributions enables us to show that the cell surface potential $\Phi_R(\hat{\mathbf{n}})$ has the same symmetry properties as the ODF (in addition to the fact that it is composed purely of even contributions),

$$\phi_{\ell,m} = \frac{4\pi l_\mathrm{B} \bar{\kappa}^{-1} \sigma_\ell}{\Lambda_\ell(\varepsilon; \bar{\kappa}a, \bar{\kappa}R) \bar{\kappa}^2 R^2} \int \mathrm{d}\hat{\omega} f(\hat{\omega}) Y^*_{\ell,m}(\hat{\omega}), \tag{B.14}$$

where $\Lambda_\ell(\varepsilon; \bar{\kappa}a, \bar{\kappa}R)$ is defined in Eq. (5.7). With this, we readily obtain the even

contributions

$$\Phi_{\text{even}}(\hat{\omega};\mathbf{r}) = l_{\text{B}}\bar{\kappa}^{-1}\underbrace{\sum_{\ell=0}^{\infty}}_{\ell\text{ even}}\frac{(2\ell+1)\sigma_\ell}{\Xi_\ell(\varepsilon;\bar{\kappa}a,\bar{\kappa}R)}\Big\{\big[k_\ell(\bar{\kappa}r)i_\ell(\bar{\kappa}R)-i_\ell(\bar{\kappa}r)k_\ell(\bar{\kappa}R)\big]P_\ell(\hat{\omega}\cdot\hat{\mathbf{r}}) + \frac{\Xi_\ell(\varepsilon;\bar{\kappa}a,\bar{\kappa}r)}{\Lambda_\ell(\varepsilon;\bar{\kappa}a,\bar{\kappa}R)\bar{\kappa}^2R^2}\int \mathrm{d}\hat{\omega}' f(\hat{\omega}')P_\ell(\hat{\omega}'\cdot\hat{\mathbf{r}})\Big\}, \quad \text{(B.15)}$$

and we obtain the general solution for the dimensionless electrostatic potential in the cell interior given in Eq. (5.5).

Appendix C

The pair interaction
of two heterogeneously charged spheres

Abstract

In this appendix, we give some details concerning the derivation of the pair interaction between two heterogeneously charged colloidal spheres used in chapter 6. This pair interaction is an approximation, which yields the DLVO potential in the limit of homogeneously charged spheres.

C.1 Approximations

The effective pair potential is approximated by applying a first order expansion in terms of induced surface charge on the colloidal particles. First, we calculate the single-particle electrostatic potential around a particle of orientation $\hat{\omega}$—positioned at the origin—within linear Poisson-Boltzmann theory. The result is given by

$$\begin{aligned}\Phi(\mathbf{r}) &= 4\pi\kappa l_{\mathrm{B}} \sum_{\ell=0}^{\infty} \frac{2\ell+1}{4\pi} Q_{\ell}^{\mathrm{eff}} k_{\ell}(\kappa r) P_{\ell}(\hat{\omega}\cdot\hat{\mathbf{r}}) \\ &= 4\pi\kappa l_{\mathrm{B}} \sum_{\ell=0}^{\infty} \sum_{m=-\ell}^{+\ell} Q_{\ell}^{\mathrm{eff}} k_{\ell}(\kappa r) Y_{\ell,m}^{*}(\hat{\omega}) Y_{\ell,m}(\hat{\mathbf{r}}). \end{aligned} \tag{C.1}$$

Then, this potential is evaluated at the surface of a spherical particle of radius a at position $\mathbf{R}$. The way to do this is via a *translation transformation* [112]. First, we

define the position $\mathbf{r}'$ with respect to the center of a sphere at position $\mathbf{R}$ by

$$\mathbf{r} = \mathbf{R} + \mathbf{r}'. \tag{C.2}$$

Then we use the following identity (for $r' < R$)

$$k_\ell(\kappa r) Y_{\ell,m}(\hat{\mathbf{r}}) = \sum_{\ell',m'} \sum_{L,M} (-1)^{\ell'} T^{(\ell,m)}_{\ell',m';L,M} i_{\ell'}(\kappa r') Y_{\ell',m'}(\hat{\mathbf{r}}') k_L(\kappa R) Y_{L,M}(\hat{\mathbf{R}}), \tag{C.3}$$

where we used the translation coefficients

$$\begin{aligned} T^{(\ell,m)}_{\ell',m';L,M} = (-1)^m \sqrt{4\pi(2\ell+1)(2\ell'+1)(2L+1)} \\ \times \begin{pmatrix} \ell & \ell' & L \\ 0 & 0 & 0 \end{pmatrix} \begin{pmatrix} \ell & \ell' & L \\ -m & m' & M \end{pmatrix}, \end{aligned} \tag{C.4}$$

such that

$$\begin{aligned} &\Phi(\mathbf{R}+\mathbf{r}') \\ &= 4\pi\kappa l_{\mathrm{B}} \sum_{\ell,m} \sum_{\ell',m'} \sum_{L,M} (-1)^{\ell'} T^{(\ell,m)}_{\ell',m';L,M} Q^{\mathrm{eff}}_\ell Y^*_{\ell,m}(\hat{\omega}) i_{\ell'}(\kappa r') Y_{\ell',m'}(\hat{\mathbf{r}}') k_L(\kappa R) Y_{L,M}(\hat{\mathbf{R}}). \end{aligned} \tag{C.5}$$

Subsequently, an induced surface charge distribution arises due to the boundary conditions on the sphere surface $r' = a$. These depend on the particle permittivity $\varepsilon_{\mathrm{in}}$ and the fact the the hard core of the particle excludes the presence of ions inside. In appendix B, these boundary conditions are treated in more detail. The induced charge distribution produces an additional potential, and we calculate the (effective) electrostatic energy of a surface charge of a particle with orientation $\hat{\omega}'$ at position $\mathbf{R}$ as a result of the sum of the two potentials. The additional potential is given by

$$\begin{aligned} \tilde{\Phi}(\mathbf{r}') = 4\pi\kappa l_{\mathrm{B}} \sum_{\ell,m} \sum_{\ell',m'} \sum_{L,M} (-1)^{\ell'} T^{(\ell,m)}_{\ell',m';L,M} Q^{\mathrm{eff}}_\ell Y^*_{\ell,m}(\hat{\omega}) \\ \times \frac{\frac{(\varepsilon_{\mathrm{out}}-\varepsilon_{\mathrm{in}})\ell'}{\varepsilon_{\mathrm{out}}\kappa a} i_{\ell'}(\kappa a) + i_{\ell'+1}(\kappa a)}{-\left(\frac{(\varepsilon_{\mathrm{out}}-\varepsilon_{\mathrm{in}})\ell'}{\varepsilon_{\mathrm{out}}\kappa a} k_{\ell'}(\kappa a) - k_{\ell'+1}(\kappa a)\right)} k_{\ell'}(\kappa r') Y_{\ell',m'}(\hat{\mathbf{r}}') k_L(\kappa R) Y_{L,M}(\hat{\mathbf{R}}). \end{aligned} \tag{C.6}$$

Interestingly, the sum of both potential obtains a rather simple form on the sphere surface $\mathbf{r}' = a\hat{\mathbf{n}}$,

$$\begin{aligned} \Phi(\mathbf{R}+a\hat{\mathbf{n}}) + \tilde{\Phi}(a\hat{\mathbf{n}}) = 4\pi\kappa l_{\mathrm{B}} \sum_{\ell,m} \sum_{\ell',m'} \sum_{L,M} (-1)^{\ell'} T^{(\ell,m)}_{\ell',m';L,M} Q^{\mathrm{eff}}_\ell Y^*_{\ell,m}(\hat{\omega}) \\ \times \frac{Y_{\ell',m'}(\hat{\mathbf{n}})}{-\kappa^2 a^2 \left(\frac{(\varepsilon_{\mathrm{out}}-\varepsilon_{\mathrm{in}})\ell'}{\varepsilon_{\mathrm{out}}\kappa a} k_{\ell'}(\kappa a) - k_{\ell'+1}(\kappa a)\right)} k_L(\kappa R) Y_{L,M}(\hat{\mathbf{R}}), \end{aligned} \tag{C.7}$$

since

$$-\left(\frac{(\varepsilon_{\text{out}}-\varepsilon_{\text{in}})\ell}{\varepsilon_{\text{out}}\kappa a}k_\ell(\kappa a)-k_{\ell+1}(\kappa a)\right)i_\ell(\kappa a)$$
$$+\left(\frac{(\varepsilon_{\text{out}}-\varepsilon_{\text{in}})\ell}{\varepsilon_{\text{out}}\kappa a}i_\ell(\kappa a)+i_{\ell+1}(\kappa a)\right)k_\ell(\kappa a)=\frac{1}{\kappa^2a^2}\qquad\forall\ell. \tag{C.8}$$

The integral which determines the electrostatic energy of a given surface charge density in an electrostatic potential arises in linearized Poisson-Boltzmann theory—introduced in Sec. 1.4—as the approximation of the free energy per particle. In certain approximate descriptions—such as this one—the resulting expression can be written as the sum of pair interactions—over all pairs of particles—divided by 2. The electrostatic energy for a surface charge density $\sigma(\hat{\omega}';\hat{\mathbf{n}})$—of a particle with orientation $\hat{\omega}'$—in an electrostatic potential $\Phi+\tilde{\Phi}$ is given by

$$\begin{aligned}
&a^2\int \mathrm{d}\hat{\mathbf{n}}\,\sigma(\hat{\omega}';\hat{\mathbf{n}})\Big[\Phi(\mathbf{R}+a\hat{\mathbf{n}})+\tilde{\Phi}(a\hat{\mathbf{n}})\Big]\\
&=a^2\int \mathrm{d}\hat{\mathbf{n}}\sum_{\lambda,\mu}\sigma_\lambda Y_{\lambda,\mu}(\hat{\omega}')Y^*_{\lambda,\mu}(\hat{\mathbf{n}})\Big[\Phi(\mathbf{R}+a\hat{\mathbf{n}})+\tilde{\Phi}(a\hat{\mathbf{n}})\Big]\\
&=4\pi\kappa l_{\text{B}}\sum_{\ell,m}\sum_{\ell',m'}\sum_{L,M}(-1)^{\ell'}T^{(\ell,m)}_{\ell',m';L,M}Q^{\text{eff}}_\ell Y^*_{\ell,m}(\hat{\omega})\\
&\qquad\times\frac{\sigma_{\ell'}Y_{\ell',m'}(\hat{\omega}')}{-\kappa^2\left(\frac{(\varepsilon_{\text{out}}-\varepsilon_{\text{in}})\ell'}{\varepsilon_{\text{out}}\kappa a}k_{\ell'}(\kappa a)-k_{\ell'+1}(\kappa a)\right)}k_L(\kappa R)Y_{L,M}(\hat{\mathbf{R}})\\
&=4\pi\kappa l_{\text{B}}\sum_{\ell,m}\sum_{\ell',m'}\sum_{L,M}(-1)^{\ell'}T^{(\ell,m)}_{\ell',m';L,M}Q^{\text{eff}}_\ell Y^*_{\ell,m}(\hat{\omega})Q^{\text{eff}}_{\ell'}Y_{\ell',m'}(\hat{\omega}')k_L(\kappa R)Y_{L,M}(\hat{\mathbf{R}}).
\end{aligned}\tag{C.9}$$

Finally, we reverse the approach to calculate the electrostatic energy of the surface charge of the particle with orientation $\hat{\omega}$ in the origin as a result of the combined potential of the particle at position $\mathbf{R}$ and the potential as a result of the induced charge at the surface of the particle in the origin. The two results are equal, and thus both are equal to half of the pair interaction (6.6), which we write here as

$$\begin{aligned}
\beta V(\hat{\omega},\hat{\omega}';\mathbf{R})=8\pi\kappa l_{\text{B}}\sum_{\ell,m}\sum_{\ell',m'}\sum_{L,M}\sqrt{4\pi(2\ell+1)(2\ell'+1)(2L+1)}\begin{pmatrix}\ell&\ell'&L\\0&0&0\end{pmatrix}\\
\times\begin{pmatrix}\ell&\ell'&L\\m&m'&M\end{pmatrix}(-1)^{\ell'}Q^{\text{eff}}_\ell Q^{\text{eff}}_{\ell'}k_L(\kappa R)Y_{\ell,m}(\hat{\omega})Y_{\ell',m'}(\hat{\omega}')Y_{L,M}(\hat{\mathbf{R}}).
\end{aligned}\tag{C.10}$$

C.2 Rotational invariants

In chapter 6, we used the functions

$$P_{\ell,\ell',L}(\hat{\omega},\hat{\omega}',\hat{\mathbf{R}}) = (-1)^{\frac{\ell+\ell'+L}{2}}\sqrt{\frac{(4\pi)^3}{(2\ell+1)(2\ell'+1)(2L+1)}} \times\sqrt{\frac{(-\ell+\ell'+L)!!(\ell-\ell'+L)!!(\ell+\ell'-L)!!(\ell+\ell'+L+1)!!}{(-\ell+\ell'+L-1)!!(\ell-\ell'+L-1)!!(\ell+\ell'-L-1)!!(\ell+\ell'+L)!!}} \times\sum_{m=-\ell}^{+\ell}\sum_{m'=-\ell'}^{+\ell'}\sum_{M=-L}^{+L}\begin{pmatrix}\ell & \ell' & L\\ m & m' & M\end{pmatrix}Y_{\ell,m}(\hat{\omega})Y_{\ell',m'}(\hat{\omega}')Y_{L,M}(\hat{\mathbf{R}}), \quad \text{(C.11)}$$

in the expression of the pair potential in Eq. (6.6). We designated these functions as rotational invariants, since they form a complete orthogonal set of rotationally invariant functions of the orientations $\hat{\omega}$, $\hat{\omega}'$, and $\hat{\mathbf{R}}$. In contrast to the Legendre polynomial—wich are functions of the relative orientation of two vectors (i.e., one dot product)—the rotational invariants are functions of the relative orientation of three vectors (i.e., three dot products). The fact that the series in Eq. (6.6) only has nonzero contributions for $\ell+\ell'+L$ even, is due to the dependence of this function on the *dot products* of the orientations, whereas a more general function of the relative *angles* between the three orientation would include contributions of rotational invariants with $\ell+\ell'+L$ odd. Some examples of these functions are

$$P_{0,0,0}(\hat{\omega},\hat{\omega}',\hat{\mathbf{R}}) = 1,$$

$$P_{1,1,0}(\hat{\omega},\hat{\omega}',\hat{\mathbf{R}}) = \hat{\omega}\cdot\hat{\omega}',\quad P_{1,0,1}(\hat{\omega},\hat{\omega}',\hat{\mathbf{R}}) = \hat{\omega}\cdot\hat{\mathbf{R}},\quad P_{0,1,1}(\hat{\omega},\hat{\omega}',\hat{\mathbf{R}}) = \hat{\omega}'\cdot\hat{\mathbf{R}},$$

$$P_{2,2,0}(\hat{\omega},\hat{\omega}',\hat{\mathbf{R}}) = \frac{3(\hat{\omega}\cdot\hat{\omega}')^2-1}{2},\quad P_{1,1,2}(\hat{\omega},\hat{\omega}',\hat{\mathbf{R}}) = \frac{3(\hat{\omega}\cdot\hat{\mathbf{R}})(\hat{\omega}'\cdot\hat{\mathbf{R}})-\hat{\omega}\cdot\hat{\omega}'}{2},$$

$$P_{2,0,2}(\hat{\omega},\hat{\omega}',\hat{\mathbf{R}}) = \frac{3(\hat{\omega}\cdot\hat{\mathbf{R}})^2-1}{2},\quad P_{1,2,1}(\hat{\omega},\hat{\omega}',\hat{\mathbf{R}}) = \frac{3(\hat{\omega}\cdot\hat{\omega}')(\hat{\omega}'\cdot\hat{\mathbf{R}})-\hat{\omega}\cdot\hat{\mathbf{R}}}{2},$$

$$P_{0,2,2}(\hat{\omega},\hat{\omega}',\hat{\mathbf{R}}) = \frac{3(\hat{\omega}'\cdot\hat{\mathbf{R}})^2-1}{2},\quad P_{2,1,1}(\hat{\omega},\hat{\omega}',\hat{\mathbf{R}}) = \frac{3(\hat{\omega}\cdot\hat{\omega}')(\hat{\omega}\cdot\hat{\mathbf{R}})-\hat{\omega}'\cdot\hat{\mathbf{R}}}{2},$$

$$P_{2,2,2}(\hat{\omega},\hat{\omega}',\hat{\mathbf{R}}) = \frac{9(\hat{\omega}\cdot\hat{\omega}')(\hat{\omega}\cdot\hat{\mathbf{R}})(\hat{\omega}'\cdot\hat{\mathbf{R}})-3(\hat{\omega}\cdot\hat{\omega}')^2-3(\hat{\omega}\cdot\hat{\mathbf{R}})^2-3(\hat{\omega}'\cdot\hat{\mathbf{R}})^2+2}{2}.$$

C.3 Wigner 3j-symbols

The Wigner 3j-symbols

$$\begin{pmatrix} \ell & \ell' & L \\ 0 & 0 & 0 \end{pmatrix} \quad \text{and} \quad \begin{pmatrix} \ell & \ell' & L \\ m & m' & M \end{pmatrix} \tag{C.12}$$

are essentially defined by the same expression. The only difference is that the first is characterized by $m = m' = M = 0$, and it therefore is given by the (relatively) simple expression

$$\begin{pmatrix} \ell & \ell' & L \\ 0 & 0 & 0 \end{pmatrix} = \begin{cases} (-1)^{\frac{\ell+\ell'+L}{2}} \sqrt{\frac{(-\ell+\ell'+L-1)!!(\ell-\ell'+L-1)!!(\ell+\ell'-L-1)!!(\ell+\ell'+L)!!}{(-\ell+\ell'+L)!!(\ell-\ell'+L)!!(\ell+\ell'-L)!!(\ell+\ell'+L+1)!!}} & \text{for } \ell+\ell'+L \text{ even}, \\ 0 & \text{for } \ell+\ell'+L \text{ odd}. \end{cases} \tag{C.13}$$

Furthermore, the Wigner 3j-symbols are more gerally connected to the Clebsch-Gordon coefficients—used in the addition of angular momentum in quantum mechanics—by

$$\langle j_1, j_2; m_1, m_2 | j_1, j_2; j, m \rangle = (-1)^{j_1 - j_2 + m} \sqrt{2j+1} \begin{pmatrix} j_1 & j_2 & j \\ m_1 & m_2 & -m \end{pmatrix}. \tag{C.14}$$

Finally, the combination of the two can be obtained by the identity

$$\begin{aligned} &4\pi \int \mathrm{d}\hat{\omega} Y_{\ell,m}(\hat{\omega}) Y_{\ell',m'}(\hat{\omega}) Y_{L,M}(\hat{\omega}) \\ &= \sqrt{4\pi(2\ell+1)(2\ell'+1)(2L+1)} \begin{pmatrix} \ell & \ell' & L \\ 0 & 0 & 0 \end{pmatrix} \begin{pmatrix} \ell & \ell' & L \\ m & m' & M \end{pmatrix}. \end{aligned} \tag{C.15}$$

Summary

As the title suggests, this thesis studies orientational ordering of charged colloidal particles. This orientational behavior appears in colloidal suspensions if the particles in it are not spherically symmetric. Generally, this is the case—even if the synthesis of such a suspension was performed carefully to make the particles as spherical as possible. The nonspherical aspects of colloidal particles can be either due to shape or to chemical surface properties—that is, patterning. The question we address is: when do such nonspherical properties become important in the collective behavior of colloidal particles?

To answer this question, we theoretically investigate the equilibrium properties of charged colloidal particles. We have chosen the subject of charge particles for three reasons. First, electrostatic effects are generally present in colloidal suspensions. Second, there were—and still are—a great deal of opportunities in this field to answer existing questions or raise new ones. Third, the effective interactions between charged colloidal particles are relatively easy to describe or approximate. The restriction to equilibrium properties of the systems of interest refers to the lack of dynamics in our descriptions. In the end, we hope to describe collective properties that can be obtained through the equilibration of a system. In other words, we like a suspension to build its own structure through thermodynamic relaxation. The question whether these structures are kinetically accessible remains to be answered.

The way we treat particle orientations is through *orientational distributions*. Analogous to particle-position distributions, we find configurations that minimize the free energy—thereby predicting the equilibrium state. We distinguish four types of phases that describe equilibrium configurations: isotropic fluid, liquid crystal, plastic crystal,

and aligned crystal. The isotropic-fluid phase is characterized by a lack of both positional and orientational ordering. Fluids that display orientational ordering but no (complete) positional ordering are denoted liquid crystals. Conversely, in the case of a plastic crystal there is complete positional ordering but no orientational ordering. The aligned-crystal phase exhibits both orientational and positional ordering. Following the teachings of Lars Onsager, we view particles of different orientation as particles belonging to different species. A change in orientation can be viewed as an exchange of particles of different species: one leaves the system to make room for the other. Such a description is easily implemented in a grand-canonical ensemble to find the most favorable distribution of particle orientations in a system. In this thesis, we apply the description to systems of colloidal particles that are either rodlike in shape and homogeneously charged, or heterogeneously charged and spherical. In both cases, the charge distribution is decomposed in multipole moments. To this end we apply expansions in spherical harmonics to all orientation-dependent functions.

In chapter 2, we treat the phase behavior of short charged rods. We compute the orientation-dependent second virial coefficient, which we compare with the case of *uncharged* rods. From this comparison, we construct a mapping onto systems of hard rods with *effective dimensions*. The liquid-crystal phases that are predicted in these systems are no longer present for rods of sufficiently high charge, because their interactions are essentially isotropic.

Chapter 3 is based on a *charge renormalization* scheme, which defines a relation between the nonlinear and linearized descriptions of electrostatic interactions between charged colloidal particles. The renormalized charge belongs to the linearized description that has the same behavior at large distances as the nonlinear description for the actual charge. This scheme is traditionally applied to spherical particles with homogeneous surface charge, but we apply it to colloidal spheres of *heterogeneous* surface charge. One of our main conclusions is that the total renormalized charge depends not only on the total actual charge, but also on its distribution on the particle surface.

Finally, we present two models in which we apply bifurcation theory to a linearized description for heterogeneously charged spheres. In chapter 4 we introduce a cell model, which is formulated as an extension of the cell model for mixtures of homogenously charged spheres. We employ this model in chapter 5 to describe fluid phases, as it lacks any positional ordering of the colloidal particles. The second model is treated in chapter 6 and puts the particles on a fixed lattice, which characterizes the positional ordering in solids. In both cases we investigate the possibility of an isotropic-to-aligned transition of the orientational distribution. In the fluid phase we find none, whereas the solid phase exhibits two possible transitions—depending on the values of the system parameters. In one case the resulting orientational distribution has up–down symmetry, in the other case it does not.

Samenvatting

Zoals de titel doet vermoeden gaat dit proefschrift over oriëntationele ordening van geladen colloïdale deeltjes. Dat gedrag is te zien in suspensies van niet-bolsymmetrische deeltjes. Dit is vaak het geval – zelfs als de makers van zo'n suspensie hun best hebben gedaan om de deeltjes zo bolvormig mogelijk te maken. Het niet-bolvormige aspect van colloïdale deeltjes kan liggen in hun vorm of in de chemische oppervlakte-eigenschappen (d.w.z. patronen). Nu is de vraag: wanneer worden zulke niet-bolvormige eigenschappen belangrijk voor het gezamenlijke gedrag van colloïdale deeltjes?

Om een antwoord op deze vraag te vinden, doen we theoretisch onderzoek naar de eigenschappen van geladen colloïdale suspensies in evenwicht. We hebben gekozen voor de studie van geladen deeltjes om drie redenen. Ten eerste, elektrostatische effecten komen veel voor in colloïdale suspensies. Ten tweede, er waren – en zijn nog steeds – veel mogelijkheden om in dit onderzoeksgebied bestaande vragen te beantwoorden en nieuwe te formuleren. Ten derde, de effectieve interacties tussen geladen colloïden zijn relatief eenvoudig te beschrijven of te benaderen. We beperken ons tot de evenwichtseigenschappen door een statistische beschrijving te geven waarin dynamica geen rol speelt. Uiteindelijke hopen we gezamenlijke eigenschappen te beschrijven die verkregen kunnen worden door een systeem in evenwicht te brengen. We eisen dus dat een systeem zijn eigen structuur aanlegt door middel van thermodynamische relaxatie. De vraag of deze structuren kinetisch toegankelijk zijn blijft dan onbeantwoord.

De manier waarop we de oriëntatie van deeltjes behandelen is als *oriëntatieverdeling*. Analoog aan de positieverdeling bepalen we configuraties behorend bij een minimum in de vrije energie – dit is dan de evenwichtstoestand. We onderschei-

den vier soorten fasen die een evenwichtstoestand beschrijven: isotrope vloeistof, vloeibaar kristal, plastic kristal en opgelijnd kristal. De isotrope vloeistof wordt gekarakteriseerd door een gebrek aan zowel positionele als oriëntationele ordening. Vloeistoffen waarin oriëntationele ordening optreedt, maar geen (of gedeeltelijke) positionele ordening, noemt men vloeibare kristallen. In het geval van een plastic kristal is er daarentegen sprake van volledige positionele ordening, maar geen oriëntationele ordening. Opgelijnde kristallen bezitten zowel positionele als oriëntationele ordening. Volgens de leer van Lars Onsager kunnen we deeltjes met verschillende oriëntatie beschouwen als deeltjes van verschillende soorten. Een verandering van oriëntatie kan dan worden beschouwd als een uitwisseling van deeltjes van verschillende soorten: de één maakt plaats voor de ander. Zo'n beschrijving is eenvoudig te implementeren in een grootcanoniek ensemble, waarbij we de meest gunstige verdeling van deeltjesoriëntaties bepalen. In dit proefschrift passen we de beschrijving toe op colloïden die óf staafvormig zijn en homogeen geladen, óf heterogeen geladen en bolvormig. In beide gevallen ontbinden we de ladingsverdeling in multipoolmomenten. Daartoe expanderen we alle oriëntatie-afhankelijke functies in bolfuncties.

In hoofdstuk 2 behandelen we korte geladen staafjes. We berekenen de oriëntatieafhankelijke tweede viriaalcoëfficient en vergelijken deze met het geval voor *ongeladen* staafjes. Uit deze vergelijking stellen we een afbeelding op naar systemen van harde staafjes met *effectieve afmetingen*. De vloeibaarkristallijne fasen die voorspeld worden voor deze systemen zijn niet meer aanwezig voor hooggeladen staafjes, omdat hun interacties eigenlijk isotroop zijn.

Hoofdstuk 3 is gebaseerd op de techniek genaamd *ladingsrenormalisatie*, waarin een koppeling gemaakt wordt tussen de niet-lineaire en gelineariseerde beschrijvingen van ladingsinteractie tussen colloïdale deeltjes. De gerenormaliseerde lading hoort bij de gelineariseerde beschrijving waarvan het gedrag op grote afstanden hetzelfde is als de niet-lineaire beschrijving voor de echte lading. Deze techniek wordt normaliter toegepast op bolvormige deeltjes met een homogene oppervlaktelading, maar wij passen hem toe op bolvormige deeltjes met een *heterogene* oppervlaktelading. Eén van de belangrijkste conclusies is dat de renormalisatie van de totale lading niet alleen afhangt van de echte totale lading, maar ook van de verdeling hiervan.

Tenslotte stellen we twee modellen op waarin we bifurcatietheorie toepassen op een gelineariseerde beschrijvingen voor heterogeengeladen bollen. In hoofdstuk 4 introduceren we een celmodel dat we afleiden als generalisatie van het celmodel voor mengsels van homogeengeladen bollen. We gebruiken dit model in hoofdstuk 5 als representatie voor vloeistoffasen, aangezien ordening in de posities van deeltjes hier afwezig is. Het tweede model wordt behandeld in hoofdstuk 6 en plaatst de deeltjes op een vast rooster dat de positionele ordening in een vaste stof kenmerkt. In beide gevallen onderzoeken we de mogelijkheid voor een overgang in de oriëntatieverdeling

van isotroop naar opgelijnd. In de vloeistoffase vinden we die niet, terwijl er zich in de vastestoffase twee van zulke overgangen kunnen bevinden – afhankelijk van de systeemparameters. In het ene geval resulteert de overgang in een verdeling die symmetrisch is onder inversie van de oplijningsrichting, in het andere geval niet.

Dankwoord

Hierbij mijn dank aan iedereen die een bijdrage heeft geleverd aan het tot stand komen van dit proefschrift.
Met name René voor zijn begeleiding in het schrijven en onderzoeken; en de weldadige invloed van zijn fysische intuïtie in onze wetenschappelijke discussies.
Niels, Marjolein, Elma en Stephan voor een fijne samenwerking.
Henk en Paul voor hun kritische blik bij het doorlezen van het manuscript.
Verder wil ik Eline bedanken voor haar morele steun in de (onvermijdelijke) moeilijke perioden van de afgelopen vier jaar.
Erik voor zijn interesse in mijn onderzoek (en de natuurwetenschappen in het algemeen), waarin hij mij aanspoorde om ingewikkelde materie in simpele en duidelijke bewoordingen uit te leggen.
Tenslotte ben ik mijn collega's erkentelijk voor de goede werksfeer op het instituut, waardoor ik elke dag met plezier naar de Uithof afreisde. Vooral mijn kamergenoten Henk en Ties speelden hierin een essentiële rol.

Bibliography

[1] S. C. Glotzer and M. J. Solomon. Anisotropy of building blocks and their assembly into complex structures. *Nature Mater.*, 6:557–562, 2007.

[2] Patrick M. Johnson, Carlos M. van Kats, and Alfons van Blaaderen. Synthesis of colloidal silica dumbbells. *Langmuir*, 21:11510–11517, 2005.

[3] Edwin Snoeks, Alfons van Blaaderen, Teun van Dillen, Carlos M. van Kats, Mark L. Brongersma, and Albert Polman. Colloidal ellipsoids with continuously variable shape. *Adv. Mater. (Weinheim, Ger.)*, 12:1511–1514, 2000.

[4] H. R. Sheu, M. S. El-Aasser, and J. W. Vanderhoff. Phase separation in polystyrene latex interpenetrating polymer networks. *J. Polym. Sci. A*, 28:629–651, 1990.

[5] Yadong Yin and A. Paul Alivisatos. Colloidal nanocrystal synthesis and the organic–inorganic interface. *Nature (London)*, 437:664–670, 2005.

[6] Young-Wook Jun, Jung-Wook Seo, Sang Jun Oh, and Jinwoo Cheon. Recent advances in the shape control of inorganic nano-building blocks. *Coord. Chem. Rev.*, 249:1766–1775, 2005.

[7] Catherine J. Murphy, Tapan K. Sau, Anand M. Gole, Christopher J. Orendorff, Jinxin Gao, Linfeng Gou, Simona E. Hunyadi, and Tan Li. Anisotropic metal nanoparticles: Synthesis, assembly, and optical applications. *J. Phys. Chem. B*, 109:13857–13870, 2005.

[8] Carmen I. Zoldesi and Arnout Imhof. Synthesis of monodisperse colloidal spheres, capsules, and microballoons by emulsion templating. *Adv. Mater. (Weinheim, Ger.)*, 17:924–928, 2005.

[9] Young-Sang Cho, Gi-Ra Yi, Jong-Min Lim, Shin-Hyun Kim, Vinothan N. Manoharan, David J. Pine, and Seung-Man Yang. Self-organization of bidisperse colloids in water droplets. *J. Am. Chem. Soc.*, 127:15968–15975, 2005.

[10] Daniela J. Kraft, Wessel S. Vlug, Carlos M. van Kats, Alfons van Blaaderen, Arnout Imhof, and Willem K. Kegel. Self-assembly of colloids with liquid protrusions. *J. Am. Chem. Soc.*, 131:1182–1186, 2009.

[11] L. Hong, A. Cacciuto, E. Luijten, and S. Granick. Clusters of charged janus spheres. *Nano Lett.*, 6:2510–2514, 2006.

[12] A. Walther and A. H. E. Müller. Janus particles. *Soft Matter*, 4:663–668, 2008.

[13] Alicia M. Jackson, Jacob W. Myerson, and Francesco Stellacci. Spontaneous assembly of subnanometre-ordered domains in the ligand shell of monolayer-protected nanoparticles. *Nature Mater.*, 3:330–336, 2004.

[14] Gang Zhang, Dayang Wang, and Helmuth Möhwald. Decoration of microspheres with gold nanodots—giving colloidal spheres valences. *Angew. Chem. Int. Ed.*, 44:7767–7770, 2005.

[15] Gretchen A. DeVries, Markus Brunnbauer, Ying Hu, Alicia M. Jackson, Brenda Long, Brian T. Neltner, Oktay Uzun, Benjamin H. Wunsch, and Francesco Stellacci. Divalent metal nanoparticles. *Science*, 315:358–361, 2007.

[16] Mirjam E. Leunissen, Rémi Dreyfus, Roujie Sha, Tong Wang, Nadrian C. Seeman, David J. Pine, and Paul M. Chaikin. Towards self-replicating materials of DNA-functionalized colloids. *Soft Matter*, 5:2422–2430, 2009.

[17] Seymour S. Cohen. The isolation and crystallization of plant viruses and other protein macro molecules by means of hydrophilic colloids. *J. Biol. Chem.*, 144: 353–362, 1942.

[18] Marie Adams, Zvonimir Dogic, Sarah L. Keller, and Seth Fraden. Entropically driven microphase transitions in mixtures of colloidal rods and spheres. *Nature (London)*, 393:349–352, 1998.

[19] Peter Bolhuis and Daan Frenkel. Tracing the phase boundaries of hard spherocylinders. *J. Chem. Phys.*, 106:666–687, 1997.

[20] Lars Onsager. The effect of shape on the interaction of colloidal particles. *Ann. N.Y. Acad. Sci.*, 51:627–659, 1949.

[21] Seth Fraden, Georg Maret, D. L. D. Caspar, and Robert B. Meyer. Isotropic–nematic phase transition and angular correlations in isotropic suspensions of tobacco mosaic virus. *Phys. Rev. Lett.*, 63:2068–2071, 1989.

[22] Michel P. B. van Bruggen, Felix M. van der Kooij, and Henk N. W. Lekkerkerker. Liquid crystal phase transitions in dispersions of rod-like colloidal particles. *J. Phys.: Condens. Matter*, 8:9451–9456, 1996.

[23] Zvonimir Dogic and Seth Fraden. Development of model colloidal liquid crystals and the kinetics of the isotropic–smectic transition. *Philos. Trans. R. Soc. London, Ser. A*, 359:997–1015, 2001.

[24] Anand Yethiraj. Tunable colloids: control of colloidal phase transitions with tunable interactions. *Soft Matter*, 3:1099–1115, 2007.

[25] Zvonimir Dogic and Seth Fraden. Ordered phases of filamentous viruses. *Curr. Opin. Colloid Interface Sci.*, 11:47–55, 2006.

[26] Wei Chen, Susheng Tan, Tai-Kai Ng, Warren T. Ford, and Penger Tong. Long-ranged attraction between charged polystyrene spheres at aqueous interfaces. *Phys. Rev. Lett.*, 95:218301, 2005.

[27] Wei Chen, Susheng Tan, Yi Zhou, Tai-Kai Ng, Warren T. Ford, and Penger Tong. Attraction between weakly charged silica spheres at a water-air interface induced by surface-charge heterogeneity. *Phys. Rev. E*, 79:041403, 2009.

[28] Liang Hong, Angelo Cacciuto, Erik Luijten, and Steve Granick. Clusters of amphiphilic colloidal spheres. *Langmuir*, 24:621–625, 2008.

[29] M. Gouy. Sur la constitution de la charge électrique á la surface d'un électrolyte. *J. Phys. Radium*, 9:457–468, 1910.

[30] David Leonard Chapman. A contribution to the theory of electrocapillarity. *Phil. Mag.*, 25:475–481, 1913.

[31] W. B. Russel, D. A. Saville, and W. R. Schowalter. *Colloidal dispersions*. Cambridge University Press, Cambridge, 1989. Chapter 4.

[32] Jacob Israelachvili. *Intermolecular & surface forces*. Academic Press, New York, 1991. Second edition. Chapter 12.

[33] Nathan Argaman and Guy Makov. Density Functional Theory—an introduction. e-print arXiv:9806013, 1998.

[34] R. Evans. The nature of the liquid–vapour interface and other topics in the statistical mechanics of non-uniform, classical fluids. *Adv. Phys.*, 28:143–200, 1979.

[35] R. Car and M. Parrinello. Unified approach for molecular dynamics and density-functional theory. *Phys. Rev. Lett.*, 55:2471–2474, 1985.

[36] Peter Debye and Erich Hückel. Zur Theorie der Elektrolyte. I. Gefrierpunktserniedrigung und verwandte Erscheinungen. *Phys. Z.*, 24:185–206, 1923.

[37] Peter Debye and Erich Hückel. On the theory of electrolytes. I. Freezing point depression and related phenomena. In *The collected papers of Peter J. W. Debye*, pages 217–263. Interscience Publishers, New York, 1954.

[38] B. Derjaguin. On the repulsive forces between charged colloid particles and on the theory of slow coagulation and stability of lyophobe sols. *Trans. Faraday Soc.*, 35:203–215, 1940.

[39] E. J. W. Verwey and J. Th. G. Overbeek. *Theory of the stability of lyophobic colloids*. Elsevier, Amsterdam, 1948.

[40] Steven L. Carnie and Derek Y. C. Chan. Interaction energy between identical spherical colloidal particles: The linearized Poisson-Boltzmann theory. *J. Colloid Interface Sci.*, 155:297–312, 1993.

[41] René van Roij and Jean-Pierre Hansen. Van der Waalslike instability in suspensions of mutually repelling charged colloids. *Phys. Rev. Lett.*, 79:3082–3085, 1997.

[42] Bas Zoetekouw and René van Roij. Volume terms for charged colloids: A grand-canonical treatment. *Phys. Rev. E*, 73:021403, 2006.

[43] R. F. Kayser, Jr. and H. J. Raveché. Bifurcation in onsager's model of the isotropic-nematic transition. *Phys. Rev. A*, 17:2067–2072, 1978.

[44] H. Zocher. Über freiwillige Strukturbildung in Solen: Eine neue Art anisotrop flüssiger Medien. *Z. Anorg. Allg. Chem.*, 147:91–110, 1925.

[45] F. C. Bawden, N. W. Pirie, J. D. Bernal, and I. Fankuchen. Liquid crystalline substances from virus-infected plants. *Nature (London)*, 138:1051–1052, 1936.

[46] R. Eppenga and Daan Frenkel. Monte carlo study of the isotropic and nematic phases of infinitely thin hard platelets. *Mol. Phys.*, 52:1303–1334, 1984.

[47] José A. Cuesta and Yuri Martínez-Ratón. Fundamental measure theory for mixtures of parallel hard cubes. I. General formalism. *J. Chem. Phys.*, 107: 6379–6389, 1997.

[48] Yuri Martínez-Ratón and José A. Cuesta. Fundamental measure theory for mixtures of parallel hard cubes. II. Phase behavior of the one-component fluid and of the binary mixture. *J. Chem. Phys.*, 111:317–327, 1999.

[49] Ansgar Esztermann, Hendrik Reich, and Matthias Schmidt. Density functional theory for colloidal mixtures of hard platelets, rods, and spheres. *Phys. Rev. E*, 73:011409, 2006.

[50] Patrick Pfleiderer and Tanja Schilling. Simple monoclinic crystal phase in suspensions of hard ellipsoids. *Phys. Rev. E*, 75:020402(R), 2007.

[51] David Chapot, Lydéric Bocquet, and Emmanuel Trizac. Interaction between charged anisotropic macromolecules: Application to rod-like polyelectrolytes. *J. Chem. Phys.*, 120:3969–3982, 2004.

[52] Rosa Ramirez and Roland Kjellander. Effective multipoles and Yukawa electrostratics in dressed molecule theory. *J. Chem. Phys.*, 125:144110, 2006.

[53] A. M. Somoza and P. Tarazona. Nematic and smectic liquid crystals of hard spherocylinders. *Phys. Rev. A*, 41:965–970, 1990.

[54] J. A. C. Veerman and Daan Frenkel. Phase diagram of a system of hard spherocylinders by computer simulation. *Phys. Rev. A*, 41:3237–3244, 1990.

[55] A. Poniewierski and R. Hołyst. Density-functional theory for systems of hard rods. *Phys. Rev. A*, 41:6871–6880, 1990.

[56] Gert Jan Vroege and Henk N. W. Lekkerkerker. Phase transitions in lyotropic colloidal and polymer liquid crystals. *Rep. Prog. Phys.*, 55:1241–1309, 1992.

[57] Hartmut Graf and Hartmut Löwen. Density functional theory for hard spherocylinders: Phase transitions in the bulk and in the presence of external fields. *J. Phys.: Condens. Mat.*, 11:1435–1452, 1999.

[58] A. Stroobants, H. N. W. Lekkerkerker, and Th. Odijk. Effect of electrostatic interaction on the liquid crystal phase transition in solutions of rodlike polyelectrolytes. *Macromolecules*, 19:2232–2238, 1986.

[59] Carlos Vega and Peter A. Monson. Plastic crystal phases of hard dumbbells and hard spherocylinders. *J. Chem. Phys.*, 107:2696–2697, 1997.

[60] Matthieu Marechal and Marjolein Dijkstra. Stability of orientationally disordered crystal structures of colloidal hard dumbbells. *Phys. Rev. E*, 77:061405, 2008.

[61] I. A. Nyrkova and A. R. Khokhlov. Liquid crystalline ordering in polyelectrolyte solutions. *Biophysics (Engl. Transl.)*, 31:839–845, 1986.

[62] Takahiro Sato and Akio Teramoto. Pertubation theory of isotropic–liquid-crystal phase equilibria in polyelectrolyte solutions. *Physica A*, 176:72–86, 1991.

[63] Shing-Bor Chen and Donald L. Koch. Isotropic–nematic phase transitions in aqueous solutions of weakly charged, rodlike polyelectrolytes. *J. Chem. Phys.*, 104:359–374, 1996.

[64] Irina A. Nyrkova, Nadezhda P. Shusharina, and Alexei R. Khokhlov. Liquid-crystalline ordering in solutions of polyelectrolytes. *Macromol. Theory Simul.*, 6:965–1006, 1997.

[65] Igor I. Potemkin, Roman E. Limberger, Alexander N. Kudlay, and Alexei R. Khokhlov. Rod-like polyelectrolyte solutions: Effect of the many-body Coulomb attraction of similarly charged molecules favoring weak nematic ordering at very small polymer concentration. *Phys. Rev. E*, 66:011802, 2002.

[66] Bertram Weyerich, Bruno D'Aguanno, Enrique Canessa, and Rudolf Klein. Structure and dynamics of suspensions of charged rod-like particle. *Faraday Discuss. Chem. Soc.*, 90:245–259, 1990.

[67] Hartmut Graf and Hartmut Löwen. Phase diagram of tobacco mosaic virus solutions. *Phys. Rev. E*, 59:1932–1942, 1999.

[68] Ahmet F. Demirors, Arnout Imhof, and Alfons van Blaaderen. Unpublished work on colloidal silica and titania dumbbells.

[69] Michael P. Allen, Glenn T. Evans, Daan Frenkel, and Bela Mulder. Hard convex body fluids. *Adv. Chem. Phys.*, 86:1–166, 1993.

[70] Bernard P. Binks. Particles as surfactants: Similarities and differences. *Curr. Opinion Coll. Interface Sci.*, 7:21–41, 2002.

[71] Pawel Pieranski. Two-dimensional interfacial colloidal crystals. *Phys. Rev. Lett.*, 45:569–572, 1980.

[72] Derek Frydel, Siegfried Dietrich, and Martin Oettel. Charge renormalization for effective interactions of colloids at water interfaces. *Phys. Rev. Lett.*, 99: 118302, 2007.

[73] Spencer Umfreville Pickering. Emulsions. *J. Chem. Soc.*, 91:2001–2021, 1907.

[74] K. Stratford, R. Adhikari, I. Pagonabarraga, J.-C. Desplat, and M. E. Cates. Colloidal jamming at interfaces: A route to fluid-bicontinuous gels. *Science*, 309:2198–2201, 2005.

[75] Michael E. Cates and Paul S. Clegg. Bijels: A new class of soft materials. *Soft Matter*, 4:2132–2138, 2008.

[76] J. H. Liao, K. J. Chen, L. N. Xu, C. W. Ge, J. Wang, L. Huang, and N. Gu. Self-assembly of length-tunable gold nanoparticle chains in organic solvents. *Appl. Phys. A*, 76:541–543, 2003.

[77] Kyung-Sang Cho, Dmitri V. Talapin, Wolfgang Gaschler, and Christopher B. Murray. Designing PbSe nanowires and nanorings through oriented atachment of nanoparticles. *J. Am. Chem. Soc.*, 127:7140–7147, 2005.

[78] S. Alexander, P. M. Chaikin, P. Grant, G. J. Morales, P. Pincus, and D. Hone. Charge renormalization, osmotic pressure, and bulk modulus of colloidal crystals: Theory. *J. Chem. Phys.*, 80:5776–5781, 1984.

[79] A. Diehl, M. C. Barbosa, and Y. Levin. Charge renormalization and phase separation in colloidal suspensions. *Europhys. Lett.*, 53:86–92, 2001.

[80] E. Trizac, L. Bocquet, M. Aubouy, and H.-H. von Grünberg. Alexanders prescription for colloidal charge renormalization. *Langmuir*, 19:4027–4033, 2003.

[81] Emmanuel Trizac, Lydéric Bocquet, and Miguel Aubouy. Simple approach for charge renormalization in highly charged macroions. *Phys. Rev. Lett.*, 89: 248301, 2002.

[82] Bas Zoetekouw and René van Roij. Nonlinear screening and gas–liquid separation in suspensions of charged colloids. *Phys. Rev. Lett.*, 97:258302, 2006.

[83] S. J. Miklavic, D. Y. C. Chan, L. R. White, and T. W. Healy. Double layer forces between heterogeneous charged surfaces. *J. Phys. Chem.*, 98:9022–9032, 1994.

[84] Armik V. M. Khachatourian and Anders O. Wistrom. Electrostatic interaction force between planar surfaces due to 3-D distribution of sources of potential (charge). *J. Phys. Chem. B*, 102:2483–2493, 1998.

[85] Norman Hoffmann, Christos N. Likos, and Jean-Pierre Hansen. Linear screening of the electrostatic potential around spherical particles with non-spherical charge patterns. *Mol. Phys.*, 102:857–867, 2004.

[86] Z. J. Lian and H. R. Ma. Effective interaction of nonuniformly charged colloid spheres in a bulk electrolyte. *J. Chem. Phys.*, 127:104507, 2007.

[87] A. Domínguez, D. Frydel, and M. Oettel. Multipole expansion of the electrostatic interaction between charged colloids at interfaces. *Phys. Rev. E*, 77: 020401(R), 2008.

[88] R. J. F. Leote de Carvalho, E. Trizac, and J.-P. Hansen. Nonlinear screening and gas–liquid separation in suspensions of charged colloids. *Phys. Rev. E*, 61: 1634–1647, 2000.

[89] E. Wigner and F. Seitz. On the constitution of metallic sodium. *Phys. Rev.*, 43: 804–810, 1933.

[90] Rosa Ramirez and Roland Kjellander. Dressed molecule theory for liquids and solutions: An exact charge renormalization formalism for molecules with arbitrary charge distributions. *J. Chem. Phys.*, 119:11380–11395, 2003.

[91] R. A. Marcus. Calculation of thermodynamic properties of polyelectrolytes. *J. Chem. Phys.*, 23:1057–1068, 1955.

[92] T. Ohtsuki, S. Mitaku, and K. Okano. Studies of ordered monodisperse latexes. ii. theory of mechanical properties. *Jpn. J. Appl. Phys.*, 17:627–635, 1978.

[93] P. M. Biesheuvel, S. Lindhoud, R. de Vries, and M. A. Cohen Stuart. Phase behavior of mixtures of oppositely charged nanoparticles: Heterogeneous poisson-boltzmann cell model applied to lysozyme and succinylated lysozyme. *Langmuir*, 22:1291–1300, 2006.

[94] H. H. von Grünberg, R. van Roij, and G. Klein. Gas-liquid phase coexistence in colloidal suspensions? *Europhys. Lett.*, 55:580–586, 2001.

[95] A. Torres, G. Téllez, and R. van Roij. The polydisperse cell model: Nonlinear screening and charge renormalization in colloidal mixtures. *J. Chem. Phys.*, 128:154906, 2008.

[96] H. H. von Grünberg and L. Belloni. Eccentric poisson-boltzmann cell model. *Phys. Rev. E*, 62:2493–2500, 2000.

[97] J.-P. Hansen and E. Trizac. Electric double layers around finite-size clay particles. *Physica A*, 235:257–268, 1997.

[98] L. Bocquet, E. Trizac, and M. Aubouy. Effective charge saturation in colloidal suspensions. *J. Chem. Phys.*, 117:8138–8152, 2002.

[99] B. M. Mulder. Isotropic-symmetry-breaking bifurcations in a class of liquid-crystal models. *Phys. Rev. A*, 39:360–370, 1989.

[100] Zhiyong Tang, Nicholas A. Kotov, and Michael Giersig. Spontaneous organization of single CdTe nanoparticles into luminescent nanowires. *Science*, 297: 237–240, 2002.

[101] S. C. Glotzer, M. J. Solomon, and N. A. Kotov. Self-assembly: From nanoscale to microscale colloids. *AIChE J.*, 50:2978–2985, 2004.

[102] Amit Goyal, Carol K. Hall, and Orlin D. Velev. Phase diagram for stimulus-responsive materials containing dipolar colloidal particles. *Phys. Rev. E*, 77: 031401, 2008.

[103] J. B. Caballero, A. M. Puertas, A. Fernández-Barbero, and F. J. de las Nieves. Oppositely charged colloidal binary mixtures: A colloidal analog of the restricted primitive model. *J. Chem. Phys.*, 121:2428–2435, 2004.

[104] M. E. Leunissen, C. G. Christova, A.-P. Hynninen, C. P. Royall, A. I. Campbell, A. Imhof, M. Dijkstra, R. van Roij, and A. van Blaaderen. Ionic colloidal crystals of oppositely charged particles. *Nature (London)*, 437:235–240, 2005.

[105] E. Trizac and Y. Levin. Renormalized jellium model for charge-stabilized colloidal suspensions. *Phys. Rev. E*, 69:031403, 2004.

[106] S. Pianegonda, E. Trizac, and Y. Levin. The renormalized jellium model for spherical and cylindrical colloids. *J. Chem. Phys.*, 126:014702, 2007.

[107] R. Castañeda-Priego, L. F. Rojas-Ochoa, V. Lobaskin, and J. C. Mixteco-Sánchez. Macroion correlation effects in electrostatic screening and thermodynamics of highly charged colloids. *Phys. Rev. E*, 74:051408, 2006.

[108] Thiago E. Colla, Yan Levin, and Emmanuel Trizac. A self-consistent renormalized jellium approach for calculating structural and thermodynamic properties of charge stabilized colloidal suspensions. *J. Chem. Phys.*, 131:074115, 2009.

[109] Hartmut Graf, Hartmut Löwen, and Matthias Schmidt. Cell theory for the phase diagram of hard spherocylinders. *Prog. Colloid Polym. Sci.*, 104:177–179, 1997.

[110] I. S. Gradshteyn and I. M. Ryzhik. *Table of integrals, series, and products*. Academic Press, New York, 1980. Eq. 8.532 1.

[111] Milton Abramowitz and Irene A. Stegun, editors. *Handbook of mathematical functions*. Dover Publications, New York, 1965. Eq. 10.2.35.

[112] M. Danos and L. C. Maximon. Multipole matrix elements of the translation operator. *J. Math. Phys.*, 6:766–778, 1965.

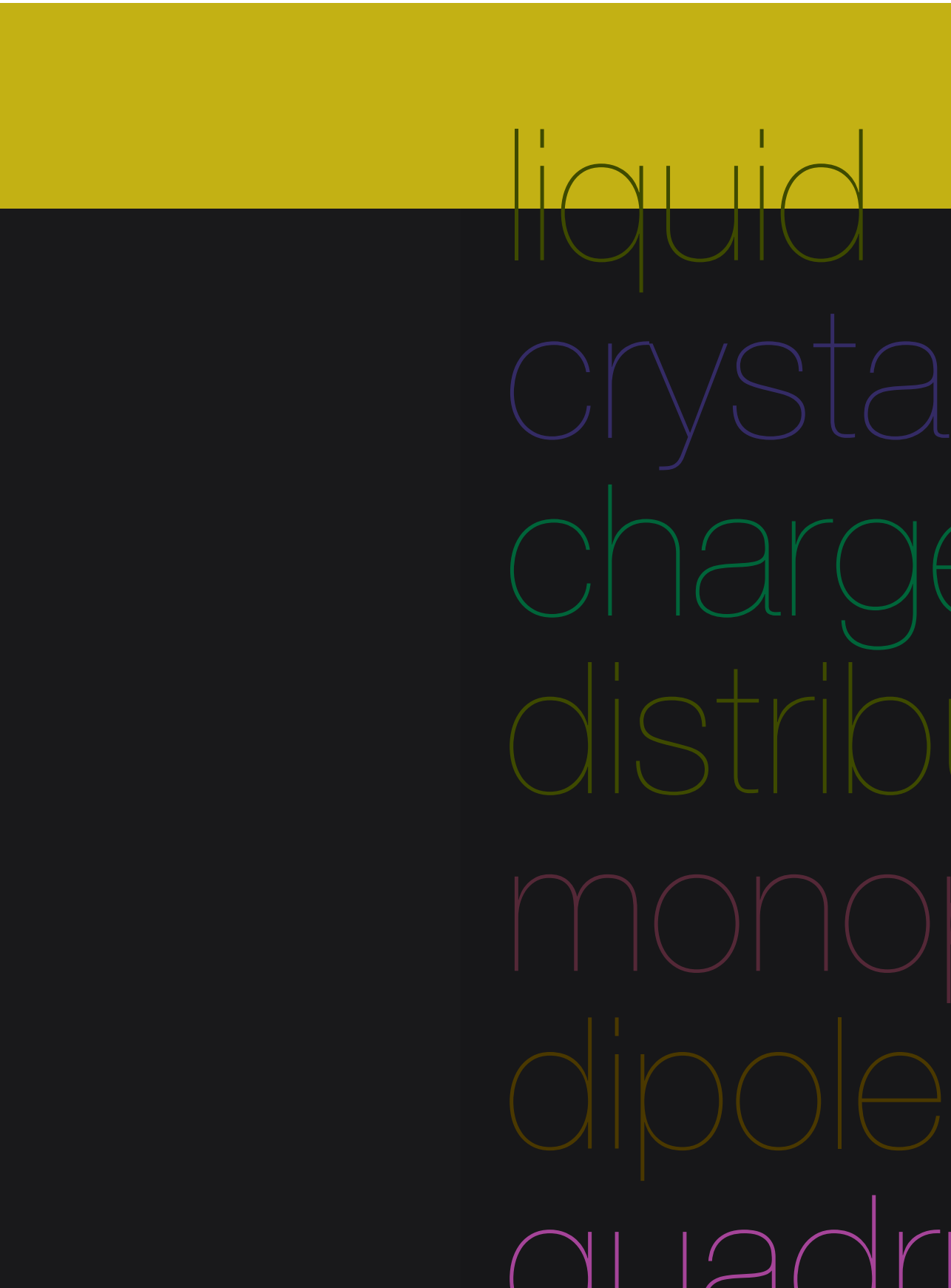
liquid
crysta
charge
distribu
monop
dipole
quadr